

AFIT/GAE/ENY/97D-02.

**Fatigue Behavior of a Quasi-Isotropic  
Graphite/Epoxy Laminate Embedded with a  
Piezoelectric Sensor**

**Thesis**

**Jon M. Coleman B.S.M.E., M.B.A.  
Captain, USAF**

**AFIT/GAE/ENY/97D-02.**

19980210 039

AFIT/GAE/ENY/97D-02.

**“The views expressed in this thesis are those of the author and do not reflect the official policy or position of the Department of Defense or the U.S. Government.”**

**AFIT/GAE/ENY/97D-02.**

Approved for public release; distribution unlimited

AFIT/GAE/ENY/97D-02.

***Fatigue Behavior of a Quasi-Isotropic Graphite/Epoxy  
Laminate Embedded with a Piezoelectric Sensor***

**Thesis**

Presented to the Faculty of the Graduate School of Engineering of the Air Force Institute of  
Technology Air University In Partial Fulfillment for the Degree of

**Master of Science**

Specialization in: Aeronautical Engineering

**BY**

**Jon M. Coleman B.S.M.E., M.B.A.**

**Captain, USAF**

Air Force Institute of Technology

Wright-Patterson AFB, Ohio

1 December, 1997

Sponsored by AFOSR and Wright-Labs, WPAFB, OH

Approved for public release; distribution unlimited

***Fatigue Behavior of a Quasi-Isotropic Graphite/Epoxy  
Laminate Embedded with a Piezoelectric Sensor***

**Jon M. Coleman B.S.M.E., M.B.A.**

**Captain, USAF**

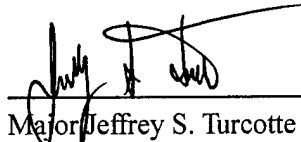
Approved:



Dr. Shankar Mall  
Committee Chairman

1 Dec 97

Date



Major Jeffrey S. Turcotte  
Committee member

1 DEC 97

Date



Captain Gregory S. Agnes  
Committee member

1 Dec 97

Date

## *Acknowledgments*

I would like to give my thanks to God and to the many people who helped me researching and writing this thesis. My wife and family have given me tremendous support throughout our assignment at AFIT, for which I am extremely grateful. My thesis advisor, Dr. Mall, has been patient, provided invaluable expertise, and directed the extent and schedule of the thesis. Mr. Mark Derriso of the Structural Dynamics Lab developed much of the software used in the testing and was always ready to help me understand how to use all the equipment. I would like to give special thanks to my sponsors, Capt Brian Sanders of AFOSR and Dr. Steve Donaldson of Wright Laboratory, for both their financial support and latitude provided to me in this thesis. From UDRI, Dr. Kim, Mr. Ron Cornwell, Mr. Brian Rice, and Mr. Ron Esterline, provided me excellent support in manufacturing the specimens and general technical expertise. Other people who helped me in understanding experimental methods and software include Mr. Sean Coghlan, Dr. Jeff Calcaterra, Capt Lance Chenault and Capt Alvin Ruiz. In addition, I would like to thank Maj Turcotte and Capt Agnes, who filtered through the many pages of text and figures.

# *Table Of Contents*

Acknowledgments .....	iii
Table Of Contents .....	iv
List Of Figures .....	viii
List Of Tables .....	xii
List of Symbols .....	xiii
Abstract .....	xvi
1. INTRODUCTION .....	1
1.1 Background .....	1
1.2 Problem Statement .....	4
1.3 Summary of Chapters and Appendices .....	5
2. PREVIOUS RESEARCH AND THEORY .....	6
2.1 Research .....	6
2.1.1 Fatigue Strength of Composite Structures .....	6
2.1.2 Structural Integrity Effects of Embedded Devices .....	12
2.1.3 Electro-Mechanical Behavior of PZTs .....	13
2.1.4 Low Strain Fatigue Response .....	15
2.2 Theory .....	17
2.2.1 Piezoelectric Material Theory .....	17

2.2.2	Composite Material Theory .....	20
2.2.2.1	Background .....	20
2.2.2.2	Micromechanic Theory .....	23
2.2.2.3	Macromechanical Theory .....	24
3.	TESTING PREPARATION AND PROCEDURES .....	26
3.1	Test Set up .....	26
3.1.1	Test Specimen Design .....	26
3.1.1.1	Laminate Selection .....	26
3.1.1.2	Specimen Dimensions .....	28
3.1.1.3	Manufacturing Method .....	30
3.1.2	Strain Measurement .....	34
3.1.3	PZT Sensor's Health and Its Output Measurement .....	34
3.1.4	Damage Detection .....	35
3.1.5	Material Test System .....	35
3.2	Experimental Procedure .....	36
3.2.1	Monotonic Test Procedure .....	38
3.2.2	Fatigue Test Procedure .....	39
4.	RESULTS & DISCUSSION .....	42
4.1	Monotonic Test Results .....	42
4.1.1	Stress-Strain Response of ATST2 and FT8 Specimens .....	43

4.1.2	Damage Mechanism .....	47
4.1.2.1	Un-Interrupted Loading .....	47
4.1.2.2	Interrupted Loading .....	47
4.1.2.3	Initial Transverse Cracks in 90° Plies .....	50
4.1.2.4	[±45] Cracking, Longitudinal Cracking, and Delamination .....	52
4.1.3	Degradation of PZT Output .....	56
4.2	Fatigue Test Results .....	60
4.2.1	S-N Curve .....	62
4.2.2	Damage Mechanism .....	65
4.2.2.1	Failure Surfaces .....	65
4.2.2.2	Change in Young's Modulus .....	71
4.2.2.3	Depth of Delamination .....	81
4.2.3	Degradation of PZT Output .....	90
4.2.3.1	Voltage Degradation from Fatigue Loading .....	91
4.2.3.2	Low-Strain versus Cycles Curve .....	96
5.	CONCLUSIONS AND RECOMMENDATIONS .....	105
	Appendix A. Laminate Properties and Equations .....	108
	Appendix B. Ply Discount Method .....	110
B.1	First Ply Failure (Ultimate Strain) .....	110
B.2	Change in Modulus and Ultimate Strength .....	110



B.2.1	Modulus after 90° Plies Have Failed . . . . .	110
B.2.2	Estimated Ultimate Strength of Laminate at This Point . . . . .	111
B.2.3	Modulus after -45° Plies Have Failed . . . . .	111
B.2.4	Estimated Ultimate Strength of Laminate at This Point . . . . .	111
Appendix C. Capacitance Calculations . . . . .		113
Appendix D. Discussion of $[0 0 \pm 45 0 0 90]_S$ Testing . . . . .		116
D.1	Test Preparation . . . . .	116
D.2	Specimen AAT1, 40% Load (552 MPa) Damage Progression . . . . .	116
D.2.1	Lessons Learned . . . . .	119
D.3	Specimen AAT2, 443 MPa, PZT Response to Mechanical Cycling . . . . .	120
Bibliography . . . . .		129
Vita . . . . .		130

## *List Of Figures*

Figure 1	Damage Sequence During Fatigue Loading [21] .....	9
Figure 2	Interlaminar Stresses Near the Crack Tip [21] .....	9
Figure 3	Normalized Stiffness vs Cycles [21] .....	10
Figure 4	Normalized Stiffness vs Normalized Cycles [21] .....	10
Figure 5	Switching of Polarity Due to Applied Stress and Electric Field [13] .....	16
Figure 6	Polarization vs Electric Field Hysteresis Loop [3] .....	19
Figure 7	Active Control eXperts (ACX) QP15N PZT .....	27
Figure 8	Diagram of Specimen with Embedded PZT .....	29
Figure 9	Diagram of Cut-out Plies and Inserted PZT in $[0 \pm 45 90]_S$ Laminate .....	31
Figure 10	Kapton Tape Applied at the Ends to Protect Lead Wires .....	33
Figure 11	Ultrasound Inspection of Panel Embedded with Five PZTs .....	33
Figure 12	QRMS-II Optics, 810 MTS Test System, 486 Pentium Computers and Monitors .....	37
Figure 13	Stress-Strain Curve for Specimens FT8 and ATST2 .....	46
Figure 14	Extensometer vs Strain Gage Data - Specimen FT8 .....	48
Figure 15	Specimen FT1 at Static Failure .....	48
Figure 16	FT1 Static "Flat" Failure Across the Width .....	49
Figure 17	FT1 Edge Delamination at Static Failure .....	49
Figure 18	Transverse Cracking of $90^\circ$ Plies - Specimen ATST1 .....	51

Figure 19 Crack in -45° Ply - Specimen ATST1 .....	54
Figure 20 Longitudinal Cracking Between 90° and -45° Plies (FT7) .....	55
Figure 21 Degradation of PZT Output after Intermediate Static Loads (ATST1) .....	58
Figure 22 Capacitance vs Applied Stress - Specimen ATST1 .....	59
Figure 23 Mathematical vs Experimental Changes in Capacitance .....	61
Figure 24 S-N Curve .....	63
Figure 25 S-N Curve on Larger Scale .....	64
Figure 26 Edge Delamination - Specimen FT6 .....	66
Figure 27 Delamination at Cycle 1k - Specimen AT2 .....	67
Figure 28 Delamination at Cycle 10k - Specimen AT2 .....	67
Figure 29 Delamination at Cycle 50k - Specimen AT2 .....	68
Figure 30 Failed Specimen FT4 .....	68
Figure 31 “Jagged” Failure Area - Specimen FT4 .....	69
Figure 32 Edge Delamination at “Jagged” Failure Area - Specimen FT4 .....	69
Figure 33 Failed Fibers Away from Ultimate Failure Region - Specimen FT4 .....	70
Figure 34 Failed Specimen FT5 .....	72
Figure 35 Failed Specimen AT2 .....	73
Figure 36 Split PZT of Specimen AT2 .....	74
Figure 37 Lead Wires of Specimen AT2 .....	74
Figure 38 Normalized Modulus vs Cycles - FT Specimens .....	76

Figure 39 Normalized Modulus vs Normalized Cycles - FT Specimens . . . . .	77
Figure 40 AT Specimens Normalized Modulus vs Cycles . . . . .	79
Figure 41 AT Specimens Normalized Modulus vs Normalized Cycles . . . . .	80
Figure 42 Normalized Modulus vs Normalized Cycles on Larger Scale . . . . .	82
Figure 43 Comparison of External Surface and Ultrasound Inspection Methods - Specimen FT6 . . . . .	83
Figure 44 Depth of Delamination vs Cycles - FT Specimens . . . . .	84
Figure 45 Depth of Delamination vs Cycles - AT Specimens . . . . .	86
Figure 46 Depth of Delamination vs Cycles for All Specimens . . . . .	87
Figure 47 Edge View of AT2 at 500k Cycles . . . . .	88
Figure 48 Overall Extent of Delamination of FT3 and AT1 at 2 Million Cycles . . . . .	88
Figure 49 Overall Extent of Delamination of FT3 and AT1 at 5 Million Cycles . . . . .	89
Figure 50 Output Voltage vs Strain - Specimen AT1, Cycle 1, (380 MPa) . . . . .	92
Figure 51 Output Voltage vs Strain - Specimen AT1, Cycle 10,000. (380 MPa) . . . . .	93
Figure 52 Output Voltage vs Strain - Specimen AT1, Cycle 1 (60 MPa) . . . . .	94
Figure 53 Output Voltage vs Strain - Specimen AT1, Cycle 500 (76 MPa) . . . . .	95
Figure 54 Schematic Edge View of Specimen AT5 with the Embedded PZT at the Edge . . . . .	98
Figure 55 Voltage vs Strain - Specimen AT5 , Comparison of Output at 1000 $\mu\epsilon$ . . . . .	99
Figure 56 Epoxy Rich Region Due to Cut-out Method - Specimen AT5 . . . . .	100
Figure 57 Bonding Interface Between PZT and Plies - Specimen AT5 . . . . .	100
Figure 58 Voltage Output vs Strain Calibration During Cycling - Specimen AT5 . . . . .	101

Figure 59 Voltage Degradation vs Cycles .....	102
Figure 60 Strain vs Cycles to Sensor Failure, Based on 40 % Reduction of Voltage Output .....	103
Figure 61 Stress-Strain Curve for AAT2 .....	121
Figure 62 Specimen AAT2 Capacitance & Cracks vs Cycles .....	122
Figure 63 Specimen AAT2 Voltage Output vs Strain .....	123
Figure 64 Specimen AAT2 Degradation of Voltage Output at Various Applied Stress Levels .....	125
Figure 65 Frequency Effects on Voltage Output at 100 MPa .....	126
Figure 66 Frequency Effects on Voltage Output at 200 MPa .....	127
Figure 67 Frequency Effects on Voltage Output at 450 MPa .....	128

## *List Of Tables*

Table 1	Summary of Tested Specimens .....	41
Table 2	Monotonically Loaded Specimens .....	44
Table 3	Theoretical vs Experimental Young's Modulus (FT8) .....	45
Table 4	Stress Levels at Which Initial Damage Occured .....	50
Table 5	Summary of Fatigue Tested Specimens .....	63
Table 6	Material Properties of AS4-3501-6 .....	109
Table 7	Quasi-Isotropic Laminate Equations .....	109
Table 8	Mathematical Change in Capacitance .....	115

## *List of Symbols*

### English Symbols

Symbol	Definition
$[A]$	extensional stiffness
$[a]$	extensional compliance
AT	specimen with embedded sensor
ATST	quasi-static specimen with embedded sensor
$[C]$	stiffness
$D$	electric displacement
$E_x$	Young's modulus
$E$	Electric Field
$F$	capacitance (farads)
FT	specimen without embedded sensor
$G$	shear modulus
HP	25.4 millimeter width specimen without sensor
$K_3^T$	dielectric constant
$N$	cycles
$[N]$	force vector
$P$	polarity
$Q$	Electric Potential
$[Q]$	Stiffness

## Greek Symbols

Symbol	Definition
$\varepsilon$	strain
$\varepsilon_0$	permittivity of free space
$\mu$	micro
$\nu$	Poisson's Ratio
$\sigma$	stress

## Subscripts

Symbol	Definition
$f$	fiber
$m$	matrix
$S$	symmetric
$3$	normal to xy-plane

## Superscript

Symbol	Definition
$^{\circ}$	degree

## Abbreviations/Acronyms

Abbreviation	Definition
ACX	Active Control eXperts
AFIT	Air Force Institute of Technology
AFOSR	Air Force Office of Scientific Research



DARPA	Defense Advanced Research Projects Agency
FEM	finite element model
FPF	first ply failure
<i>Hz</i>	hertz
kip	1000 pounds-force
<i>MPa</i>	megapascal
O	oxygen
Pb	lead
PZT	lead zirconate-titanate
QRMS-II	Questar Remote Measurement System
SMS	Smart Materials Structures Program
SPICES	Synthesis and Processing of Intelligent Cost Effective Structures
Ti	titanium
UDRI	University of Dayton Research Institute

## *Abstract*

Described in a simple manner, "smart" structures are materials which can respond to environmental inputs in an intelligent manner. The concept of smart materials covers a broad range of applications and technology. One example is an internal structural vibration damping system, which would use an embedded piezoelectric actuator to detect and dampen vibrations preventing catastrophic failure. This study primarily investigated the mechanical effects of embedding piezoelectric lead zirconate-titanate (PZT) sensors on the tensile strength and fatigue behavior of a quasi-isotropic, carbon-epoxy laminate. A secondary focus was the investigation of the sensor degradation under tensile fatigue loading. An eight ply,  $[0|\pm 45|90]_S$  laminate was fabricated from Hercules AS4/3501-6 pre-preg tape to simulate a laminate similar to those found in aircraft. The embedded PZT, Active Control eXperts (ACX) QP15N, was inserted into a cutout area in the two middle  $90^\circ$  plies. In actual aircraft laminates, a greater percentage of  $0^\circ$  and  $45^\circ$  plies are normally used, therefore this laminate should be considered a worst case scenario for embedding sensors in the  $90^\circ$  plies.

Two types of specimens were used in this study. "AT" specimens were  $304.8\text{ mm} \times 50.8\text{ mm} \times 1.1\text{ mm}$  in size, with an approximate  $50.8\text{ mm} \times 24.5\text{ mm} \times 0.254\text{ mm}$  actuator embedded in the middle. "FT" specimens had the same dimensions without the embedded sensor. Specimens were first tested under monotonic loading to obtain the ultimate tensile strength and to document the progression of damage. Few of these tests were interrupted at different stress levels to measure the cyclic voltage output and capacitance of the PZT. Several other specimens were then fatigue tested under tension-tension loading,  $R = 0.1$ ,  $10\text{ Hz}$ , constant amplitude. Cycles to failure at pre-determined stress levels were then plotted on S-N curves. The damage

progression, PZT voltage output, and capacitance were measured at pre-determined intervals to monitor the health of the structure. In the last part of this study, AT specimens were cycled at low-strain values, below the expected laminate damage, to investigate the fatigue characteristics of the embedded sensor.

Results from this study indicate that it is possible to embed PZTs inside carbon-epoxy laminates without significantly affecting the monotonic tensile and fatigue response of the composite. Results from the monotonic tests showed that the average ultimate stress and modulus of specimens with or without PZTs were within 4% of each other, which was not very significant considering the relatively large size of the embedded PZT. The fatigue life of AT and FT specimens were very comparable as well, where AT specimens actually had a slightly higher fatigue resistance. Overall, the sequence of damage in all specimens in this study agreed with previous investigations on the damage mechanisms for  $[0 | \pm 45 | 90]_S$  quasi-isotropic laminates. First, the  $90^\circ$  plies transversely cracked which slightly decreased in modulus. Resulting stress concentrations near the cracks resulted in further cracking near this area as the load was increased even more. Longitudinal cracking and delamination then occurred as the edge effects caused the plies to pull apart at the edge. The overall range in modulus reduction for FT and AT specimens were usually within 5-15 % of each other during fatigue loading. The rate of delamination growth of AT and FT specimens during most of the fatigue life was very comparable, with no significant variations, which was contrary to previous reports using glass inserts [9, 18]. In addition to the laminate strength and fatigue results, this study showed that PZTs can maintain a steady output indefinitely when mechanically cycled within the operational strain limits. At low-strain levels (200-1000  $\mu\epsilon$ ), the voltage output remained constant for millions of cycles.

# ***Fatigue Behavior of a Quasi-Isotropic Graphite/Epoxy Laminate Embedded with a Piezoelectric Sensor***

## **1. Introduction**

### **1.1 Background**

To help understand smart materials, a brief background of composite materials is necessary. Daniel and Ishai state, "A structural composite is a material system consisting of two or more phases on a macroscopic scale, whose mechanical performance and properties are designed to be superior to those of the constituent materials acting independently [6]". Composite materials have existed for thousands of years. One example is by the ancient Egyptians, who used straw-reinforced clay bricks in construction. Today, composite materials can be found almost anywhere. Plywood, fiberglass, bricks, and concrete are used in many homes. In the military, composite materials have become a critical technology for advanced aircraft. For example, the B-2 stealth bomber is made almost entirely of composite materials, while future hypersonic programs' success depends on the development of advanced composites [5].

In the future, smart materials may replace composite materials in many applications. Smart material technology attempts to take the complementing properties of composite materials a few steps further. Culshaw states, "The concept is all about materials and structures that can react to the world within which they operate and thereby enhance their functionality or survivability [5]". Ahmad defines smart materials as, "A system or a material which has built-in or intrinsic sensor/s, actuator/s, and control mechanism/s whereby it is capable of sensing a stimulus, responding to it in a predetermined manner and extent, in a short appropriate time and reverting to its original state as soon as the stimulus is removed [4]". While the need for a material to

respond in a "smart" manner to an operational environment may be obvious, a few key technologies clarify the focus of the smart material research.

Brei summarizes the key smart material technologies as health and load monitoring, smart skins, shape control, flow control, vibration control, acoustic control, and self-repairability. In health and load monitoring, sensors would receive raw data, and local processors would determine the severity of the damage. The resulting response would give an emergency notification to the pilot or relay maintenance information to logistic personnel. For example, the analysts from the Smart Material Structures Program (SMS), funded by DARPA and the U.S. Air Force, estimated savings of \$35 million per year in maintenance for the F/A-18 by using a triangulation method of acoustic sensors to locate damage. The next technology, smart skins, would embed antennas and sensors to enhance stealth functions of aircraft such as the F-22. Cost savings of \$250K per airframe on the F-22 have been projected along with weight savings of 70 lbs per airframe. Shape control technology would use a combination of sensors, actuators, or shape memory alloys to reduce drag or increase lift. Flow control technology would similarly modify the surface of the material by actuators for improved performance. In vibration control technology, the sensors would detect and actively dampen or cancel vibrations. Piezoelectric actuators have shown to be effective in vibration suppression in the Synthesis and Processing of Intelligent Cost Effective Structures (SPICES) program for motor mounts in submarines. Aircraft applications include vibration suppression of the tails of the F/A-15 and F/A-18. Benefits of decreased vibration include elimination of dynamic instabilities such as tail buffet or wing flutter and the reduction of fatigue damage of the materials. Acoustic control technology studies the ability of a structure to detect and modify acoustic waves. The last technology, self-repairability, studies the structure's ability to detect and repair the damage. In each of these technologies you have

either a dual purpose composite, or a material with the ability to detect and react intelligently to external stimulus [4, 10].

Among the smart material technologies, vibration control via attached piezoelectric actuators is the most researched. A number of programs have been successful in demonstrating this capability. Piezoelectricity has been researched since its discovery over 100 years ago by Jacques and Pierre Curie [4], who found that certain materials became polarized after being mechanically strained. As piezoelectric materials are strained, the output voltage increases almost linearly with increasing strain. The converse is also true; the strain of the piezoelectric material increases linearly with applied voltage. Of course, limits exist for maximum and minimum polarization and strain. Among the better performing actuators are the piezoceramics, such as lead zirconate-titanate (PZT), where manufacturers have packaged the material to protect the structure from premature damage. This report will interchangeably use the acronym PZT, actuator, or sensor when discussing the embedded piezoelectric sensors.

Even though the future for smart structure technology seems promising, operational applications to military aircraft and spacecraft can not be accomplished until its integrity issues are fully understood. As electronics and embedded sensors are integrated into complex aerospace systems, questions arise on the mechanical behavior and integrity of the system. Mechanical response of smart materials when subjected to static loads, cyclic loading, extreme temperatures, radiation, corrosion, humidity, impact, and other environmental factors need to be quantified.

One of the most important, but least researched integrity issues, is the mechanical effect of embedding actuators in a structure. Most smart structure research has focused on electrical component performance and failure, rather than structural integrity [13, 14]. There has been some structural fatigue research on embedded fiber optics and embedded glass inserts, but very

limited research with actual PZTs [8–10, 18]. Further research in this area is needed to advance the application of smart structures to operational vehicles.

## 1.2 Problem Statement

The purpose of this study is to investigate the mechanical fatigue effects of smart structures embedded with PZTs. To investigate mechanical integrity, specimens representative of vibration control application were mechanically fatigued under tension-tension at high and low stress levels. Specimens with and without embedded sensors were compared using several measures, such as first-ply failure, transverse crack density, delamination, modulus, ultimate strain, ultimate strength, and fatigue life. The PZT voltage output was also monitored at high and low stress levels to determine the failure limits and damage mechanism. After these mechanical effects testing, the specimens with embedded sensors were cycled at low-strain ( $200 - 2000 \mu\epsilon$ ), in order to determine the fatigue response of the PZTs near the nominal load range. After all static and fatigue testing was accomplished, the damage sequence and degradation of the structural properties due to embedding PZTs was investigated.

The specimen in this study consisted of a carbon-epoxy (AS4/3501-6), which is found in various military systems. PZTs were embedded by cutting out an area in the center plies and placing the PZT in the area before final curing. Initially, the laminate  $[0|0|\pm 45|0|0|90]_S$  was chosen to protect the actuator and to obtain a typical laminate used in operational structures. This laminate was later abandoned and replaced with the widely studied quasi-isotropic laminate  $[0|\pm 45|90]_S$ . This laminate was chosen to more effectively indicate any degradation due to the insert and to represent a reasonable configuration. Since this laminate has a relatively low percentage of  $0^\circ$  plies, strength reduction from embedding PZTs in the  $90^\circ$  plies should be

considered a worse-case scenario. In the earlier laminate  $[0|0|\pm 45|0|0|90]_S$ , the degradation in structural properties would have been less evident.

### 1.3 Summary of Chapters and Appendices

The remaining chapters of this thesis detail the steps taken to investigate the integrity of laminates embedded with PZTs. Chapter 2 discusses previous research and theory, which includes the fatigue response of composite materials, integrity issues of embedded devices, and mechanical validation of smart structures. Chapter 3 discusses test preparation and procedures, which details the decisions made and equipment used to design, manufacture, and monitor the damage of the specimens. The test results are found in Chapter 4, and the conclusions and recommendations are found in Chapter 5.

The five appendices give additional details that may be of interest to future readers of this report. Appendix A lists in tabular format the laminate properties and equations used to theoretically calculate the modulus and strength of the laminates. Appendix B details the calculations and assumptions made for ply-discount method, which was used to approximate the theoretical decrease in Young's modulus during monotonic and fatigue loading. Appendix C discusses possible reasons why the capacitance value started to rise in some specimens. Potential changes in thickness and PZT dielectric properties are calculated to compare with the initial rise in capacitance. Appendix D briefly discusses the damage progression, lessons learned, and PZT response of the laminate  $[0|0|\pm 45|0|0|90]_S$ .



## **2. Previous Research and Theory**

### **2.1 Research**

This section focuses on previous research dealing with the progression of mechanical damage of carbon-epoxy laminates without and with embedded PZTs. A significant amount of research has detailed the failure mechanism of quasi-isotropic composite laminates without PZTs, including various carbon-epoxy materials with similar or identical material properties as the material studied in this report. Much of the research has been shown to be consistent and repeatable, which is further discussed in the Fatigue Strength of Composite Structures sub-section. However, very limited structural integrity research has been conducted on laminates with PZTs. Most of the mechanical effects research has used representative embedded devices, such as glass inserts or glass-epoxy, which is discussed in the structural integrity effects of embedded devices sub-section. Although the primary concern is the mechanical effect of embedding the sensor, some insight of the failure mechanism of the embedded sensor is desired as well. Therefore, the electro-mechanical constitutive behavior and low-strain fatigue response of PZTs are discussed in the last two research sub-sections.

#### **2.1.1 Fatigue Strength of Composite Structures**

Fatigue of carbon-epoxy, quasi-isotropic laminates has been detailed in many reports. Among these reports, Kim gives a detailed assessment of the progression of damage during quasi-static and tension-tension fatigue loading of quasi-isotropic T300/5208 carbon-epoxy specimens [12]. The results of Kim's tests show an average ultimate quasi-static strength of  $583 \text{ MPa}$ , where the range of the 28 specimens was  $496.7 \text{ MPa}$  to  $643.5 \text{ MPa}$ . Between 77-83 % of the ultimate static strength, fatigue cycling at 10 Hz resulted in failure within 10,000

cycles. At 71 % and 64% stress levels, the cycles to failure were less than 80,000 and 326,000 cycles respectively. Finally, at 59 %, the cycles to failure were less than 1.4 million.

Kim discusses the four basic failure mechanisms: matrix cracking, delamination, fiber breakage, and interfacial debonding. In general, fatigue failure in composites occurs after extensive damage has been generated throughout the specimen, as opposed to a single crack propagating at one location. As the four basic failure mechanisms occur, a reduction in fatigue strength and stiffness results. The type and sequence of the failure mechanism depends upon the lay-up, the material, and the type of loading. Static and fatigue loading generally result in similar damage sequences, except that fatigue loading causes damage at lower stress levels as a function of the number of cycles.

When considering matrix cracking in a multidirectional laminate, failure usually first occurs in the weakest ply. Subsequent failures generally occur as a function of strength; the strongest plies fail last. As stress is increased, the number of cracks in the matrix increases to a final crack density limit. At this point, new cracks may not appear until ultimate failure. In general, more cracks will result from fatigue loading as compared to static loading, where the crack density limit might not be reached. This may be explained in part by the multiplication effect of fatigue. In fatigue loading, many axial cracks may initiate from the transverse cracking of the matrix. After the cycles increase, the axial cracks extend upward, thereby potentially generating more cracking. Most of the crack multiplication effects occur within the first 20% of the fatigue life. In a  $[0 | \pm 45 | 90]_S$  lay-up, the  $90^\circ$  plies transversely crack first, with the  $45^\circ$  plies cracking at higher loads. The  $0^\circ$  plies may even experience some cracking in the matrix due to transverse stresses, which are usually small for longitudinally loaded specimens.

Delamination is caused by highly localized interlaminar stresses at the free edge of the specimen. The interlaminar stresses are highly dependant upon the type of laminate, stacking

sequence, properties of the constituent materials, and type of loading. For the classical quasi-isotropic  $[0|\pm 45|90]_S$  lay-up, extensive delamination under static tension is expected and experimentally seen. The delamination first extends down the entire length of the specimen, then proceeds to grow towards the middle of the specimen under increasing loads. Delamination usually occurs at lower stress levels for fatigue loading than for static loading. The change in the delamination path usually occurs at transverse cracks, which appear to be a significant factor for the start of delaminations.

Fiber break and interface debonding is the fourth basic failure mechanism discussed by Kim. For a composite with a polymer matrix that has a higher ultimate strain than the carbon fibers, fibers can break before the matrix-fiber interface fails. At this localized point, cracks may start and grow in the matrix or interface. If the bonding is strong between the matrix and fibers, the crack grows into the matrix, resulting in a smooth failure surface across the section. Where there is weak bonding, interfacial debonding in the form of fiber pullout and irregular surface failure results. For most advanced composites, interface bonding is strong, so fatigue damage can be considered negligible, except at the area of fiber breakage.

Other reports generally agree with the damage sequence discussed by Kim [11, 15, 20]. Stinchcomb gives a graphical representations of the cumulative damage sequence and interlaminar stresses resulting from transverse cracking [21]. Figure 1 shows the progressive damage to failure of the laminate. Figure 2 shows the interlaminar shear and normal stresses which result from the cracking of the  $90^\circ$  plies of a quasi-isotropic  $[0|\pm 45|90]_S$  laminate. Results of Stinchcomb's testing of notched carbon-epoxy specimens under complete reversed loading are shown in Figures 3 and 4. The higher loaded specimen's stiffness drops faster and fails in less cycles, but the relative damage during the life is approximately the same as shown in the Figure 4.

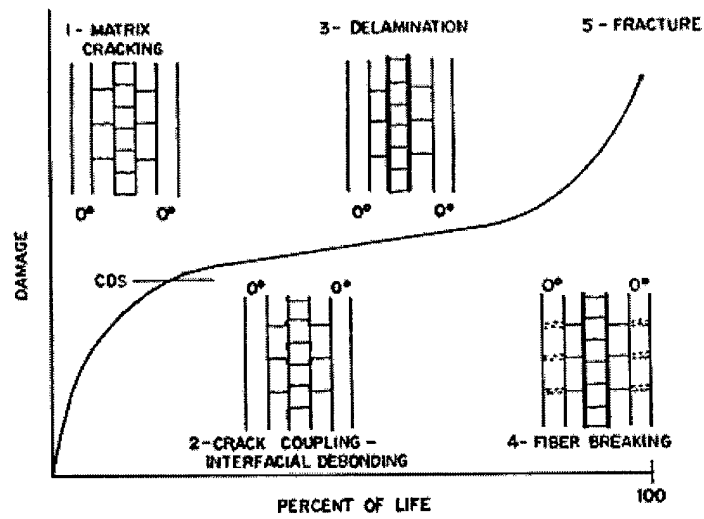


Figure 1. Damage Sequence During Fatigue Loading [21]

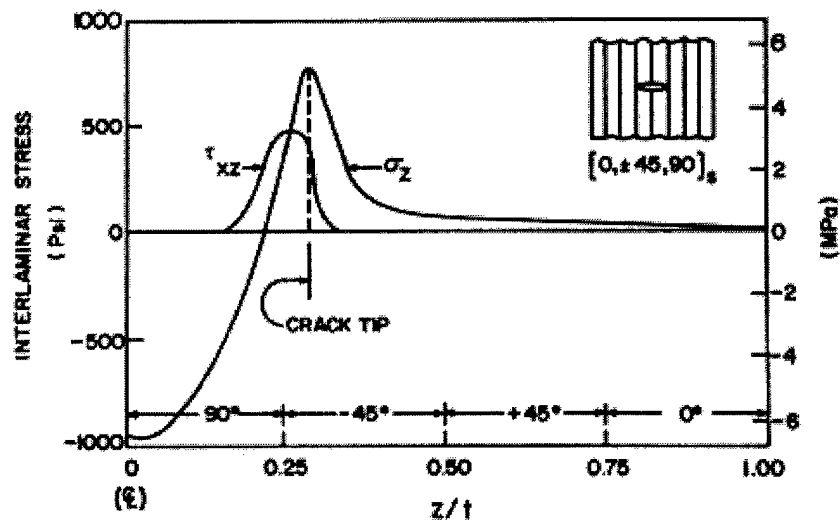


Figure 2. Interlaminar Stresses Near the Crack Tip [21]

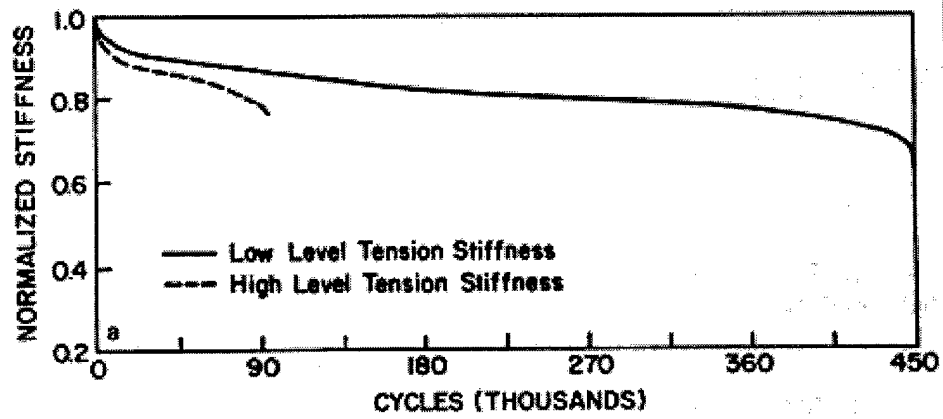


Figure 3. Normalized Stiffness vs Cycles [21]

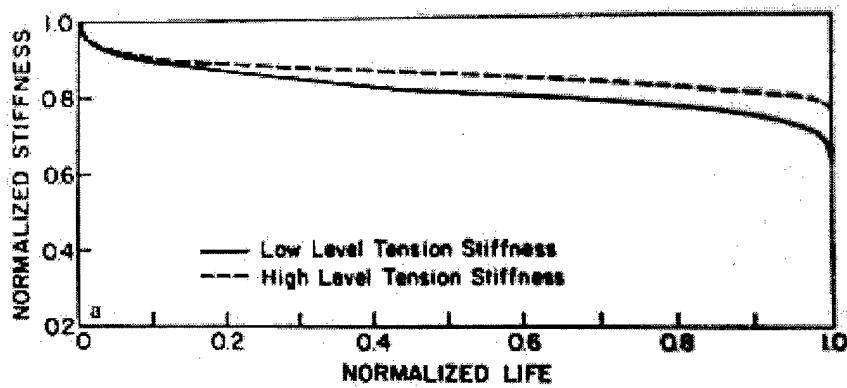


Figure 4. Normalized Stiffness vs Normalized Cycles [21]

The primary purpose of a report by Masters and Reifsnider was to qualitatively and quantitatively describe the cumulative damage development of quasi-isotropic carbon-epoxy laminates [16]. The material studied in this investigation was the Hercules AS/3501-5 graphite-epoxy pre-preg. The two laminates were  $[0 | \pm 45 | 90]_S$  and  $[0 | 90 | \pm 45]_S$ . The test was tension-tension fatigue at constant amplitude, where the specimens were tested for 1 million cycles at or below the first-ply failure stress. The average ultimate stress of the first laminate was 602 *MPa*, while first-ply failure stress was calculated to be approximately 275.7 *MPa*.

Quasi-static load results for the  $[0 | \pm 45 | 90]_S$  laminate were very similar to those reported by Kim [12]. Initially, the 90° plies transversely cracked, until eventually a crack saturation spacing was achieved. As the stress was increased, the adjacent -45° plies cracked, until they once again achieved a crack saturation spacing. At about the same point of -45° cracking, longitudinal cracking occurred. Eventually, the cracks joined together down the length of the edge, forming a delamination. As the load was increased further, the delamination gap widened further. During the entire process, only a few +45° plies cracked before failure. Saturation spacing of the cracks was approximately 0.756 *mm* in most cases.

Fatigue results given by Masters and Reifsnider were very similar to the quasi-static results. After just a few cycles at 275.7 *MPa*, similar crack saturation spacing in the 90° and -45° plies resulted. Some frequency effects were noted, where higher frequency tends to increase the number of cycles required to achieve the saturation spacing. These fatigue tests were run at 15 *Hz*.

To address the questions involving the failure process, Masters and Reifsnider quote from Stinchcomb [16, 19].

“Although we can detect, identify, and monitor damage details during the process of failure, we do not understand how the individual details combine to form the damage state which controls the

fracture of the materials.”

The main point is that our understanding of the exact details of material interactions that control fracture is somewhat limited even today, which necessitates the experimental testing of composites.

### **2.1.2 Structural Integrity Effects of Embedded Devices**

In 1997, Hansen and Vizzini studied interlacing techniques to improve on the static and fatigue strength (tension-tension) of embedded glass microscope slides in carbon-epoxy composites [9]. Hercules AS4/3501-6 graphite epoxy prepreg was used to manufacture the laminates. The  $50\text{ mm} \times 25\text{ mm} \times 1\text{ mm}$ , glass slides were used to represent embedded sensors or actuators in smart or multi-functional structures. The thickness of the glass slides was approximately 2 plies, while the width spanned the entire width of the specimen ( $50\text{ mm}$ ). The location of the slides varied with different types of interlacing techniques. The surface of the slides were scuffed with sandpaper in order to improve the adhesion with the plies. In order to detect and monitor the damage in the specimens, dye penetrant and X-ray analysis were used. Strain gages were attached on the surface at the slide/ply interface and far-field locations.

Results showed major differences in static and fatigue strength for the different embedding techniques. The first method involved cutting-out an area to embed the slides, leaving a resin rich pocket between the cut-out plies and the slide. Two other dispersed-interlace techniques were employed by separating the cut-out plies and interlacing them with continuous plies, thereby distributing the discontinuity through the thickness of the laminate. The dispersed-interlacing techniques showed improved damage resistance and decreased delamination, which resulted in greatly increasing the fatigue life. The pure cut-out method resulted in severe delamination and crack initiation around the slide, but the ultimate static strength was over 130 %

greater than the other insertion methods. Some conclusions were that the performance of the host structure and lifetime of the embedded device are severely degraded by simply using the cut-out method, since the damage resistance to delamination is much lower.

An earlier report in 1995 by Shukla and Vizzini using similar techniques showed different results [17]. 24-ply unidirectional laminates were used with embedded glass slides, but the slides in this case were 6 plies thick. Understandably, the first conclusion was that the ultimate strength was reduced by 28 % by cutting out plies for embedding the slide. Cutting out the 6 plies across the entire width of the specimen effectively reduces the load carrying plies to approximately 18, which gives a quick rough estimate of a 25 % reduction of strength. This report further indicates an improvement of a factor of two in ultimate strength by using the dispersed-interlace method. This increase in ultimate strength is clearly in contrast to the report in 1997. Both reports conclude the interlacing techniques improve the initiation of transverse cracking and edge effects.

In 1993, Singh and Vizzini discuss further how cutting out plies reduce the strength of laminates by 15-20 % [18]. References to Warkentin and Crawley, and Crawley and de Luis showed that glass-epoxy and graphic epoxy coupons showed decrease in strength from inserting embedded piezoceramics and silicon chips. Upon further inspection, these reports only tentatively suggest the decrease, since the number of tests was minimal (4) and the difference could be within expected variances. In addition, both cases cut-out load carrying  $0^\circ$  plies, which suggest a significant degradation by design [22,23].

### **2.1.3 Electro-Mechanical Behavior of PZTs**

In studies done by Lynch, different samples of ferroelectric ceramic PZTs were tested under combined stress and electric field loading, including lead lanthanum zirconate titanate [13, 14]. The piezoelectric materials were not embedded or attached to the surface of any struc-



ture. Strain gages were attached directly to the specimens, which were loaded in compression by aluminum spacers. After certain stress levels were reached, the specimens were electrically loaded. After the last stress level, the load was ramped back down to zero for further electrical loading. The direction of the applied mechanical and electrical loads were opposite to the original polarization of the material. Therefore, the remnant strain from original polarization was compressed back both mechanically and electrically. Strain, electric displacement, polarity, and stress were measured in different planes to compare the effects of mechanical and electrical depolarization. "Softer" or lower yield materials saw immediate depolarization due to the mechanical stress and electric field applied. The effects were shown in a hysteresis curve, where residual strain was seen after the removal of the load. "Harder" materials showed less hysteresis effects due to depolarization and much less residual strain. Comparisons were made based upon the degree of depoling and ultimately the "switching" of the polarization.

"Switching" is a term used by Lynch to describe types of depoling which can occur with mechanical and electrical loads. A material fully poled in the desired direction will cause a remnant strain or lengthening of the material in the direction of the polarity. When the material is compressed, the remnant strain and polarization can be decreased. When tension is applied to the fully polarized material, no further polarization or remnant strain can be achieved. Compression loading "switches" the polarity of atoms or molecules by  $90^\circ$ . Electrical depoling can switch the polarity by  $180^\circ$ , where the atomic structure flips  $180^\circ$ , creating a net dipole moment in the opposite direction. This is achieved by applying an electric field directly opposite the polarization. The ability of the atoms or molecules to realign is explained by a dielectric inclusion effect, which basically depends on the grain boundaries and residual stresses already found in the material. Figure 5 shows how the applied stress ( $\sigma$ ) or electric field (E) can cause a switch-

ing effect of the polarity (P). The tetragonal shaped lattice is representative of a piezoelectric material [13, 14].

#### **2.1.4 Low Strain Fatigue Response**

Bronowicki et al focused on testing embedded PZTs at or below the ultimate tensile strain of the PZT [1]. Specimens were subjected to tension and compression loading, and thermal cycling for hundreds of cycles. Static response for applied voltages was also conducted. Stiffness changes were measured through changes in the first and second mode frequencies. Dynamic performance was obtained by measuring the dynamic transfer function between the applied voltage to the measured voltage at the sensor. A specially designed test set-up was required to monitor these parameters. Test results showed correlation to the analytic predictions, using the manufacturer's data for the PZT modulus and piezoelectric coefficient. The ultimate strains for the two types of PZTs were 600 and 1500  $\mu\epsilon$ . At approximately 60 % of the ultimate strains, there was no observed degradation in dynamic actuation/sensing performance. When the ultimate strain was reached, degradation of 13 % resulted. Changes in the modal frequencies due to the static tests were on average 1 to 1.4 %, depending on the fatigue schedule. The loss of stiffness was attributed to a combination of PZT and matrix cracking, fiber breakage, and end fitting bond deterioration. Dynamic testing showed that the actuator-sensor feedthrough was initially enhanced, possibly due to laminate damage. When the dynamic testing was at the ultimate strain level, the feedthrough dropped by 12 %.

A similar report by Doran and Butler only studied the static actuation behavior of embedded PZTs. Stress-strain relationships and piezoelectric relations were used to predict the electro-mechanical behavior [7]. Experimental results were then compared with theoretical results. The comparisons showed some differences, which were attributed to the error in the Young's modulus of the PZT. In addition, this report briefly overviews some of the difficulties in embedding

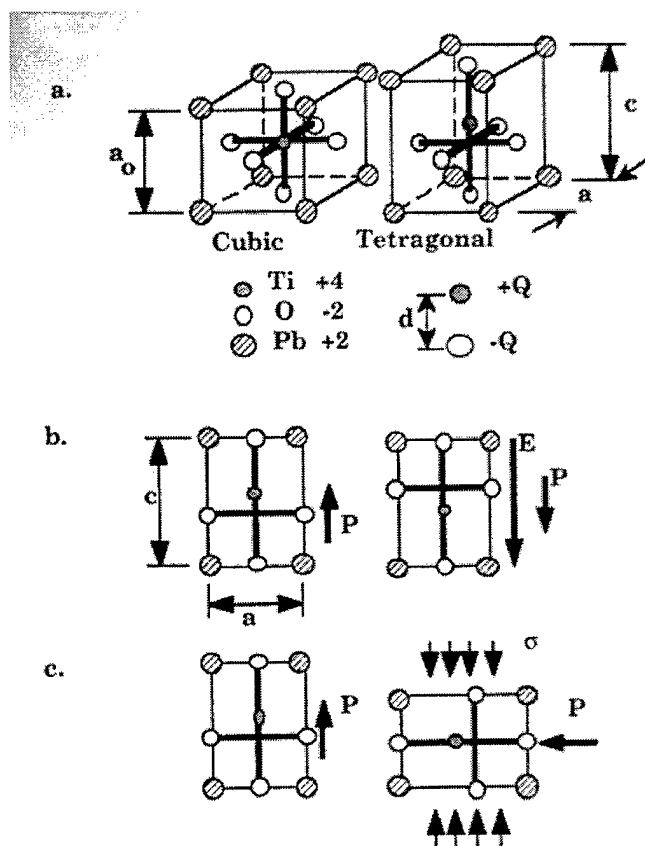


Figure 5. Switching of Polarity Due to Applied Stress and Electric Field [13]

PZTs for aerospace utilization. The extremely brittle nature of ceramics and the requirement for thinner elements are among the problems discussed.

## 2.2 Theory

The review of past research covers much of the theory behind damage mechanisms in composites, effects of embedded devices, and electro-mechanical behavior of PZTs. This section focuses on filling some of the gaps through the theory of piezoelectric materials and composites. The piezoelectric theory is primarily taken from Brei's instructional papers, while the composite theory is taken from the text, "Engineering Mechanics of Composite Materials," Daniel and Ishai [3, 6].

### 2.2.1 Piezoelectric Material Theory

In general, piezoelectric materials normally have no center of symmetry below a certain Curie temperature, which enables a dipole state to occur. Above the Curie temperature, the structure transitions to a "centrosymmetric" lattice, where the negative and positive charges coincide. Piezoelectric materials are made by applying an electromagnetic field at a temperature slightly below the Curie temperature. The electromagnetic field aligns the dipoles into regions known as Weiss domains. In a Weiss domain, a net dipole moment occurs, which in-turn results in a net polarization of the material. Equation 1 shows the basic relation between the electric displacement ( $D$ ), the electric field ( $E$ ), and the polarization ( $P$ ), where " $\epsilon_0$ " is the permittivity of free space.

$$D = \epsilon_0 \times E + P \quad (1)$$

The polarization process is reversible as well, following a dielectric hysteresis curve. Figure 6 shows the dielectric hysteresis loop from initial positive polarization, reversal, then back to positive. As indicated earlier, polarization occurs when the material is held at a temperature

slightly below the Curie temperature and a strong electric field is applied. When no further polarization can be achieved, this point is indicated as the saturation polarization. When the electric field is taken away, alignment relaxes slightly resulting in a small drop to the remanent polarization. Applying a negative electric field decreases the polarization down the left side of the hysteresis curve until the negative saturation polarization is achieved. Once again, when the electric field is removed, the negative remanent polarization results. Applying the positive electric field again, the polarity increases along the right side of the hysteresis curve.

Another effect of the poling treatment (electric field + heat) is the lengthening of the material in the direction of the electric field. The curve below the polarization hysteresis curve in Figure 6 is the strain which is induced as a result of the polarization. S3 is the strain along the direction of the electric field, while S1 and S2 are the strains perpendicular to the field. Notice at the remanent polarization, there exists a remanent strain of the material parallel to the electric field. This property may explain some embedded actuator test results found later in this report.

A number of other properties of the PZTs should be discussed in support of this research. First, the PZT can be cyclically loaded via stress or voltage to achieve a desired cyclic voltage or strain correspondingly. Second, the PZT are temperature and frequency dependant, so comparison tests will be conducted at the same frequency and approximately the same temperature. Third, PZTs have a tendency to depolarize due to exposure to strong electric fields, high mechanical cycling, and high temperatures. The effects of mechanical cycling near the design limits is discussed in the second half of this report.

The PZT QP15N from Active Control eXperts (ACX), used in this study, has been designed to be a sensor or an actuator. As a cyclic load is applied to the actuator, a cyclic voltage, approximately linearly proportional to the applied stress is generated. In this mode, the PZT can be considered a sensor. If a cyclic voltage is applied, the PZT would extend or contract cycli-

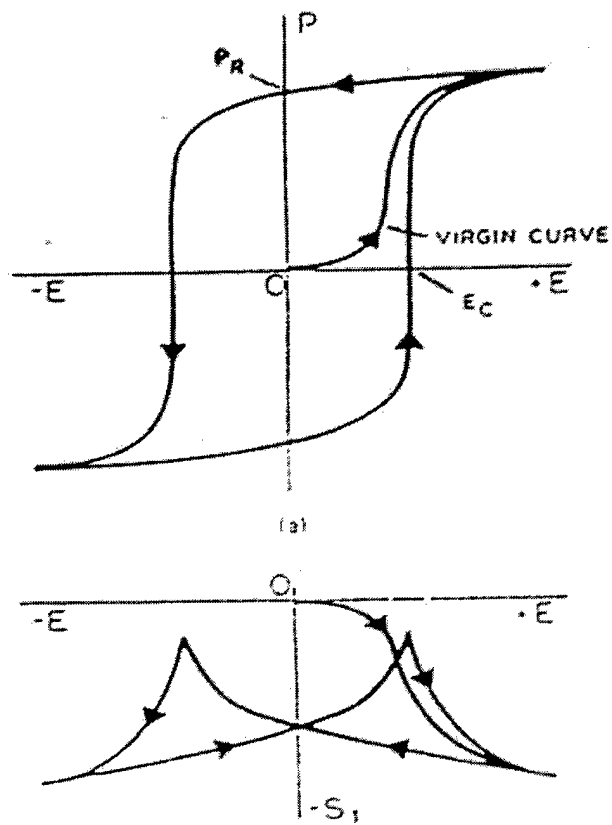


Figure 6. Polarization vs Electric Field Hysteresis Loop [3]

cally. In this mode, the PZT would be an actuator. This research report will take sensor data from the PZT during mechanical fatigue testing. Capacitance measurements will also be taken to monitor the health of the sensor. If mechanical deformation of the PZT occurs, two results could occur. First, the change in shape may cause a permanent deformation of the PZT resulting in a change of capacitance. This change can be theoretically calculated by Equation 2, where  $K_3^T$  is the dielectric constant,  $\epsilon_0$  is the permittivity of free space,  $l$  is the length,  $w$  is the width, and  $t$  is the thickness of the capacitor. From discussions with ACX, if the deformation causes cracking or lead wire damage, the capacitance should drop noticeably, regardless of the change of thickness.

$$\text{Plate Capacitance (F)} = \frac{K_3^T * \epsilon_0 * l * w}{t} \quad (2)$$

## 2.2.2 Composite Material Theory

### 2.2.2.1 Background

Composites are generally made up of a fiber and matrix phase. In the case of AS4/3501-6 pre-preg, thousands of AS4 carbon fibers run continuously along the longitudinal length of a single ply. The epoxy matrix surrounds the fibers and provides a mechanism for load transfer and structural integrity. Pre-preg indicates the manufacturer has made rolls of plies which have the fibers and pre-cured matrix already combined. The pre-preg material can be cut and stacked into a composite lay-up, where each ply could have a different angle. The  $0^\circ$  ply has the fibers in the longitudinal direction or parallel to the direction of the primary load. Different angle plies, such as  $45^\circ$  and  $90^\circ$  are from the same pre-preg roll, but are turned at an angle during the lay-up process.  $[0|\pm 45|90]_S$ , indicates an eight ply lay-up, symmetric about the middle  $90^\circ$  plies.

In order to calculate the elastic behavior of laminae, the generalized stress-strain relations shown in Equations 3 and 4 can be used.  $[\sigma]$  is the stress matrix,  $[Q]$  is the stiffness matrix,  $[S]$

is the compliance matrix, and  $[\varepsilon]$  is the strain matrix.

$$[\sigma] = [Q] * [\varepsilon] \quad (3)$$

$$[\varepsilon] = [S] * [\sigma] \quad (4)$$

The number of variables in the matrices can be reduced significantly by conservation of energy and the type of laminate being studied. Since the laminate in this study is a quasi-isotropic lay-up, only those particular equations required will be given without the extensive derivation. When dealing with thin plates (plane stress), Equations 3 and 4 can be reduced to 2-dimensional problems, where the compliance matrix reduces to a  $3 \times 3$ . For a unidirectional lamina, the stress-strain relations are shown in Equations 5 and 6.

$$\begin{pmatrix} \sigma_1 \\ \sigma_2 \\ \tau_6 \end{pmatrix} = \begin{bmatrix} Q_{11} & Q_{12} & 0 \\ Q_{12} & Q_{22} & 0 \\ 0 & 0 & Q_{66} \end{bmatrix} * \begin{pmatrix} \varepsilon_1 \\ \varepsilon_2 \\ \gamma_6 \end{pmatrix} \quad (5)$$

$$\begin{pmatrix} \varepsilon_1 \\ \varepsilon_2 \\ \gamma_6 \end{pmatrix} = \begin{bmatrix} S_{11} & S_{12} & 0 \\ S_{12} & S_{22} & 0 \\ 0 & 0 & S_{66} \end{bmatrix} * \begin{pmatrix} \sigma_1 \\ \sigma_2 \\ \tau_6 \end{pmatrix} \quad (6)$$

In order to obtain the transformation of these stresses and strains at different angles, a transformation matrix can be used. Equation 7 shows a typical transformation matrix, where  $c$  is the cosine of the rotated angle, and  $s$  is the sine of the rotated angle.

$$\begin{bmatrix} c^2 & s^2 & 2cs \\ s^2 & c^2 & -2cs \\ -cs & cs & (c^2 - s^2) \end{bmatrix} \quad (7)$$

For multi-directional laminates, moments and forces must be taken into consideration, since the material varies through the thickness. Usually, the moments and forces are related by the mid-plane strain. Skipping much of the derivations, symmetric laminates have zero coupling stiffness, so the primary concern for tension loading is the extensional stiffness  $[A]$



or the extensional compliance  $[a]$ . The force-displacement relation is shown in Equation 8, where  $N_i$  and  $\varepsilon_i^0$  are the appropriate forces and mid-plane strain respectively in an orthogonal coordinate system.  $A_{sx}$ ,  $A_{sy}$ ,  $A_{xs}$  and  $A_{ys}$  are zero for balanced laminates.

$$\begin{pmatrix} N_x \\ N_y \\ N_s \end{pmatrix} = \begin{bmatrix} A_{xx} & A_{yx} & A_{xs} \\ A_{yx} & A_{yy} & A_{ys} \\ A_{sx} & A_{sy} & A_{ss} \end{bmatrix} * \begin{pmatrix} \varepsilon_x^0 \\ \varepsilon_y^0 \\ \gamma_s^0 \end{pmatrix} \quad (8)$$

For a  $[0|\pm 45|90]_S$  quasi-isotropic laminate, the stiffness equations have already been derived in composite textbooks. The list of equations below summarize the equations used to estimate the modulus of the AS4/3501-6 laminate, where  $E$  and  $G$  are the Young's and shear modulus for each ply,  $\nu$  is Poisson's Ratio for each ply,  $t$  is the thickness of the laminate, and  $\bar{E}_x$  is the modulus for the laminate.

$$\begin{aligned} Q_{11} &= \frac{E_1}{1 - \nu_{12} * \nu_{21}} \\ Q_{22} &= \frac{E_2}{1 - \nu_{12} * \nu_{21}} \\ Q_{12} &= \frac{\nu_{12} * E_2}{1 - \nu_{12} * \nu_{21}} \\ Q_{66} &= G_{12} \\ Q_{xx}(\theta = 0) &= Q_{11} \\ Q_{xx}(\theta = 90) &= Q_{22} \\ Q_{xx}(\theta = 45) &= \frac{1}{4} * (Q_{11} + Q_{22} + 2 * Q_{12} + 4 * Q_{66}) \\ A_{xx} &= \frac{t}{8} * (3 * Q_{11} + 3 * Q_{22} + 2 * Q_{12} + 4 * Q_{66}) \\ A_{yy} &= A_{xx} \\ A_{xy} &= \frac{t}{8} * (6 * Q_{12} + Q_{11} + Q_{22} - 4 * Q_{66}) \\ \bar{E}_x &= \frac{1}{t} * \left( A_{xx} - \frac{(A_{xy})^2}{A_{xx}} \right) \end{aligned} \quad (9)$$

Failure of composites has been described in literature via micro-mechanical and macro-mechanical theories. In micro-mechanical theory, individual fiber strengths and matrix strengths are used to describe the failure mechanism. Usually, the fibers are usually the strength behind the composite, while the matrix distributes the load and holds the composite together. After calculating the volume percent of fibers or matrix, one can determine a ply's strength based upon the combination. In macromechanical theory, a global view of the composite is taken. When studied from a macroscopic viewpoint, a composite material may be considered homogeneous and anisotropic, whereas from a micromechanics view, this same composite could be considered heterogeneous and isotropic. In composites, failure by ultimate stress or strain usually refers to complete failure of the composite. First-ply failure (FPF) is another failure criteria, which is usually higher than the design loads.

#### **2.2.2.2 Micromechanics Theory**

In micromechanics, the mechanical properties of the matrix and fiber phases are combined to predict the overall strength of the lay-up. As expected, the epoxy matrix will normally fail first due to the lower ultimate transverse strain.

$$\sigma_1 = (\sigma_f \times V_f) + (\sigma_m \times V_m) \quad (10)$$

$\sigma_f, \sigma_m$  = Average longitudinal stresses in the fiber and matrix, respectively

$V_f, V_m$  = Fiber and matrix volume ratios, respectively

As indicated above, the fiber and matrix phases have different stresses, because of the different material properties of each. When combined in a single 0° ply and pulled in tension, both the matrix and fibers are stretched to the same strain level. More stress is required to pull the fibers the same distance, since the fibers' modulus is higher.

At the fiber/matrix interface, interfacial shear stresses transfer the load across the ply. As the fibers or the matrix starts to break, the stress in the adjacent fibers and matrix increases. The interfacial stresses increase as well. As the stress levels increase, damage in adjacent areas coalesces to form a crack. During the damage sequence, the modulus of elasticity reduces until catastrophic failure occurs.

#### ***2.2.2.3 Macromechanical Theory***

The laminate used in this study is assumed to be a quasi-isotropic, homogeneous, symmetric lay-up. Quasi-isotropic refers to materials having the same elastic properties in all orientations in a given plane. Isotropic would refer to a composite that has the same material properties in all directions. The failure estimates used in this report are primarily based upon macromechanical failure theories.

Various methods have been used to determine theoretically the failure of a composite from known ply strengths; these methods include Maximum Stress, Maximum Strain, Deviatoric Strain Energy (Tsai-Hill), etc. Since the focus of this research was not on comparing failure theory with experimental results, a reasonable estimate of FPF was achieved by using the Maximum Strain Theory. Simply, the ultimate transverse strain level for a unidirectional laminate was taken from previous research. After the modulus for the laminate was determined, the stress required to achieve the ultimate strain in the  $90^\circ$  plies was calculated using the simple stress/strain relationship. The theoretical level of FPF was used to approximately determine when to expect cracking the composite. The levels of stresses for transverse cracking between specimens with and without actuators were then compared. Since different lots of pre-pregs could result in some variation in material properties, the primary comparison is between tested specimens and not with past research.

To address Maximum Strain Theory more specifically, the stress components along the principal material axes are first determined by stress transformation, then the corresponding strain components are obtained by the lamina stress-strain relations.

$$e_1 = (1/E_1) * (\sigma_1 - \nu_{12} * \sigma_2) \quad (11)$$

$$e_2 = (1/E_2) * (\sigma_2 - \nu_{21} * \sigma_1) \quad (12)$$

$$\gamma_6 = \tau_6/G_{12} \quad (13)$$

From this point, the ultimate stresses are solved from the given ultimate strains calculated in the above equations.

As the damage in the laminate progresses, ply-discount method is one way to account for the change in strength. Basically, ply-discount method reduces or zeros out the stiffness of the failed plies and takes into account an effective area for applied stress. When the failed ply stiffness is set to zero, the overall laminate modulus decreases. The reduction of the effective area results in an increase of the stress on the remaining plies. For example, if two plies out of eight fail, the effective area is reduced by a factor of 25 %. This reduction results in a  $\frac{8}{6}$  increase in the stress to the remaining plies. Ply-discount method calculations for this report are provided in Appendix B.

### 3. Testing Preparation and Procedures

#### 3.1 Test Set up

As discussed by Warkentin, the construction of smart structures must prevent damage of the embedded sensors, provide a stable operating environment, fulfill processing requirements, and minimize the degradation of the structural properties [23]. After a literature research and discussions with experts in this area, the test specimen design was chosen based upon practical experience and lessons learned from similar experiments. The experimental procedure focused upon two primary areas of concern: the structural degradation effects of embedded sensors in the host structure, and the piezoelectric degradation of the embedded sensors when subjected to mechanical cyclic loading.

##### 3.1.1 Test Specimen Design

The carbon-epoxy material tested was a Hercules AS4/3501-6 pre-preg, which had a single ply thickness of approximately  $0.13 \text{ mm}$ . The piezoelectric actuator studied was a pre-packaged Active Control eXperts (ACX) QP15N, which consisted of the PZT, an outer isolation barrier similar in appearance to Kapton tape, and extended lead wires. The dimensions of the PZT were approximately  $50.8 \text{ mm} \times 25.4 \text{ mm} \times 0.254 \text{ mm}$ . The lead section extended to  $25.4 \text{ mm}$  from the base of the PZT, had a width of  $12.7 \text{ mm}$ , and was surrounded by the same epoxy isolation barrier. Figure 7 shows a diagram of this sensor.

##### 3.1.1.1 Laminate Selection

The final laminate chosen in this study, after several iterations, was a classical quasi-isotropic  $[0 | \pm 45 | 90]_S$ , where the sensor was embedded at the mid-plane inside the two center  $90^\circ$  plies. This laminate was chosen based upon the multi-directional characteristics of similar laminates used in industry, the predicted effects of embedding PZTs, and the previous research

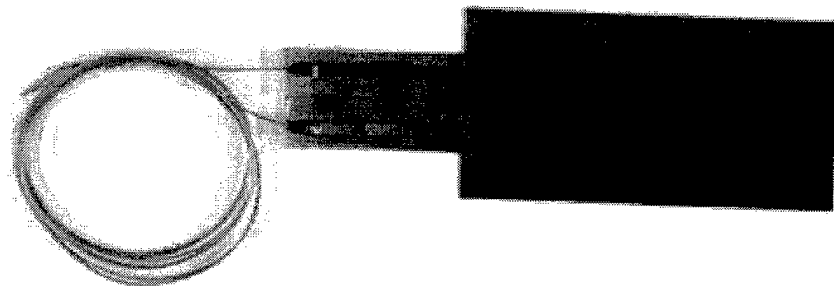


Figure 7. Active Control eXperts (ACX) QP15N PZT

found on this type of laminate. Symmetric laminates in industry would generally be thicker, with a larger percentage of  $0^\circ$  plies in the primary load bearing direction. Therefore, this laminate could be considered a worst case for embedding sensors/actuators in actual applications.

Initially, a  $[0|0|+45|-45|0|0|90]_S$  laminate was proposed and constructed, which provided increased strength in the longitudinal direction. After initial investigation, this laminate was changed, since the S-N curve would be relatively flat because of the fiber dominated strength. The effects of fatigue loading by embedding the sensors in the  $90^\circ$  plies would be very difficult to detect, since the  $90^\circ$  plies provide a very small percentage of the overall strength in this lay-up. A couple of tests were run with this laminate, which indicated a very flat S-N curve. Discussion of these tests is provided in Appendix D.

#### **3.1.1.2 Specimen Dimensions**

Two types of specimens were constructed, one with the sensor embedded and one without the sensor embedded. The dimensions of these two specimens were approximately the same, with the exception of some 25.4 mm wide specimens made to study the width effects. The size of the 305 mm  $\times$  50.8 mm specimens was primarily based upon the size of the embedded PZTs. In order to embed the 50.8 mm  $\times$  25.4 mm sensor, a 2:1 width and 6:1 length ratio were designed to limit edge and large inclusion effects. The actuators were normally centered in the middle of the specimens, except in one case where the PZT was placed at the edge of the specimen. This particular specimen was constructed to study the bonding interface of the PZT with the surrounding plies at the edge. This study basically involved the comparison of these two types of specimens when subjected to cyclic loading. Figure 8 is a diagram of a specimen with an embedded sensor.

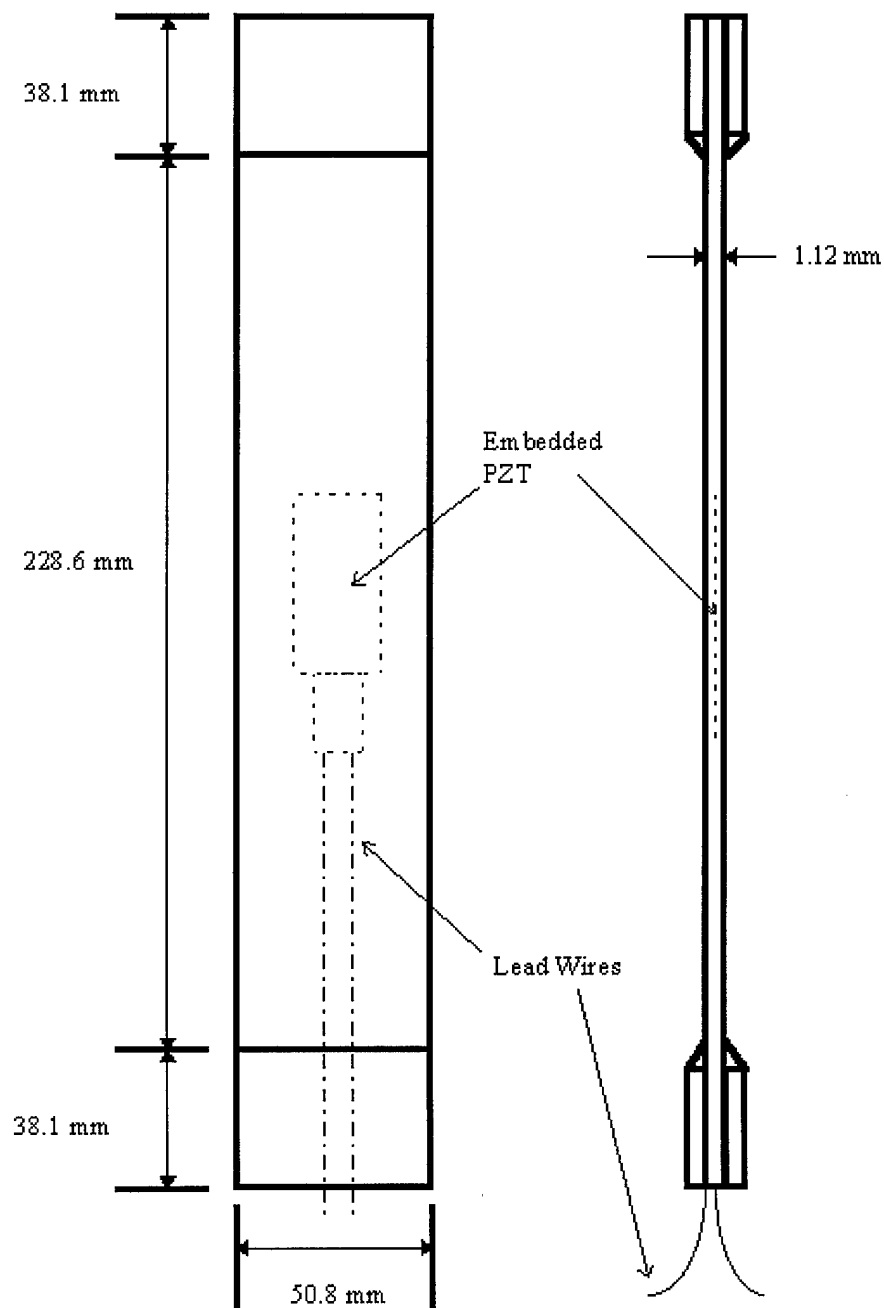


Figure 8. Diagram of Specimen with Embedded PZT



### 3.1.1.3 Manufacturing Method

Early in the laminate selection process, there was much discussion on whether to cut-out plies or to simply insert the sensors between the plies of the laminate. The cut-out method was selected, but not without some controversy. Obviously, there is a risk of strength reduction when plies are cut. In addition, the manufacturing method of cutting out holes in plies is more tedious than simply inserting the sensors in the middle. But, simply inserting sensors could change the thickness and surface properties of the composite. There was also some concern that the sensor might crack from residual stresses pinching the edges during the cure cycle, which has been reported in few previous studies [7, 10]. The perceived disadvantages outweighed the advantages of simply inserting sensors, therefore the cut-out method was employed. "Cutting the plies" versus "dropping them in" could be a study in itself, which is beyond the scope of this report. A diagram of the cut-out method is shown in Figure 9.

In order to ensure the health of the actuators and the prevention of obvious flaws during the manufacture of the specimens, processing experiments were conducted with the University of Dayton Research Institute (UDRI) in coordination with Non-metallic Division, Materials and Manufacturing Directorate, Wright Laboratory, Wright-Patterson Air Force Base, Ohio. Location of the actuator in the middle plies of the laminate was the configuration chosen. Each ply of AS4/3501-6 was approximately 0.13 mm thick, while the ACX piezoceramic actuator was approximately 0.254 mm thick. To accommodate the actuator/sensor, an approximate 50.8 mm by 25.4 mm area was cut-out from two 90° plies at the center of the laminate. Initially, aluminum pieces in place of the actuators were inserted in cut-out areas of a  $[0|0|\pm 45|0|0|90]_S$  laminate. Ultrasound technique was then used to ensure no voids or defects were introduced by the insertion. The panels were further inspected by cutting across the aluminum pieces and examining for debonded regions. After these preliminary tests were completed, two piezoelectric sensors

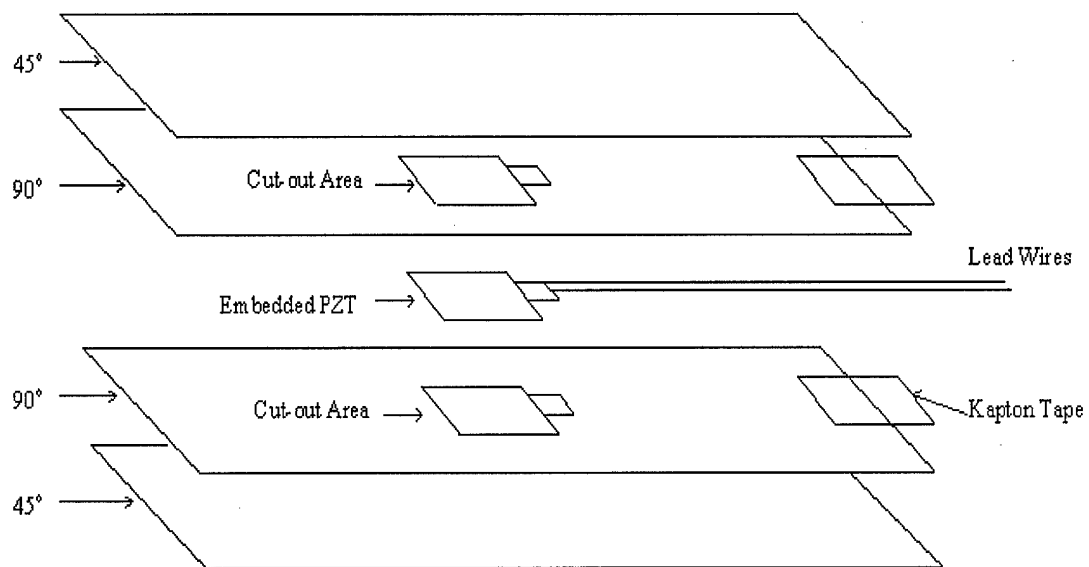


Figure 9. Diagram of Cut-out Plies and Inserted PZT in  $[0 | \pm 45 | 90]_S$  Laminate

were inserted using the same cut-out procedure. One actuator was previously determined to be faulty, while the “good” actuator’s capacitance was used to determine the electrical integrity of the system. One noticeable problem was the seepage of epoxy around the lead wires and the movement of the lead wires to the top edge of the panel. The excess epoxy and location of the lead wires tended to snap off the wires at the edge of the panel. The panel edge had to be cut around the ends to enable the wires to be resoldered. Tubing was tried to strengthen the wires at the edge, but this increased the epoxy funneling. Eventually, Kapton tape was used instead of the tubing to hold the wires in place. About 1.27 *cm* of tape was placed at the edge to prevent damage of the lead wires and maintain the center location at the edge. After this processing method was finally determined, the  $[0|\pm 45|90]_S$  lay-up was made in the same manner. The Kapton tape applied to protect the lead wires at the edge is shown in Figures 10 and 11. Figure 11 is an ultrasound image of a panel with the embedded PZTs.

The nominal panel size was approximately 30.5 *cm*  $\times$  30.5 *cm*, therefore four to five specimens were made from each panel. All the panels were made from the same pre-preg roll, but panels with sensors or without sensors were generally made separately. Panels without actuators had the same manufacturing method, with the exception of the cut-out areas.

After a panel has been prepared, the lay-up is then put into an autoclave as the final step in making the composite. The autoclave heats and cools the composite in a vacuum bag environment during a several hour process. The vacuum removes any volatiles trapped in the pre-preg or between the plies during lay-up. The autoclave heating elements are critical for the removal of volatiles, joining of the plies, and the final curing of the epoxy.

A couple of major concerns with the curing cycle were with the health of the embedded actuators. The maximum temperature of 176.7° *C* was close to the Curie transition temperature of the actuators, which could result in depoling. The depoling would result from the molecules

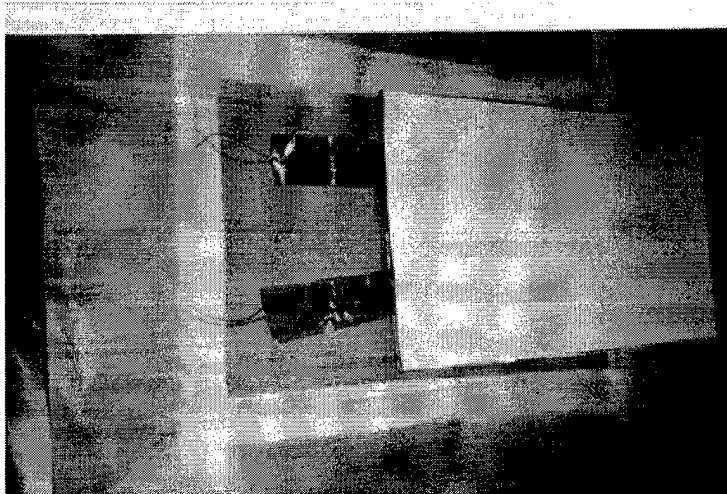


Figure 10. Kapton Tape Applied at the Ends to Protect Lead Wires

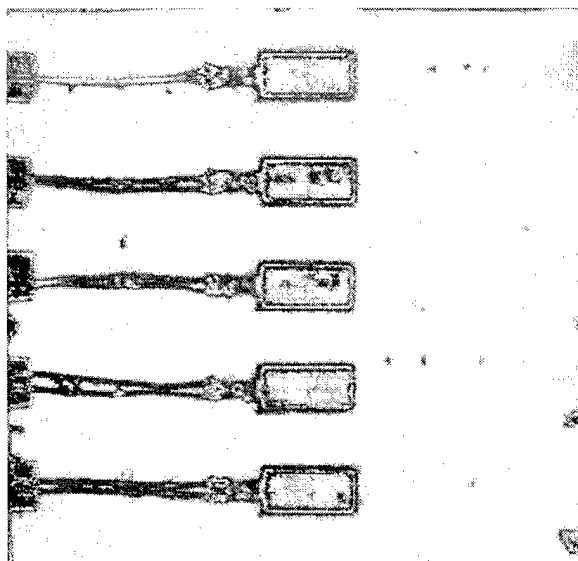


Figure 11. Ultrasound Inspection of Panel Embedded with Five PZTs

transitioning back to a more random state, thereby reducing the dipole moment created during the initial manufacturing process. Residual stress from the thermal cycling of the actuators was the other concern. There has been apparently some history of cracking in the actuators during the cure cycle, which degrades the performance of the actuators. The lead wires were connected together, as recommended by study under the SPICES program, to prevent cracking in the embedded actuators [10]. After discussing the cure cycle and shorting method with ACX, the manufacturer of the sensor, a standard cure cycle for AS4/3501-6 was used during the manufacture of the laminate. No significant variations in capacitance of the PZT was observed before and after the specimens were made. Actuator capacitance varied from 96  $nF$  to 100  $nF$  after the cure cycle, compared to the design specification of 100  $nF$ . Therefore, depoling and cracking did not occur during the manufacture of specimens in this study.

### **3.1.2 Strain Measurement**

A 101.6  $mm$  extensometer was selected to measure the longitudinal strain across the specimen with embedded sensor. Local strain gages were not used except in the case of specimen tested under monotonic loading, where progressive damage in the laminate was monitored. A Material Test System (MTS) Model 632.11B-20, GL 4.000, extensometer was attached to the edge of the specimen, encompassing the length where the sensor was located. Epoxy was used to prevent slippage of the extensometer knife edges during cycling. The Micro-Measurements, Measurement Group Incorporated, 120 ohm strain gages were used for the monotonic stress-strain response comparison of the two types of specimens.

### **3.1.3 PZT Sensor's Health and Its Output Measurement**

As the specimens were mechanically cycled, the voltage output of the PZTs were recorded via a voltage divider, MTS voltage meter, and computer software generated by Mr. Mark Der-

riso of AFIT. The 250 data points per cycle were recorded at many intervals during cycling, which is further discussed in the experimental procedure section. After discussions with ACX, a capacitance check at each cyclic interval was also conducted to monitor the health of the actuator. Generally, if the PZT was cracked or depoled, then the expected design capacitance should drop. A B+K Precision Dynascan Corporation 820 capacitance meter was used for this purpose. If capacitance dropped or was below an initial standard of  $95\text{ nF}$ , the PZT was repoled using a Hewlett Packard 3466A Digital Multimeter and a Bertan Associates Incorporated High Voltage Power Supply, Series 230.

#### **3.1.4 Damage Detection**

The primary tool used for the detection of transverse cracks was the Questar QM100 Remote Measurement System II (QRMS-II), which had an encoder resolution of 1 micron and a system resolution of approximately 5 microns. Magnification of the digital image to the computer monitor was approximately 500X. Once the edges of the specimens were polished, a strobe light and optics system could accurately detect transverse cracking when the specimen was put under a load. The QRMS-II optics system was also used to measure the initiation and width of the delamination at the edges. As this width of delamination grew to about a thickness of four plies, measurement with a standard ruler was conducted. When cracks could not be discerned, the specimen was removed and placed under a higher powered microscope (Nikon Epiphot) to inspect the edge. X-ray and ultrasound inspection was also used with specimens tested at the low-strain value to detect cracking.

#### **3.1.5 Material Test System**

The MTS 810 Material Test System (97,856  $N$ ) was used to conduct the tension-tension fatigue and monotonic testing, which was controlled by software developed by Mr. Mark Derriso

of Air Force Institute of Technology. The MTS grip alignment and strain gage calibration were accomplished per manufacturer's guidelines. In order to inspect the specimens, the QRMS-II was positioned in front of the MTS 810. A Tetronix TDS 420A was used to monitor the wave form of the cyclic load input. A picture of the test equipment is shown in Figure 12.

### **3.2 Experimental Procedure**

After the manufacture and design of the specimens, the experimental procedure was developed to investigate the mechanical effects of the embedded sensors. The experiment involved a control group of specimens without PZTs and specimens with the embedded PZTs. Specimens with embedded sensors were labeled with an "AT" prefix, while specimens without PZTs were labeled with the "FT" prefix. The 25.4 *mm* wide specimens were labelled "HP" and did not have PZTs. The first procedure involved monotonic testing, where the ultimate strength and damage sequence were investigated. After the monotonic testing was completed, the remaining specimens were tension-tension fatigued. Transverse cracking, primarily in the 90° plies, was tracked along with the extent of delamination. Modulus was recorded periodically during cycling to measure the extent of damage during the lifetime of the specimen. Specimens with actuators underwent the same test measurements, with the additional measurement of the actuator output voltage and capacitance. Since the stresses applied to the specimens resulted in strains which were several orders of magnitude greater than the actuator operational limits, an intermittent check at lower strains was also conducted to monitor the actuator's voltage output. For this purpose, the fatiguing of the specimen was stopped periodically, and a smaller load was applied over a few cycles. The last set of tests were conducted at low strain value to find the fatigue response of the embedded PZT near the operational limits. The details of the procedure are further described in the following paragraphs.

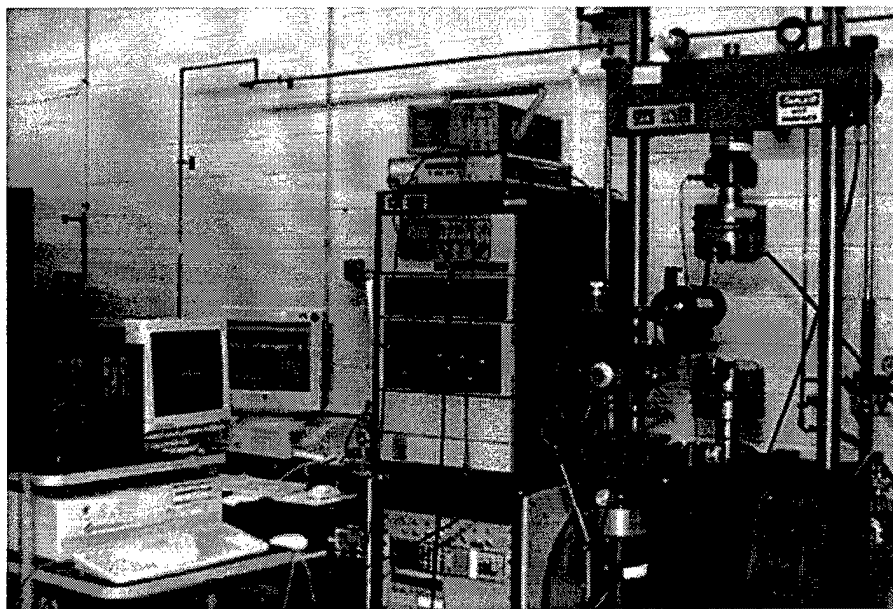


Figure 12. QRMS-II Optics, 810 MTS Test System, 486 Pentium Computers and Monitors



### 3.2.1 Monotonic Test Procedure

Before testing, each specimen's cross-section was measured with Scherr-Tumico micrometers (50.8 *mm* and 25.4 *mm*). The specimens were placed in the MTS 647 Hydraulic Wedge Grip, which was slightly modified to accommodate the 50.8 *mm* width. The grip pressure, based upon the MTS handbook, was set at 6.9 *MPa* for the static tests. The extensometer was attached by a modified spring-wire attachment, which was again required due to the relatively large width of the specimen.

Two types of monotonic testing were conducted in order to compare the damage progression and ultimate failure strengths of specimens with and without sensors. The first procedure involved progressive laminate failure, where the stress levels were ramped by 50 *MPa*, and the edge was inspected for transverse cracking at each level. Transverse cracking, longitudinal/axial cracking, and delamination levels were also recorded for each specimen using the QRMS-II optics system. After a stress of 350 *MPa* was reached, the specimens were monotonically loaded to ultimate failure. The general steps for analysis of progressive laminate failure during quasi-static or monotonic testing are given by Daniel and Ishai [6].

1. Determine analytically the First Ply Failure load from lamina stresses using maximum strain criterion.
2. The failed lamina or laminae are discounted by use of the ply-discount method. New laminate stiffnesses are then calculated.
3. Lamina stresses are recalculated and checked against the selected failure criterion to verify that the undamaged laminae do not fail immediately under their increased share of the stress following the FPF above.
4. The load is increased until the next ply failure occurs and steps 1, 2, and 3 above are repeated.
5. When remaining undamaged laminae cannot sustain the stresses, ultimate failure occurs.

The second test procedure involved monotonically loading of the specimens to failure without the intermittent stress damage inspection procedure as discussed above. The loading rate for this test was calculated based upon an expected ultimate strength and a maximum testing

time limit of 60 seconds (maximum load/60 seconds). The number of data points recorded during this test was kept under 500 to ensure the software limit was not reached. This test was to determine the classical shifts in modulus during the monotonic test before and after First-Ply-Failure (FPF) and subsequent ply failures. Further, ultimate strength obtained from these monotonically loaded specimens was used to get stress level estimates for the fatigue tests. The results of these tests are discussed in the stress-strain response section of the next chapter.

### **3.2.2 Fatigue Test Procedure**

In order to determine the fatigue response of the specimens, fatigue testing was done under tension-tension loading condition,  $R = 0.1$  (constant amplitude), and at a frequency of 10  $Hz$ . All fatigue tests consisted of mechanical loading only, where electrical actuation was not measured or applied. The first part of the fatigue testing was to establish S-N curves for specimens with and without embedded sensors. The goal was to determine the load levels which would cause failure in about ten thousand, one hundred thousand, and one million cycles. A total of eleven specimens were tested, which are detailed in the next chapter. During the entire cycling process, the damage sequence was tracked at pre-determined intervals. Transverse cracking, delamination depth and width, and modulus degradation were measured at 500, 1000, 5000, 10000, 50000, 100000, ... cycles until failure. For AT specimens, the capacitance and voltage output of the PZT was also recorded at the same time intervals. In addition, since the strain levels were far beyond the design upper limit of the PZT, the AT specimens were cycled at 10  $MPa$  and 76  $MPa$  in order to measure their voltage output at these intervals. These tests were conducted in order to investigate the integrity of the sensor under cyclic loading with the applied maximum strain value within the limits of the design value of the sensor. Tracking of some damage data was stopped after the upper limit was reached, such as transverse crack saturation spacing and negligible voltage output. Due to the extremely damaged edges after a

considerable number of cycles, the extensometer was taken off and only re-attached at the desired interval check point. In order to calculate capacitance changes due to thickness variation, the actual wafer size of the sensor was taken to be  $45.97\text{ mm} \times 20.57\text{ mm} \times 0.15\text{ mm}$  [2].

The second part of the fatigue test was the low-strain experiment, where the goal was to obtain strain versus cycles to failure relationship along with the PZT voltage output at the lower strain values. These low-strain tests were conducted at  $16\text{ Hz}$  in order to save time due to the long duration of these tests. Failure for this test was chosen to be a drop of at least 60 % of the original voltage output of the PZT. The applied strain levels for this test were near the maximum strains given by the manufacturer [2]. At  $200\text{ }\mu\epsilon$  and  $1000\text{ }\mu\epsilon$ , the expected lifetimes of the PZT were infinite and over ten million cycles respectively, but these life predictions did not take into account their embedment into the composite laminate. The level of stress in this case was far below the FPF of the composite, therefore no cracking was expected. Edge inspections by the QRMS-II optics and Nikon microscope were conducted periodically at the same intervals as discussed earlier. In addition, one specimen was sectioned so the edge of the PZT could be inspected directly for debonding and cracking of the epoxy rich zone. After microscope inspection, specimens were taken for X-ray and ultrasound inspection as well. The summary of all tests conducted in this study is provided in Table 1.

Table 1. Summary of Tested Specimens

Remarks	Specimen	Test Configuration	PZT Embedded (Yes/No)
Monotonically Loaded	FT0	Un-interrupted test	NO
	FT1	Un-interrupted test	NO
	FT7	Interrupted test	NO
	FT8	Un-interrupted test	NO
	ATST1	Interrupted test	YES
	ATST2	Un-interrupted test	YES
	HP3	Un-interrupted test, 25.4 mm width	NO
	HP4	Un-interrupted test, 25.4 mm width	NO
Fatigue Loading (tension-tension) ( $R = 0.1$ , 10 Hz)	FT2	$\sigma = 360 \text{ MPa}$	NO
	FT3	$\sigma = 380 \text{ MPa}$	NO
	FT4	$\sigma = 420 \text{ MPa}$	NO
	FT5	$\sigma = 440 \text{ MPa}$	NO
	FT6	Depth of delamination comparison	NO
	AT1	$\sigma = 380 \text{ MPa}$	YES
	AT2	$\sigma = 420 \text{ MPa}$	YES
	AT3	$\sigma = 440 \text{ MPa}$	YES
	AT4	$\sigma = 460 \text{ MPa}$	YES
	HP1	25.4 mm width, $\sigma = 420 \text{ MPa}$	NO
	HP2	25.4 mm width, $\sigma = 440 \text{ MPa}$	NO
Low Load Cycling (tension-tension) ( $R = 0.1$ , 16 Hz)	AT5	Off-set PZT, $\varepsilon = 200, 1000, 2000 \mu\varepsilon$	YES
	AT6	$\varepsilon = 1400 \mu\varepsilon$	YES
	AT7	$\varepsilon = 1250 \mu\varepsilon$	YES
	AT8	$\varepsilon = 1100 \mu\varepsilon$	YES

## 4. Results & Discussion

The results of the monotonic loading, fatigue loading, and low strain/sensor fatigue tests are discussed in this chapter. In each case, various material properties and damage mechanisms were measured. The degradation of the embedded sensor output is discussed separately for the monotonic, fatigue, and low strain level tests. Since the focus of the tests was primarily about the mechanical response, the theoretical electro-mechanical response of the PZTs is not discussed in great detail. Even so, the voltage output and capacitance of the PZTs were closely monitored in each test to indicate their response.

As stated in the test setup chapter, specimens were labelled to distinguish those with PZTs versus those without PZTs. "AT" specimens had a PZT embedded in the center 90° plies, while the "FT" specimens did not have a cut-out area or embedded PZT. "HP" specimens were 25.4 *mm* width specimens without PZTs used to compare width effects on the mechanical response of the specimens.

### 4.1 Monotonic Test Results

Overall, six specimens were monotonically loaded in tension to failure. The results of these tests are broken up into stress-strain response, damage mechanism, and degradation of PZT output. In order to measure strain more consistently at higher stress levels, which could not be accomplished due to slippage of the extensometer, the last two tests (ATST2 and FT8), had both strain gage and extensometer attached to measure the local strain at the middle of the actuator area and the average strain across the entire actuator length. These two specimens are compared in the first part of the section of stress-strain response. In order to document the damage sequence of the laminates, ATST1 and FT7 were loaded up at several intermediate levels and inspected for damage. These tests are summarized in the damage mechanism section. After

each intermediate stress, the load was removed, then specimen ATST1 was also briefly cycled at the actuator operational range (200 - 1000  $\mu\epsilon$ ) to measure the voltage output of the sensor. This test was conducted to find the level of stress which caused degradation on the actuator output during monotonic loading. The results of the electrical output degradation are provided in the last part of the monotonic loading section.

The other monotonic load tests were used to get an average ultimate strength of specimens with and without the embedded PZTs. This data was not only used for direct comparison of the ultimate strengths, but also for setting up the fatigue testing plan. Table 2 summarizes the ultimate strengths and modulus measured from each specimen and their averages. The resulting average ultimate strength and modulus were within 4% of each other, which is not very significant considering the relatively large embedded PZT. Compared to previous reports, the average strengths are lower in this study, which may be due to different lots of pre-preg. The variation range of the ultimate strengths are not uncommon, when compared to previous test results [12, 16].

#### **4.1.1 Stress-Strain Response of ATST2 and FT8 Specimens**

A comparison of the stress-strain curves (strain gage data) for specimens FT8 and ATST2 show little differences (Figure 13). FT8's stress-strain curve initially has a constant slope, but tends to start curving downward at 200 *MPa*, until a slight shift occurs at approximately 300 *MPa*. After this point, the slope more noticeably bends downward at 420 and 550 *MPa*. These changes in slope represent increasing damage in the specimen, which resulted in decreasing strength. The ultimate failure for FT8 occurred at 644 *MPa*. The same stress-strain response was then measured for ATST2, and the results have been overlaid upon FT8 in Figure 13. The FT8 and ATST2 curves mimic each other almost exactly, bending downward almost along the same path. The most notable difference between these was the lower ultimate strength

Table 2. Monotonically Loaded Specimens

Remark	Specimen	Ultimate Strength (MPa)	Young's Modulus (GPa)
Without PZT	FT0	510.0	51.4
	FT1	485.0	51.4
	FT7	544.6	49.5
	FT8*	643.6	49.0
	Average	545.8	50.3
With PZT	ATST1	504.0	50.6
	ATST2*	578.9	47.0
	Average	541.5	48.8
*The modulus was computed from strain gage data in these two specimens			

of ATST2, which was still above the average monotonic ultimate failure stress found from other specimens with and without PZT. Other specimens had very similar stress-strain responses, but the extensometer data was found to be skewed at higher loads, which is discussed further at the end of this subsection.

The noticeable shifts in the stress-strain curves and the corresponding changes in modulus correspond to transverse cracking, FPF,  $\pm 45^\circ$  plies failure, and other progressive delamination and axial cracking. Theoretical changes in modulus due to the failure of plies were estimated via Ply-Discount Method (See Appendix B). The changes in the experimental modulus after these noticeable shifts were calculated for comparison. Experimentally, FPF occurred at approximately 300 MPa, where the modulus decreased by approximately 5.3 %. The shift at 400 MPa corresponded to increasing damage in the  $45^\circ$  plies, where the modulus decreased by 11.2 %. Theoretically, the decrease in modulus after the  $-45^\circ$  plies fail was 18.4 %. Table 3 compares the calculated shifts from the theoretical Ply-Discount method versus the experimental shifts in the stress-strain curve. Ply-Discount method can be somewhat inaccurate, since it does not take into consideration complicated laminate damage properties, but does give a general estimate of damage progression.

As mention earlier, the extensometer data seemed skewed at higher loads, which led to the use of strain gages in the stress-strain response comparison. The strain gage data showed the shift in modulus before and after the damage such as FPF. From the extensometer data, the modulus remained relatively constant throughout, instead of showing a downward sloping

Table 3. Theoretical vs Experimental Young's Modulus (FT8)

Remarks	Theoretical (GPa)	Decrease (%)	Experimental (GPa)	Decrease (%)
Before Damage	53.9	-	49.0	-
90° Ply Failure	51.5	4.4	46.4	5.3
-45° Ply Failure	44.0	18.4	43.5	11.2



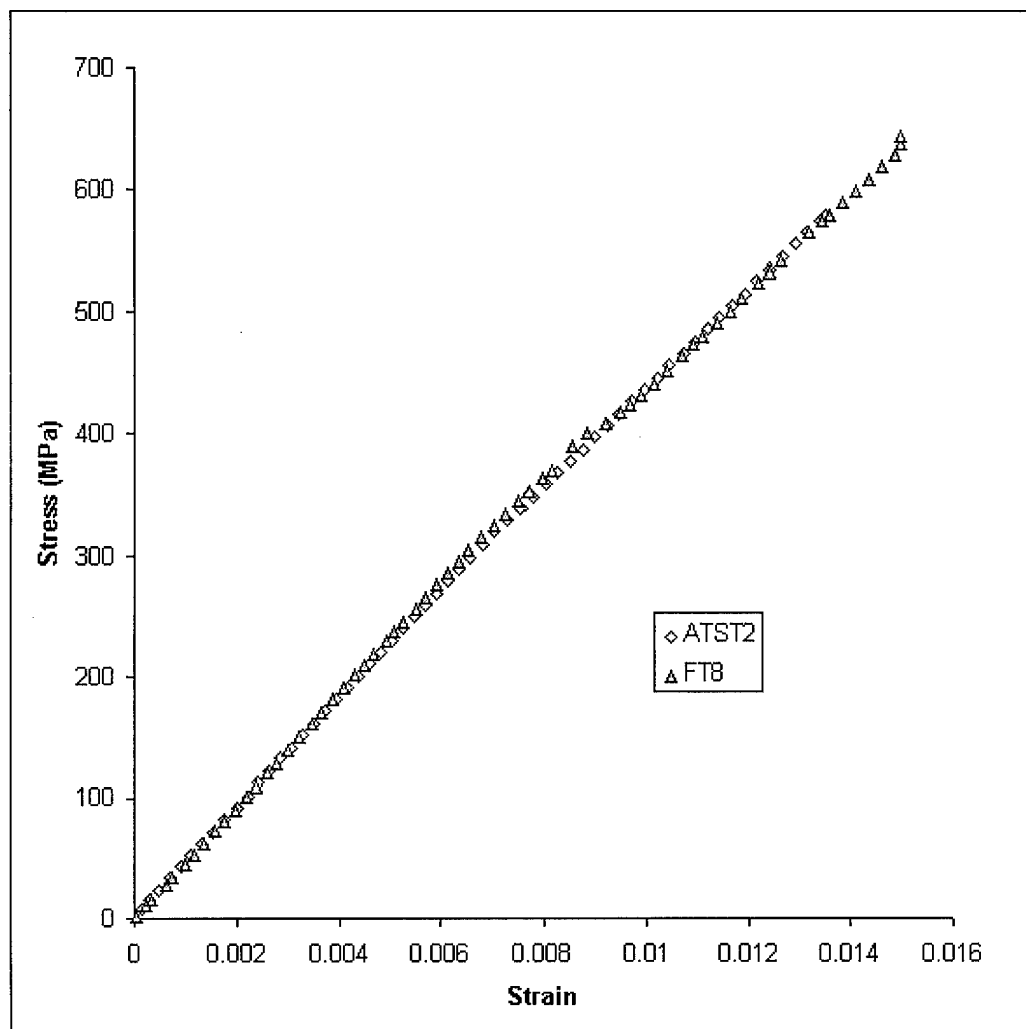


Figure 13. Stress-Strain Curve for Specimens FT8 and ATST2

modulus after the damage. Two explanations may be given for this unexpected behavior. First, the extensometer measured strain over a 101.6 mm length of the specimen. This measurement would give an average strain across this long section, with the possibility of not capturing any effects seen in local areas. The second, more likely, explanation would be due to the damage at the edges of the specimen. As the edges delaminated and cracked, the knife edges of the extensometer would slip or give inaccurate strain results due to the damage. Figure 14 shows the difference between the extensometer and strain gage data.

#### **4.1.2 Damage Mechanism**

##### **4.1.2.1 Un-Interrupted Loading**

Overall, all monotonically loaded specimens had similar transverse failure planes and limited edge delamination. During each un-interrupted monotonic loading test, the specimens were stressed to fail within 60 seconds after the start of the un-interrupted test, so the damage sequence occurred very rapidly. Figures 15, 16, and 17 show the overall failed FT1 specimen, an enlarged view of the failure across the width, and the edge delamination. In general, these specimens had a lesser amount of delamination damage than found during fatigue testing, but compared very well with each other. As discussed in the stress-strain response section, FPF and subsequent ply failures were approximated by the change in the stress-strain curve's slope.

##### **4.1.2.2 Interrupted Loading**

ATST1 and FT7 specimens were loaded at several intermediate levels to record the stress levels at which initial transverse cracking in the 90° plies,  $\pm 45^\circ$  off-ply cracking, longitudinal/axial cracking, and delamination occurred. In addition, the ATST1 specimen was briefly cycled at 200  $\mu\epsilon$  after each loading level to check the voltage output of the actuator at its design strain limit. The capacitance of the actuator was measured after each loading level was reached

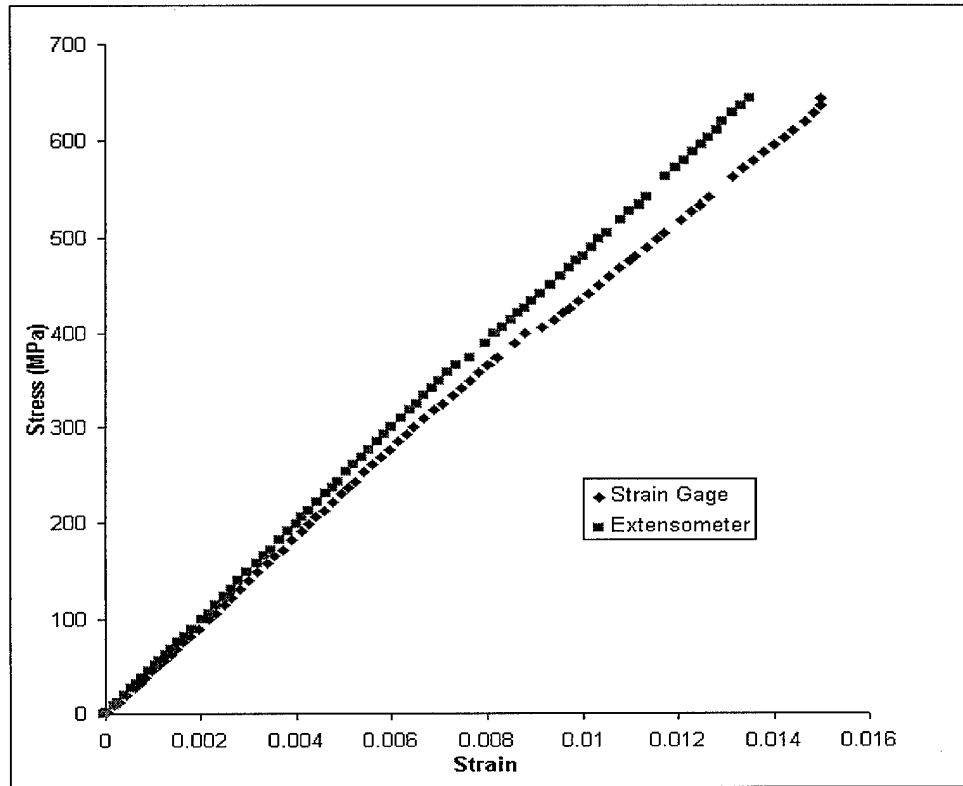


Figure 14. Extensometer vs Strain Gage Data - Specimen FT8

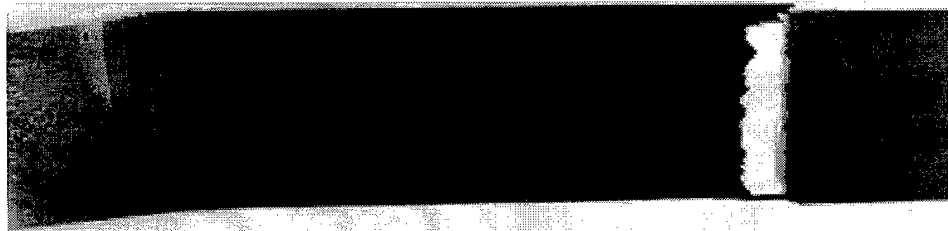


Figure 15. Specimen FT1 at Static Failure



Figure 16. FT1 Static "Flat" Failure Across the Width

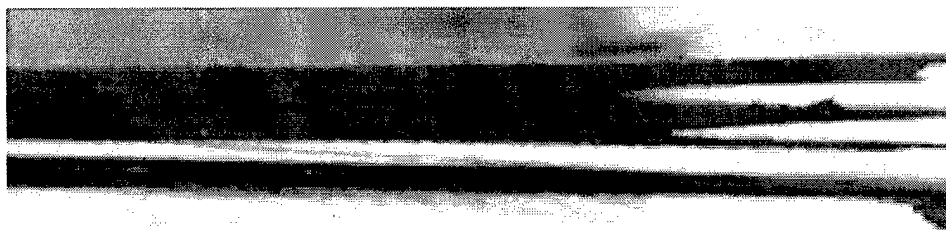


Figure 17. FT1 Edge Delamination at Static Failure

as well. The results of the interrupted testing are discussed in the following subsections. Table 4 summarizes the load levels at which different initial damage modes occurred in the different plies.

#### 4.1.2.3 Initial Transverse Cracks in 90° Plies

The transverse crack initiated, as expected, in the 90° plies because of the weaker matrix and/or matrix fiber interface. The fibers in this case do not prevent the progression of the crack, therefore the crack propagates quickly across the width and ply thickness. Figure 18 shows a typical edge view of an early transverse crack in the 90° plies.

The differences in stress levels at which transverse cracking started between specimens ATST1 and FT7 could be easily attributed to variation of material inclusions or microcracks during the lay-up process. Specimens ATST1 and FT7 started transverse cracking at 200 MPa and 250 MPa respectively. Micromechanically, voids or stress concentrations in the matrix are normally the points of initiation of the cracking. As individual cracks (usually around the fiber/matrix interface) coalesce, the crack goes across the entire width of the specimen, resulting in the transverse crack. If the two specimens were assumed identical with the exception of the embedded actuator, the differences in transverse cracking levels would be due to the localized stress concentrations around the embedded actuator of ATST1. Even though the epoxy completely fills the gaps around the PZT during the cure cycle, the sharp edges and corners of the PZT should be a point of crack initiation. However, in the case of ATST1, the first transverse crack was seen about an inch below the top edge of the actuator. This was the case in most of

Table 4. Stress Levels at Which Initial Damage Occured

Specimen	90° Crack (MPa)	±45° Crack (MPa)	Axial Crack (MPa)	Delamination (MPa)
FT7	250	300	350	350
ATST1	200*	250	300	350
*Initial degradation of voltage output of PZT				

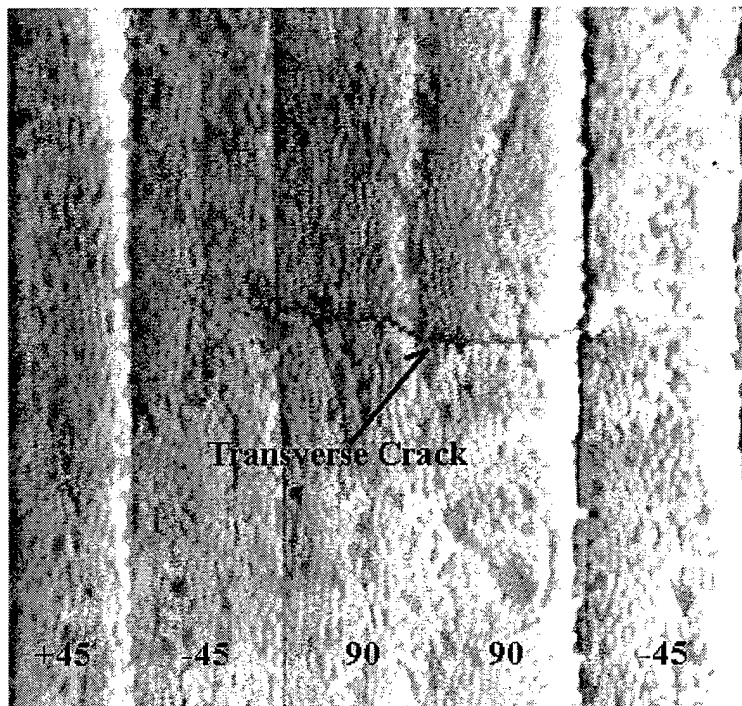


Figure 18. Transverse Cracking of 90° Plies - Specimen ATST1

the specimens with PZT. Therefore, the difference in stress level at which cracking started was likely due to the specimen to specimen variation, instead of due to the presence of the PZT.

One laminate failure criteria related to transverse cracking is FPF. During the interrupted and un-interrupted tests, the transverse crack density of the  $90^\circ$  plies eventually became saturated and resulted in FPF. Once again, any slight variations in FPF between specimens were likely due to the natural variation between specimens due to contaminates, voids, etc. The FPFs for ATST1 and FT7 specimens were approximately at 300 MPa, while the FPFs for ATST2 and FT8 specimens (un-interrupted test) were approximately at 320 MPa. Therefore, both groups of experimental FPFs were close to the expected value of 300 MPa, which was based upon an average experimental modulus of 50 MPa and an ultimate strain of 0.006 mm/mm taken from previous research by Kim [12]. However, there is less confidence in the un-interrupted FPF measurement, since the change in slope was not sharp and other factors such as  $45^\circ$  ply cracking could have caused the shift. Therefore, more confidence is placed upon ATST1 and FT7 values for FPF, which were equal to the expected value of 300 MPa. If the modulus and the ultimate strain were both taken from previous research, the expected FPF would have been 323 MPa, which is also close to the experimental results. Appendix A gives a summary of material properties and equations used in calculating the laminate modulus  $\bar{E}_x$  for a quasi-isotropic, symmetric, homogeneous lay-up.

#### 4.1.2.4 $[\pm 45]$ Cracking, Longitudinal Cracking, and Delamination

The general trend of specimen ATST1 cracking at a slightly lower stress level than specimen FT7 continued until delamination, where the stress levels were identical (See Table 4 on page 50). Neglecting this slight variation in stress levels, the progression of damage was generally the same for all specimens. At approximately the same stress level as FPF, the inner side of the  $-45^\circ$  plies (adjacent to  $90^\circ$ ) started to crack, but not to the extent as seen in the  $90^\circ$  plies.

As stated earlier, this may have been the cause of the shift in the stress-strain slope seen in the un-interrupted tests. Theoretically, after the  $90^\circ$  plies cracked, a resulting stress concentration at the ply interface arose near the crack. Therefore, the adjacent  $-45^\circ$  plies are expected to crack next [16]. In this case however, the crack was not typically horizontal across the thickness, but tended to rise up at an approximate  $45^\circ$  angle in many cases. Figure 19 shows the start of a typical crack in the  $-45^\circ$  ply. The growth of this crack may be explained by the angle of the ply. In this case, the matrix interface again is the weak link, failing first due to the ultimate strain level being reached in this ply. The crack propagates upwards or downwards due to the fibers, which cause the crack to proceed along the path of least resistance.

After the  $90^\circ$  and  $-45^\circ$  plies had cracked, longitudinal cracking and delamination occurred mainly between  $90^\circ$  and  $-45^\circ$  plies. Longitudinal cracking at the ply interfaces vertically joined the transverse cracking that had already occurred. Figure 20 shows the longitudinal cracking at 350 MPa in FT7 as the stress was increased by another 50 MPa, where delamination of the plies occurred completely down the length of the edge of the specimen.

Overall, the sequence of damage in the composites seen in the present study agreed with previous investigations on the damage mechanisms of  $[0 | \pm 45 | 90]_S$  quasi-isotropic laminates. First, the  $90^\circ$  plies transversely cracked and slightly decreased the modulus. Resulting stress concentrations near the cracks resulted in further cracking near this area as the load was increased even more. Longitudinal cracking and delamination then occurred as the edge effects caused the plies to pull apart at the edge. The edge effects were from two primary sources. First, as the specimen was pulled in tension, Poisson's effect resulted (contraction of the width). The outside  $0^\circ$  plies contracted along the width easier than the  $90^\circ$  plies, primarily because of the direction of the fibers in each ply. The resulting edge effect was a normal stress at the edge. The normal stress equalized the shear stress moment created by the "pushing" and "pulling"



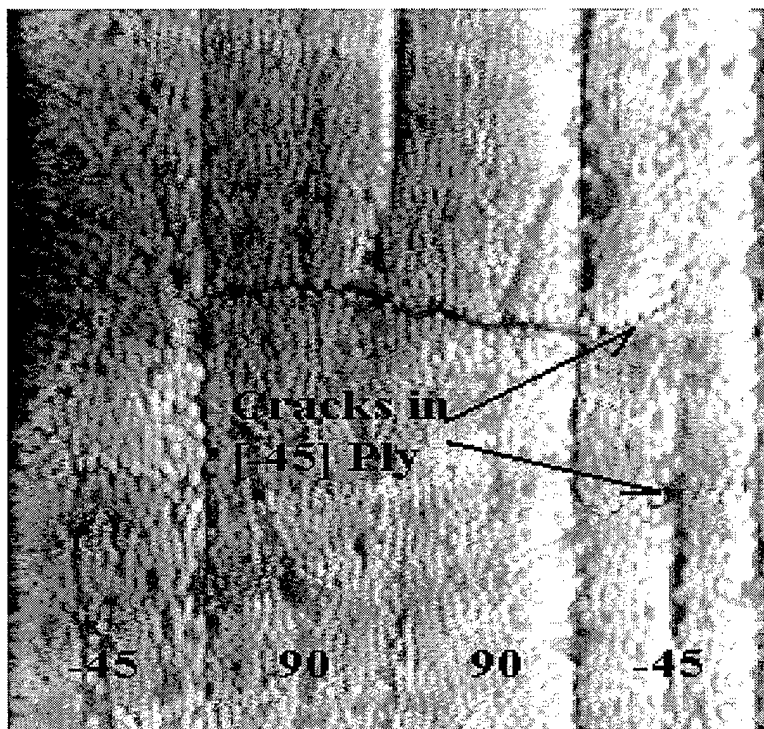


Figure 19. Crack in  $-45^\circ$  Ply - Specimen ATST1

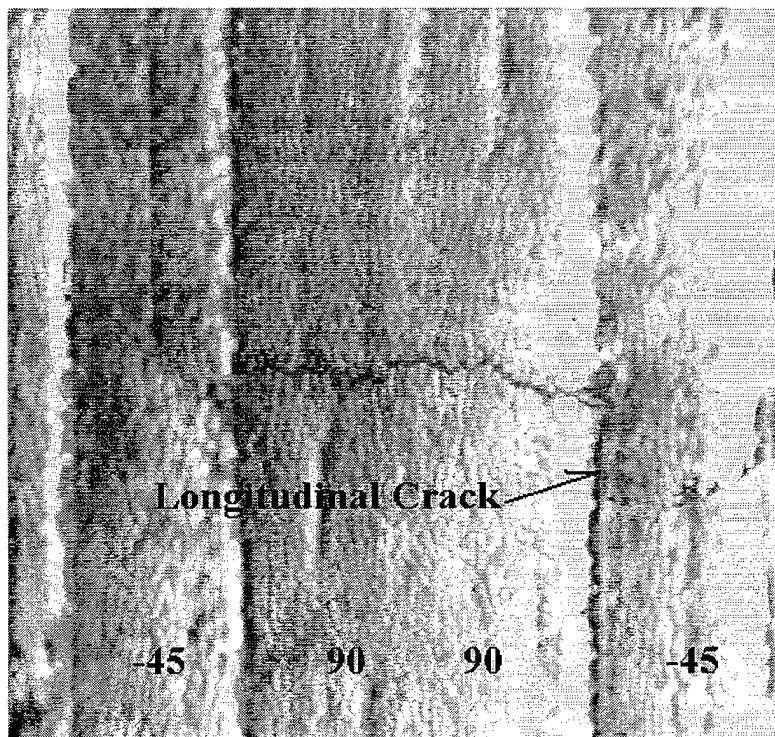


Figure 20. Longitudinal Cracking Between 90° and -45° Plies (FT7)

of the different plies. In this case the normal force was in tension, resulting in delamination. The lesser, second edge effect was due to the  $\pm 45^\circ$  plies, which have a tendency to straighten in the  $0^\circ$  direction when pulled in tension. The resulting shear stresses at the ply interface may have resulted in increasing the delamination damage. Delamination and cracking occurred primarily in the  $90^\circ$  and  $-45^\circ$  plies, which decreased the modulus of the composite even further, which was evident in the stress-strain response curve. Eventually, the ultimate strength of the composite was reached, where the damage of the fibers of the  $0^\circ$  plies resulted in fracture.

In summary, specimens with and without sensors had very similar cumulative mechanical damage sequences, and the stress levels of different ply failures did not vary between them. Observed differences are certainly within expected variances due to material inhomogeneities, test differences, etc. One trend seen was a slightly lower stress level for crack initiation in specimen ATST1, which could be due to the residual stresses from the embedded sensor.

#### **4.1.3 Degradation of PZT Output**

During the interrupted testing of ATST1, the voltage output of the embedded PZT was monitored at two strain levels ( $\sim 200$  and  $1000 \mu\epsilon$ ), which corresponded to approximately  $10 \text{ MPa}$  and  $50 \text{ MPa}$  stress levels. In this case, after a certain intermediate static stress level was reached in the test, the load was then brought back down to zero. At this point the specimen was cycled in tension-tension,  $R = 0.1$ , at  $10 \text{ MPa}$  and  $50 \text{ MPa}$ . The “ $R$ ” ratio of the lower load to the peak load was kept at  $0.1$  for all fatigue type testing. Also at this time, the capacitance was checked to verify the electrical integrity of the PZT.

Results showed the voltage output of the PZT remained fairly constant until a static load of  $100 \text{ MPa}$ , but as  $150 \text{ MPa}$  was reached, the voltage output dropped by  $20 \%$ . When  $200 \text{ MPa}$  was reached, the output dropped by over  $50 \%$ , followed by further degradation as higher static loads were applied (Figure 21).  $200 \text{ MPa}$  corresponded to the initial cracking of the  $90^\circ$

plies, therefore the drop seemed to be associated with either laminate damage, sensor damage, or both. Figure 21 shows the drop-off of the voltage at both the 10 *MPa* and 50 *MPa* cycling after the corresponding static load was applied.

All capacitance measurements were taken at zero stress levels after the interrupted static test was performed. Capacitance measurements steadily increased after the intermediate level of 100 *MPa* and peaked at 300 *MPa* (See Figure 22). These slight increases in capacitance may have been due to the changes in thickness and other material properties of the PZT, but generally are not fully understood. After reaching the upper limit, the capacitance started to drop under higher loads, which may have been the result of PZT cracking.

Theoretically, changes in plate capacitance due to dimension and material constant changes can be approximated by Equation 2, which is duplicated in Equation 14 for convenience.  $K_3^T$  is the dielectric constant,  $\epsilon_0$  is the permittivity of free space,  $l$  is the length,  $w$  is the width, and  $t$  is the thickness of the capacitor.

$$\text{Plate Capacitance (F)} = \frac{K_3^T * \epsilon_0 * l * w}{t} \quad (14)$$

To determine which variable was the primary factor in the capacitance change, an analysis of the potential changes in dimensions and material constants was done. If the PZT dimensions were permanently changed by the intermediate static loads, and  $K_3^T * \epsilon_0$  remained constant, the theoretical plate capacitance would have gradually increased as the thickness decreased. Using Poisson's ratio to determine the maximum potential change of the PZT's dimensions and Equation 14, the maximum increase in capacitance was calculated. Figure 23 shows that this mathematical rate was found to be lower than what was seen experimentally. This would indicate that the other variables in Equation 14 changed, or other factors were involved. By

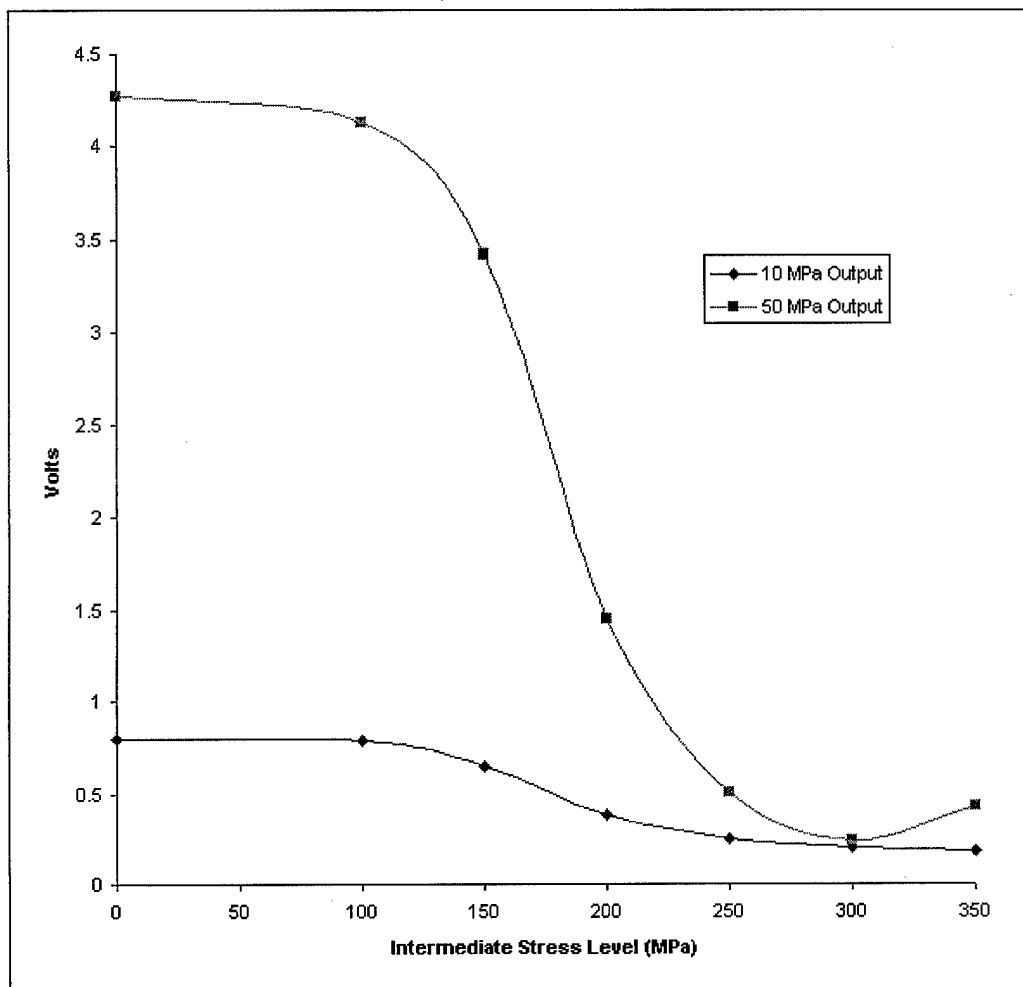


Figure 21. Degradation of PZT Output after Intermediate Static Loads (ATST1)

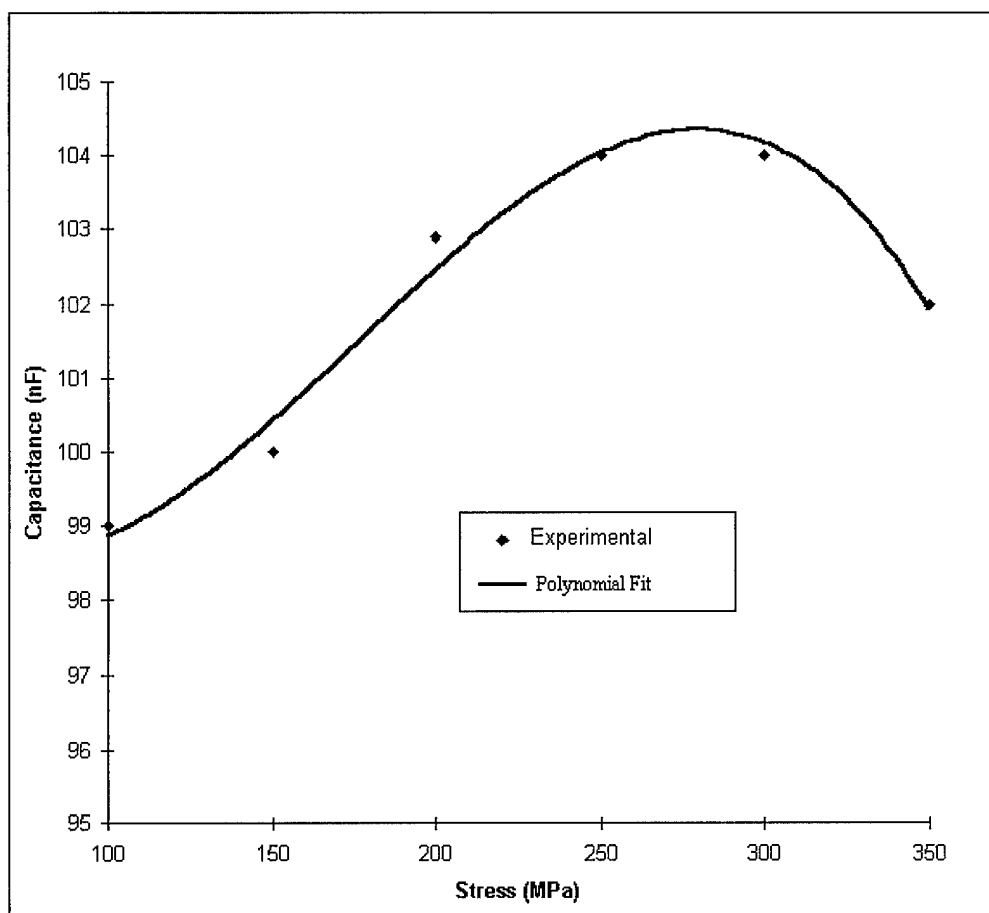


Figure 22. Capacitance vs Applied Stress - Specimen ATST1

linearly increasing the dielectric constant, the experimental rise in capacitance can be matched initially (Figure 23). The equations and assumptions for the mathematical data are shown in Appendix C.

In order to further understand the PZT output degradation due to mechanical cycling, low-strain, high cycle fatigue testing was conducted. This test is discussed in the last section of this chapter. Rises in capacitance were noticed in this case as well, but were not seen for all the tests. This is understandable, since the lower stress levels would cause less permanent deformation of the PZT. Further details are given at the end of this chapter.

## **4.2 Fatigue Test Results**

The primary objective of the fatigue tests was to determine the effects of mechanical fatigue loading on a quasi-isotropic laminate with embedded piezoelectric sensors. The fatigue test results are divided into a discussion of the S-N curve, damage mechanism, and PZT output degradation during and after cyclic loading. Basically, the S-N curve is a graphic illustration of stress level versus life given in Table 5 on page 63, where the specimens were loaded under different stress levels and failed or did not fail after a certain number of cycles. In general, flatter S-N curves indicate the laminate is fiber dominated, whereas matrix dominated laminates would have a more noticeable drop-off. The results of the S-N curve unexpectedly indicated that the AT specimens (with PZTs) had a fatigue strength comparable, if not better, than the FT specimens (without the embedded PZT). Investigation of the damage mechanism showed that the sequence of damage was found to be very similar to the monotonically loaded specimens, except that the extent of damage due to fatigue was much larger. The cyclic voltage output of the PZT and capacitance were again monitored throughout the lifetime of the specimen. The voltage output of the PZT generally degraded substantially after only a few cycles, since transverse cracking

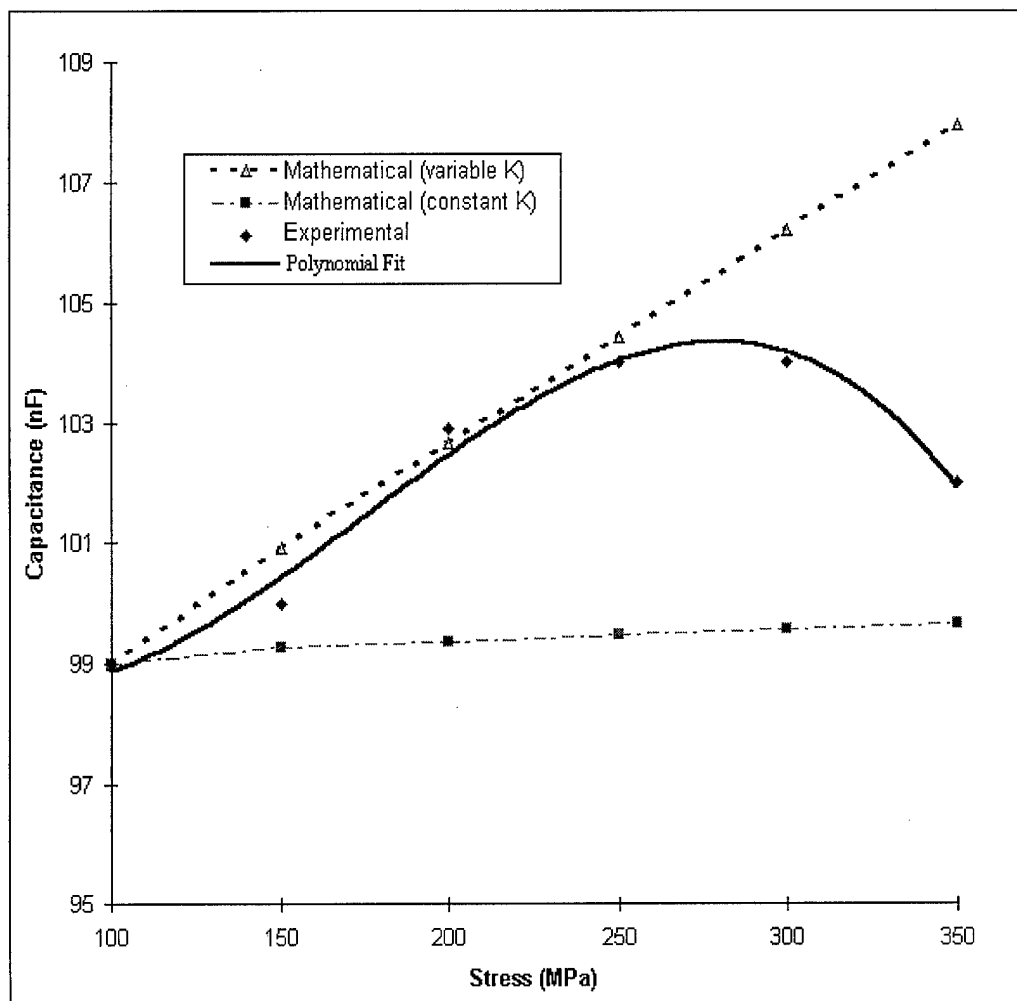


Figure 23. Mathematical vs Experimental Changes in Capacitance



of the 90° plies was almost immediate at the fatigue loads used in this study. A brief discussion on the degradation of the PZT follows after the fatigue test results.

#### 4.2.1 S-N Curve

A good S-N curve should contain the data point at each decade of fatigue life [15], i.e.  $10^3$ ,  $10^4$ ,  $10^5$ , etc. With this objective, the initial test was conducted at 360 MPa. This initial test of FT2 was stopped at 1.2 million cycles, since the modulus was decreasing very slowly and the life expectancy was suspected to be very large. The next two test specimens, FT3 and AT1 (380 MPa), were run concurrently for 5 million cycles. Due to time constraints, these tests were halted before the failure of these specimens, even though they showed very substantial damage. Specimen FT6 was not tested to failure either, since this specimen was used primarily to detect the delamination depth during the cycling. The extent of the delamination was initially approximated by measurement of the bending of the ply at the surface. In order to compare this visual inspection with the actual delamination depth, FT6 was ultrasonically tested at the same intervals as that visual inspection. These results are discussed later in the depth of delamination sub-section. Due to the long time frame and potential degradation due to water absorption during the ultrasonic testing, visual inspection was done for the remaining specimens. The HP specimens were 2.54 cm wide without PZTs, which were tested to ensure that width effects were not causing any effect on the fatigue life. Table 5 and Figures 24 and 25 show the specimens tested, the level of stress applied, and the cycles to failure.

As mentioned earlier, the trend indicated the AT specimens (with PZTs) have a fatigue life comparable, if not better, than the FT and HP specimens (without PZTs). All the AT specimens survived approximately the same number of cycles or more than the FT and HP specimens at the same stress levels. One explanation may be due to the location of the PZT and damage mechanism differences of the specimens, which will be discussed later in this chapter. Another

Table 5. Summary of Fatigue Tested Specimens

Remark	Specimen	Fatigue Stress (MPa)	Cycles to Failure
	FT3	380	+5 million
	FT4	420	753,600
Without PZT	FT5	440	12,500
	HP1*	420	496,000
	HP2*	440	18,500
With PZT	AT1	380	+5 million
	AT2	420	1.01 million
	AT3	440	1.39 million
	AT4	460	87,000
"+" indicates that specimen did not fail, stopped due to time constraints.			
* These specimens were 25.4 mm in width			

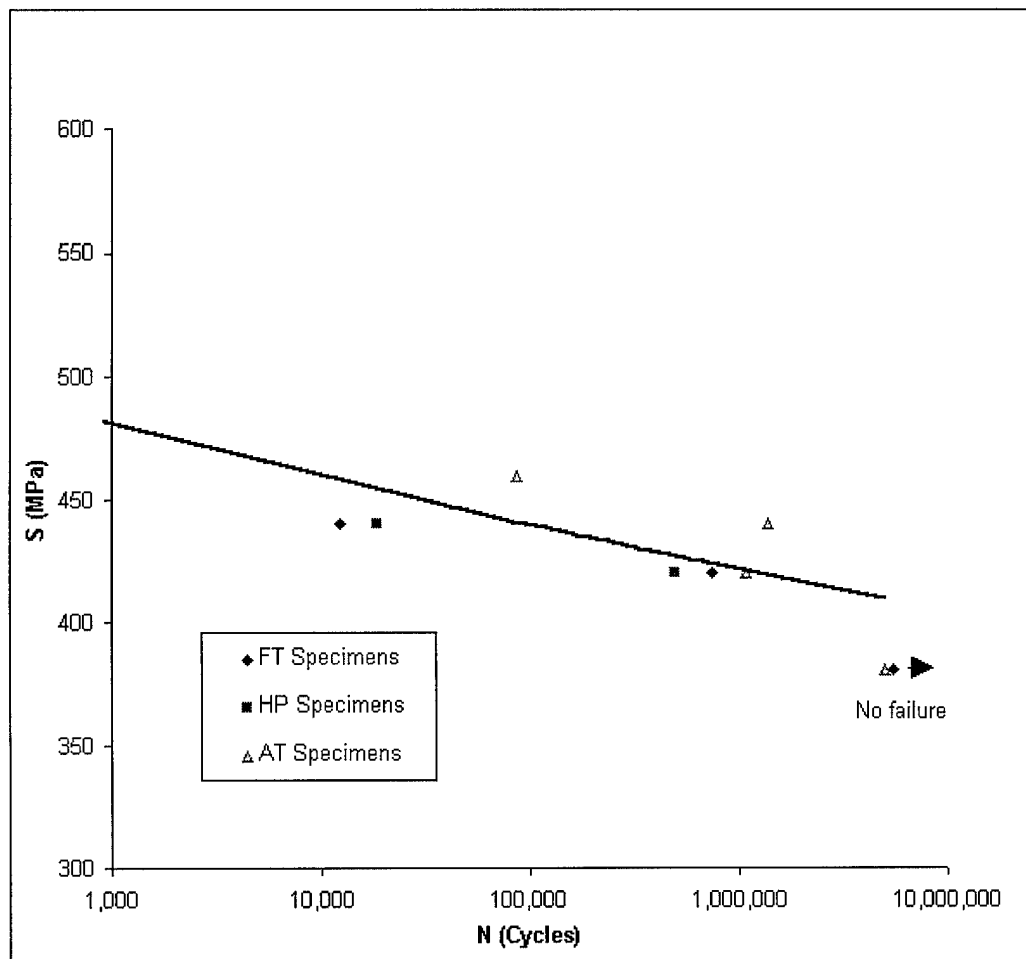


Figure 24. S-N Curve

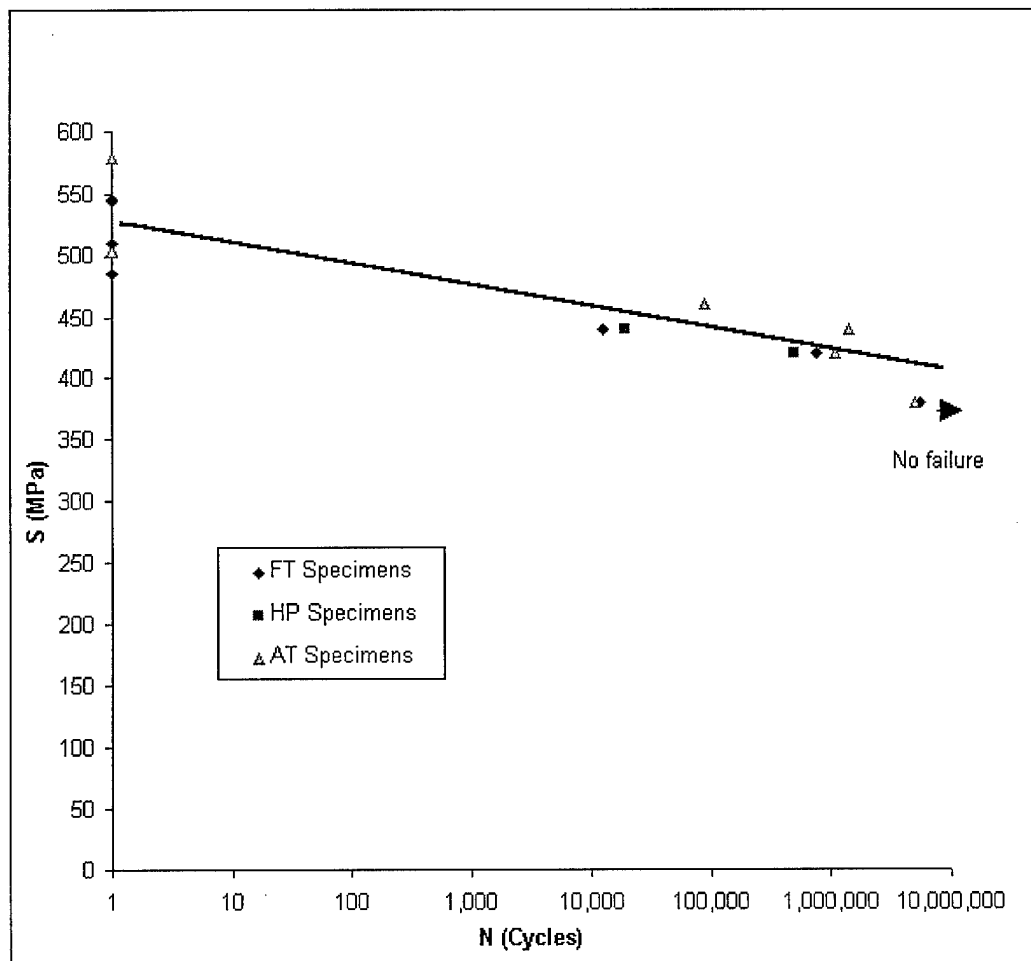


Figure 25. S-N Curve on Larger Scale

explanation would be the statistical variation, where stronger than average AT specimens were tested by chance. Overall, the differences were not very significant, since the data generally fell on the same S-N curve, as shown in Figure 25. Any width effects on the fatigue life (HP versus FT specimens) were not found.

One drawback of this laminate lay-up is the variation in results. The S-N curve for both AT and FT specimens were rather flat. Therefore slight changes in stress levels resulted in large differences in cycles. The flatness of the curve was expected, since the tested carbon-epoxy laminate has a fiber dominated strength [12]. Minor differences in strength could result in large differences in fatigue life. Five specimens without PZTs and four specimens with PZTs were used to establish the S-N curve. Nominally, a few data points per logarithmic interval would be desired, but the time and number of specimens were limited. As a result, the S-N curve only shows the general trend in the cycles to failure.

## **4.2.2 Damage Mechanism**

### **4.2.2.1 Failure Surfaces**

The damage mechanism for both types of fatigue specimens (AT and FT) was similar to the monotonically loaded specimens, but the extent of overall damage was much more during fatigue. In the monotonic tests, the load was constantly increased to failure, so the progression of damage was dependant on the increasing level of applied stress. In the fatigue tests, the progression of damage was dependant on both the applied stress and the number of cycles. Since the applied fatigue stresses were above the measured static delamination stress level, the different types of damage occurred almost simultaneously, then steadily increased thereafter. First, transverse cracking immediately occurred in the 90° plies. Before 500 cycles was reached for each specimen, the crack density of the 90° plies became saturated, resulting in FPF. The

crack saturation spacing average for the specimens was 1.33 cracks/*mm*. Following the 90° transverse cracks, the adjacent -45° plies cracked due to the interlaminar stress and increasing damage. Significant longitudinal cracking and delamination along the length of the specimen occurred after the application of more cycles, which eventually led to ultimate failure. Figure 26 shows how the delamination moves back and forth in the middle plies down the length of the specimen. This delamination was primarily found between the 90|90 and -45|90 interfaces. The switching of delamination interfaces usually occurred at transverse cracks. As the cycles increased further, the width and depth of the delamination steadily increased. Figures 27, 28, 29 show the width of the delamination for AT2. For high cycle specimens, the delamination width noticeably widened and contracted during the increasing and decreasing portion of the load cycle, flapping so to speak. Figures 30, 31, 32 show the final failure region of FT4. Notice the extensive delamination, debonding, and fiber breakage at this region. Away from this “jagged” failure region, fiber failure was seen at the opposite end of the specimen in the middle. This cracking of the 0° plies is shown in Figure 33.

In some cases, the specimen failed in two locations at about 50.8 *mm* from the grips. Figure 34 shows how FT5 failed in two regions. One area showed extensive fatigue damage, while the other area looked similar to monotonic failed specimens. Bending at failure around the edge was also noticed, where one side would actually show compressive damage. This would suggest the failure started at the edge, where extensive delamination caused a significant reduction in strength in a local region. Near the grips, the normal tensile stress caused by the



Figure 26. Edge Delamination - Specimen FT6

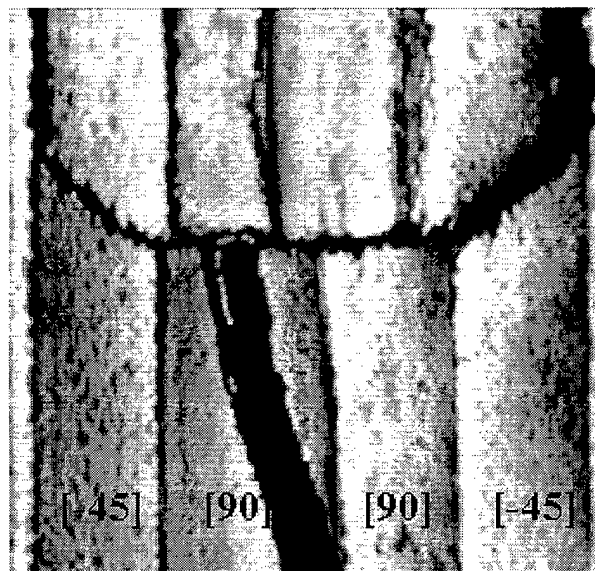


Figure 27. Delamination at Cycle 1k - Specimen AT2

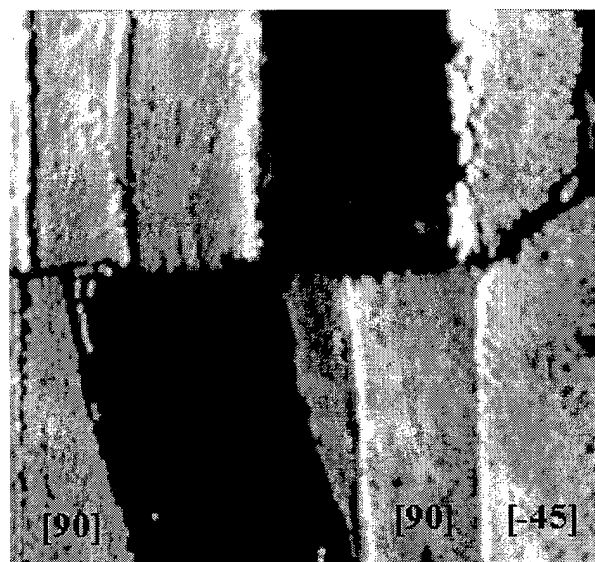


Figure 28. Delamination at Cycle 10k - Specimen AT2

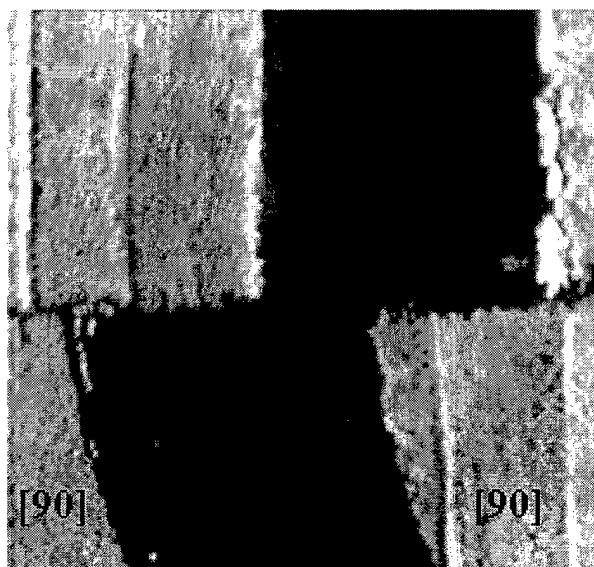


Figure 29. Delamination at Cycle 50k - Specimen AT2

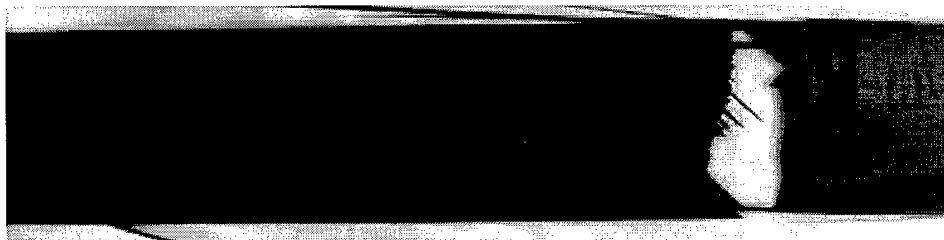


Figure 30. Failed Specimen FT4

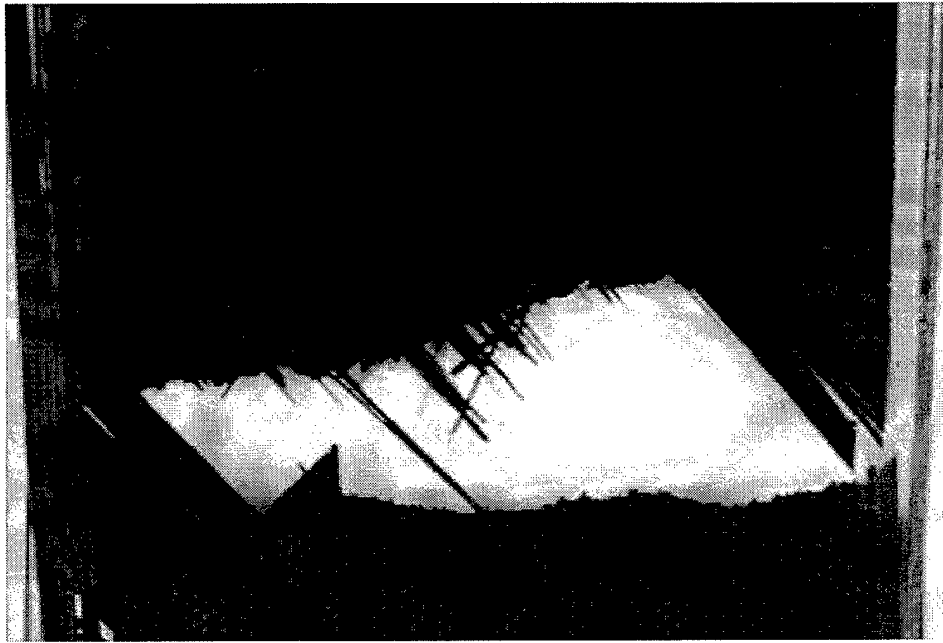


Figure 31. "Jagged" Failure Area - Specimen FT4

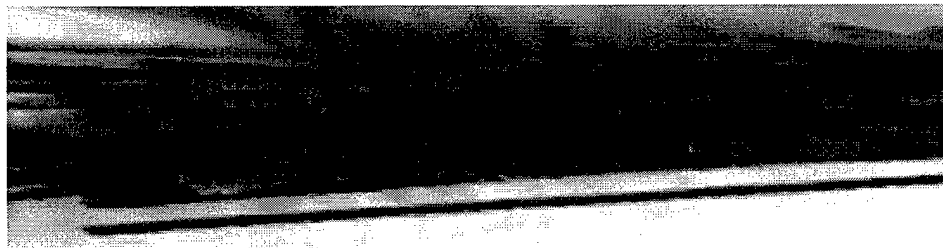


Figure 32. Edge Delamination at "Jagged" Failure Area - Specimen FT4



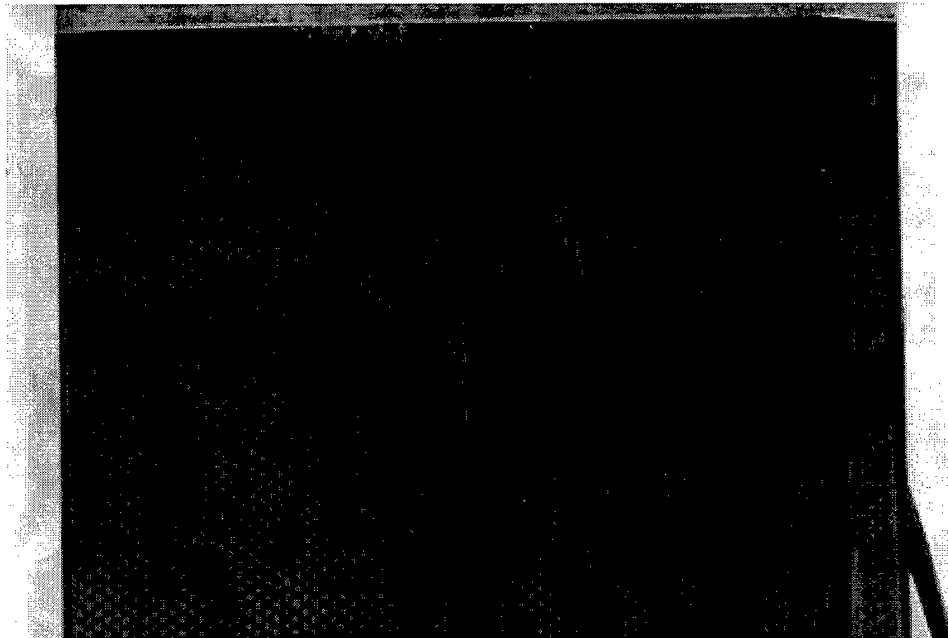


Figure 33. Failed Fibers Away from Ultimate Failure Region - Specimen FT4

edge effects was counteracted by the compressive normal stress of the grips. This area would be subjected to a ripping effect. As the edge started to fail at one end of the specimen, a shear moment resulted causing the opposite end to fail or to be severely damaged as well.

The results of the damage analysis of AT and FT specimens showed similar trends with a couple of significant differences. The most noticeable difference was the ultimate failure mode for two AT specimens. Specimens AT2 and AT3 split apart down the middle, spreading out similar to a fan at ultimate failure load. The embedded PZT was split down the middle as well, indicating the bonding of the interface to the plies was stronger than the interface between the plates of the PZT. Inspection of the split PZT showed extensive cracking in the PZT and lead wire disconnection. Figure 35 shows how specimen AT2 split at ultimate failure. Figure 36 shows the split PZT after this specimen was cut apart, while Figure 37 shows the extensive damage to the lead wire area of the sensor. All the figures show the extensive damage due to fatigue surrounding the PZT. The smoother surfaces around the lead wire section indicate this area was not completely delaminated until near ultimate failure. This agrees with the ultrasound inspection of fatigued specimens, where the delamination progressed into the middle areas last. While FT specimens showed the same trend of delamination, none of these specimens completely split upon failure.

#### **4.2.2.2 *Change in Young's Modulus***

Monitoring of the Young's modulus was another way of showing the progression of damage in the laminate. As seen in the monotonic loading section, the modulus decreased as plies failed and damage increased. Both AT and FT specimens saw immediate drops in their modulus of approximately 5 %, which was similar to the monotonic loading after the FPF. As the damage increased after cycling, the modulus eventually dropped off by more than 15 % in most cases, which may indicate  $-45^\circ$  failure or extensive delamination damage. Many cycles and substantial

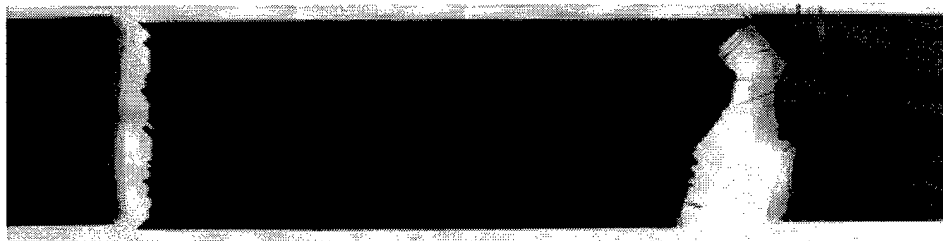


Figure 34. Failed Specimen FT5



Figure 35. Failed Specimen AT2

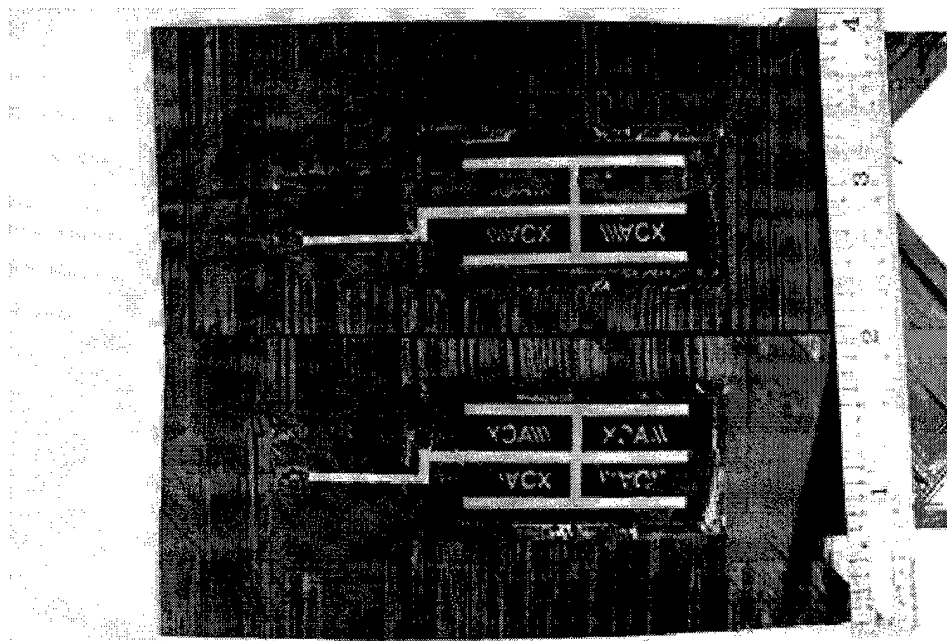


Figure 36. Split PZT of Specimen AT2



Figure 37. Lead Wires of Specimen AT2

damage were required for the specimens loaded at lower stress levels to fail, since the modulus had to decrease until fiber breakage or localized failure at the edges occurred. Theoretically, delamination at the edges results in more stress on the  $0^\circ$  plies at the edge, since the interfacial load transfer mechanism has been broken. In static loading, the increasing stress levels caused the ultimate strain of the fibers to be reached more quickly, while the fatigue loading required progressive damage to occur before the  $0^\circ$  plies failed.

AT and FT specimens both saw degradation in the modulus, but trends in progression were somewhat different. The modulus for FT specimens degraded linearly on the logarithmic scale. Figure 38 shows how all the FT specimens follow approximately the same slope of the normalized modulus versus cycles curve. This indicates the relative drop in each specimen's modulus occurred at about the same rate, when compared directly to cycles. This was slightly different than expected, since higher loaded specimens should have a higher rate of fatigue damage [21]. Specimens under higher loads failed in less cycles, since the higher stress was sufficient to break the specimen at this point. Specimens at lower load required more fatigue damage before ultimate failure occurred. It should be noted that since FT6 spent a large amount of time in the water (for ultrasonic tests), the data from this specimen was not used for degradation of stiffness results.

When the normalized modulus is compared with the normalized cycles to failure, stiffness reduction trends are more noticeable. Figure 39 clearly shows the different extent of stiffness reduction for each specimen. Specimen FT5 was tested at the highest load and failed after only 12,000 cycles. Obviously, there was no substantial fatigue damage before the ultimate strength of the laminate was reached. FT4's curve was slightly above FT3's curve, which indicates less fatigue damage for higher loads again. The higher stress level was sufficient to fail the specimen at an earlier point in fatigue cycling.

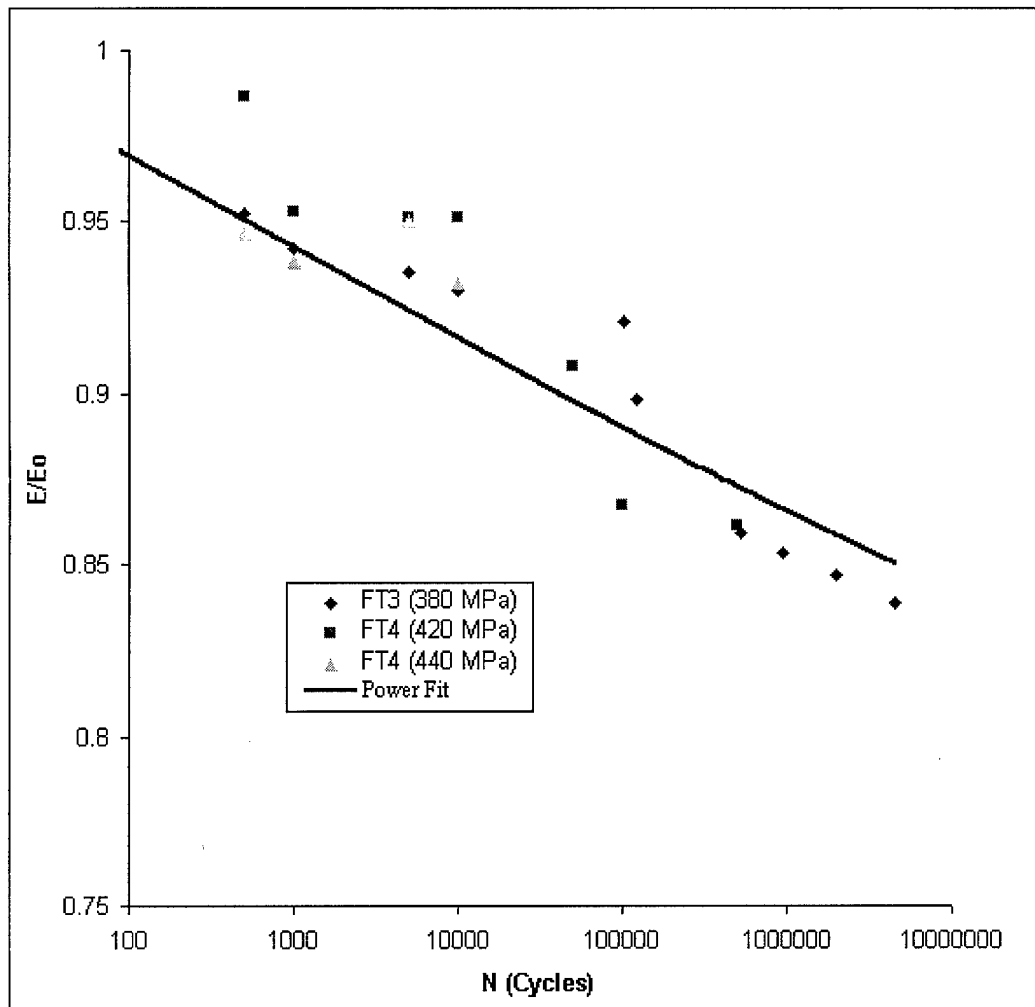


Figure 38. Normalized Modulus vs Cycles - FT Specimens

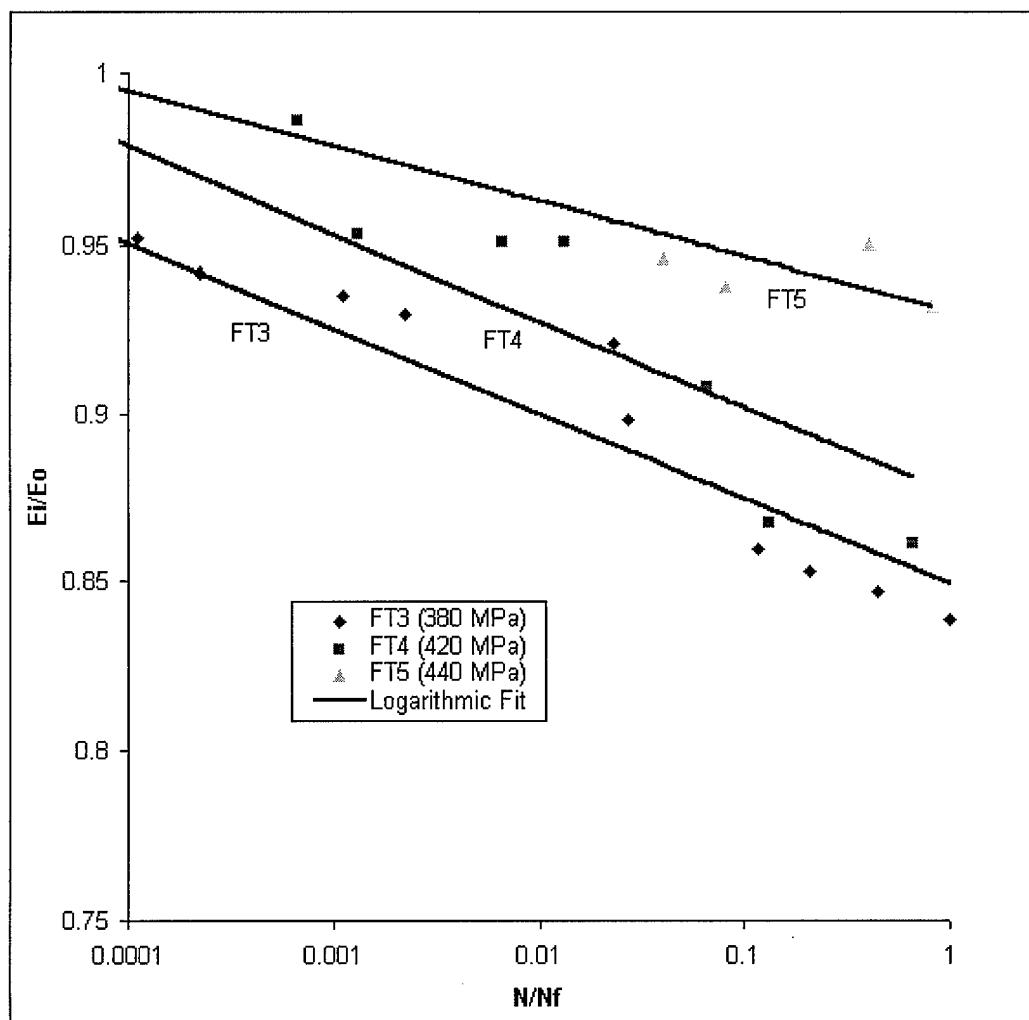


Figure 39. Normalized Modulus vs Normalized Cycles - FT Specimens



The modulus for the AT specimens showed the drop off more sharply at the later part of fatigue life. Further it showed that rate of fatigue damage was more sensitive to stress levels. Figure 40 shows the upper and lower curves of AT1 and AT4 surrounding the data points of AT2 and AT3. The dependency of the rate of stiffness reduction on the level of stress (not seen in the FT specimens) was expected [21]. In this case, the reduction in modulus started in the same manner as seen in FT specimens, but then dropped off at a higher rate.

The highest loaded specimen, AT4, saw the greatest drop in modulus, which was not expected. The lowest loaded specimen, AT1, which was cycled for over 5 million cycles, did have a considerable reduction. The overall comparison indicated that similar degrees of modulus reduction were required in each specimen before ultimate failure occurred. This can be more clearly shown in Figure 41, which shows the extent of damage of each of the AT specimens versus the normalized cycles to failure. This could be attributed to the delamination across the width of the specimen, where the PZT split into two parts in a couple of cases. When this point of damage would occur, the laminate would fail.

Another explanation of the slightly varying results between the different specimens could be extensometer slippage at the edges. In order to prevent this variation due to edge damage, the extensometer was remounted at each inspection interval. The modulus was then measured at 80 MPa, therefore the extensometer should not have been greatly affected by any slippage normally seen at higher load levels. (The monotonic stress-strain curve showed the extensometer data was skewed only at a level greater than 300 MPa.) However, some variation in extensometer interfaces could still have attributed for the differences seen.

When looking on a larger scale, the overall range in data for FT and AT specimens were usually within 5-15 % of each other. While some trends may have been attributed to the embedded sensor and extensometer, the natural variation in each specimen's material properties may

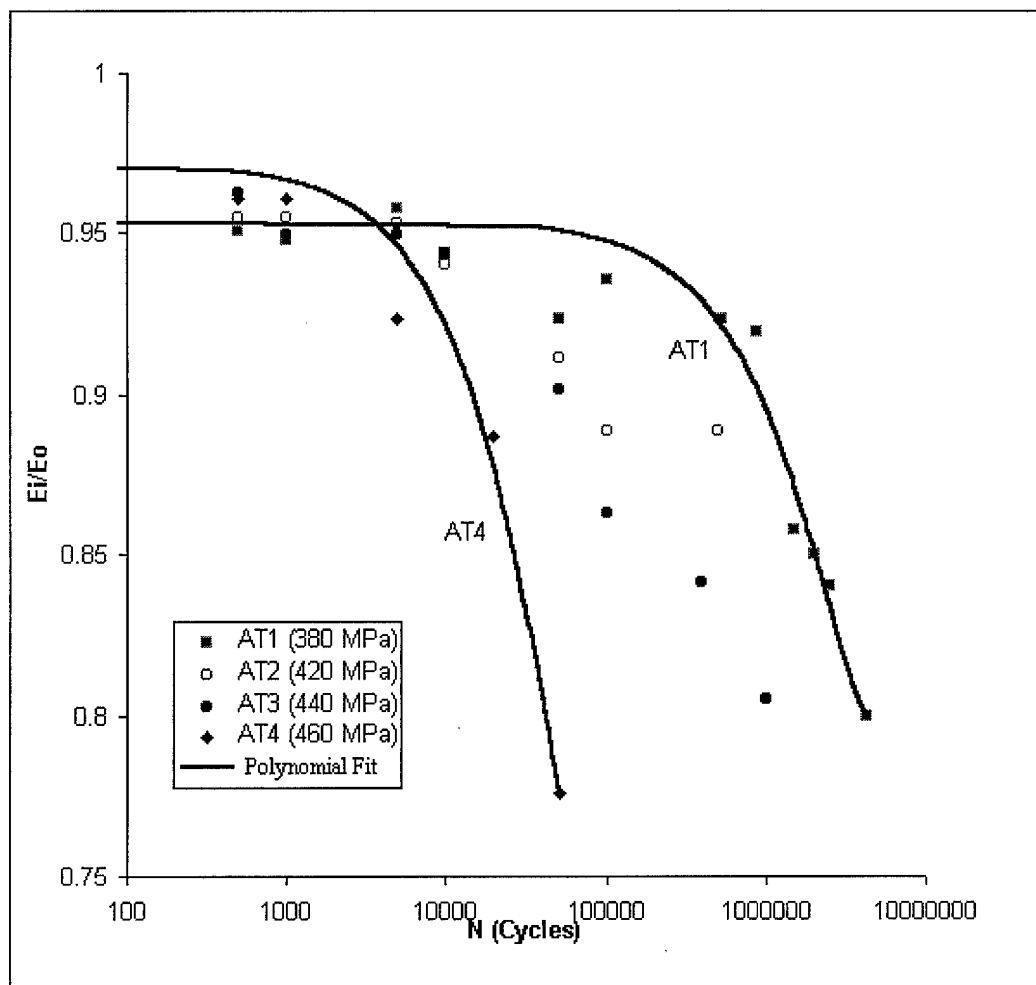


Figure 40. AT Specimens Normalized Modulus vs Cycles

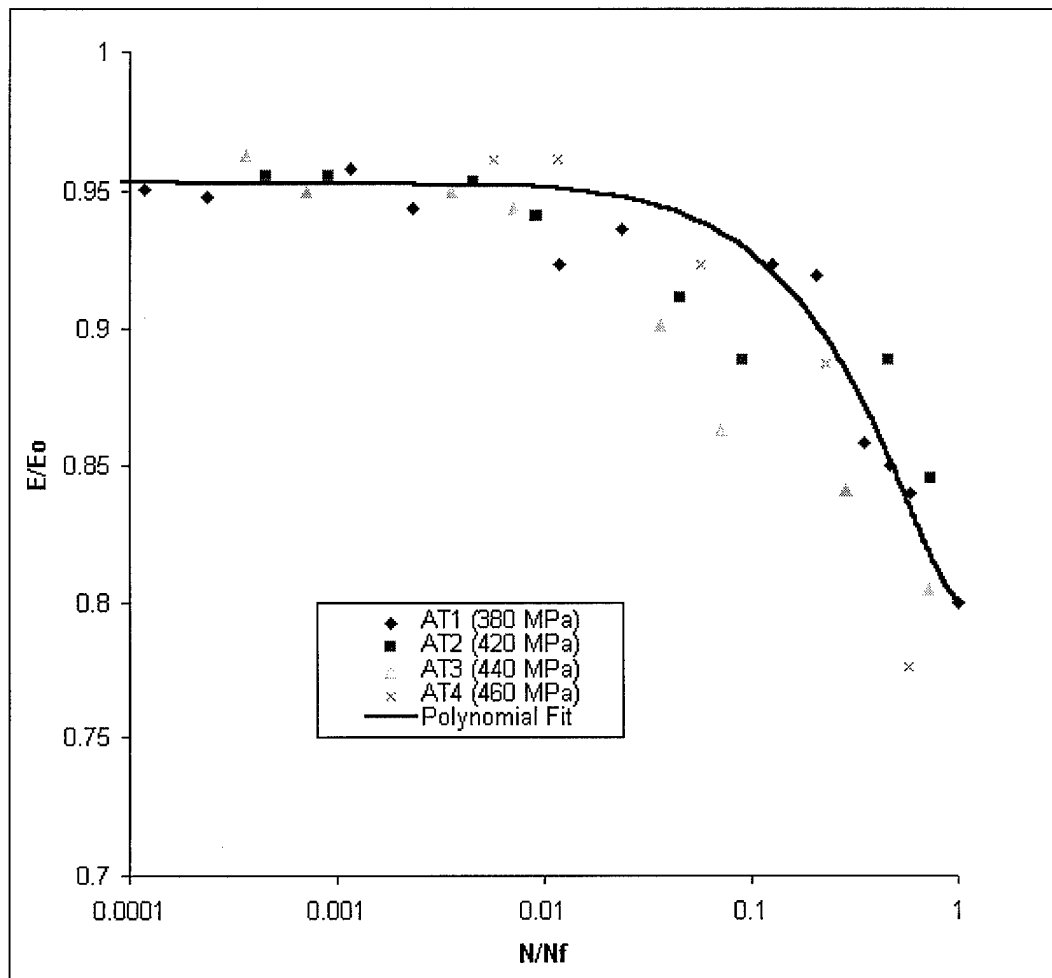


Figure 41. AT Specimens Normalized Modulus vs Normalized Cycles

have caused many of the differences as well. When all the data is plotted on the same normalized cycles curve, most specimens fall within the same scatter band, as seen in Figure 42. More specimens would have to be tested to ensure a statistically accurate analysis.

#### **4.2.2.3 Depth of Delamination**

Depth of delamination was measured to track the progression of edge effects in both AT and FT specimens. The maximum depth of delamination was measured on one edge, however some ultrasound tests were also conducted to verify the overall extent of delamination. Specimen FT6 was used to compare measurement methods of depth of delamination, which were external surface inspection and ultrasound technique. As shown in Figure 43, the external surface inspection gives a relatively accurate approximation of the depth of delamination. Since specimen FT6 spent a large amount of time in the water, this data was not used for the overall depth of delamination results.

The depth of delamination trends found in the FT specimens were generally as expected. Tensile fatigue loading of this quasi-isotropic laminate has been shown to result in delamination due to edge effects [12, 21]. As the fatigue loading was increased, the normal stresses due to Poisson's effect and shear stresses of the 45° plies increased as well. Therefore, higher applied stresses should result in a larger rate of delamination at the edge. Figure 44 shows the increasing delamination of FT specimens versus the applied stress. The higher applied stresses resulted in a higher rate of delamination, but an overall lower total depth of delamination at failure. As similarly seen in the degradation of stiffness, the extent of damage had to increase until the stress level could fail the specimen.

The AT specimens showed similar results, but with a slightly different progression rate with cycling. The rate of delamination growth found in AT specimens was more gradual. AT1 actually plateaued for many cycles before rapidly rising at high cycles. It should be noted that

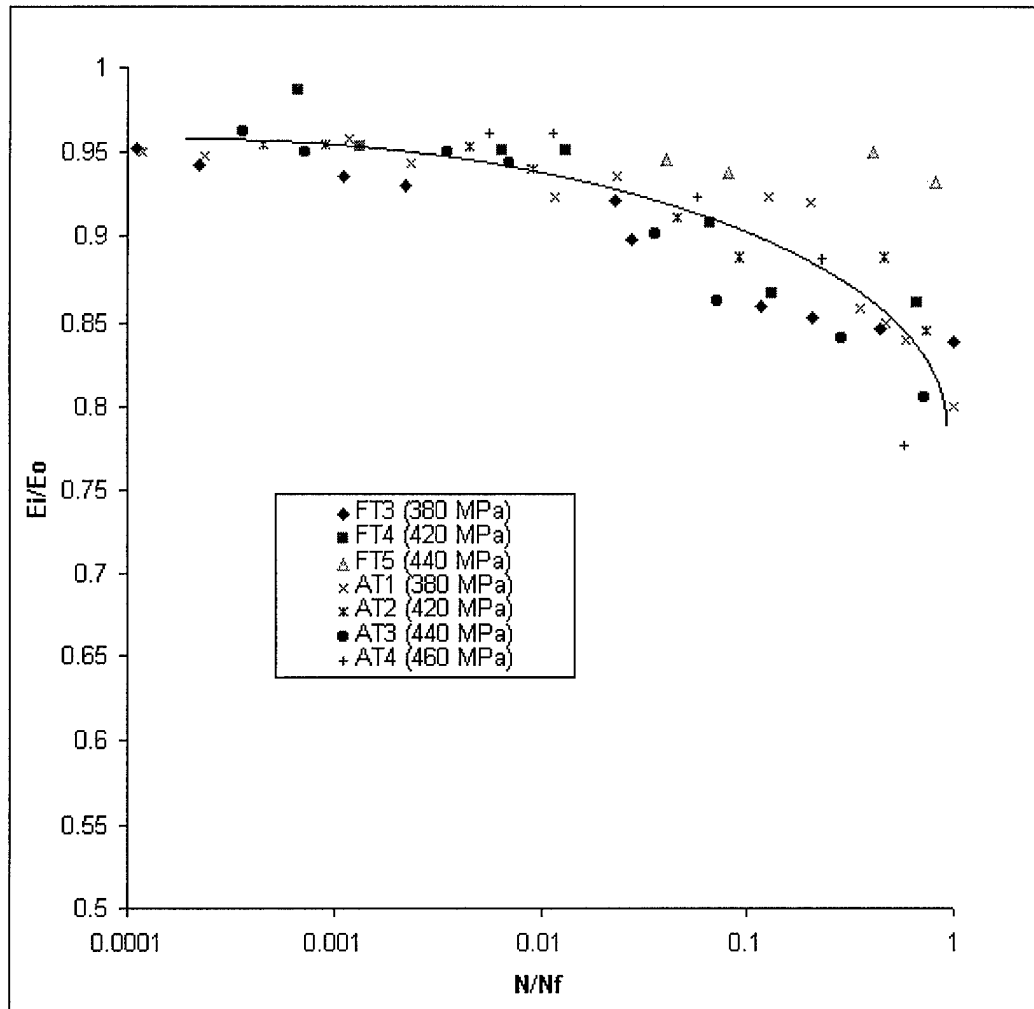


Figure 42. Normalized Modulus vs Normalized Cycles on Larger Scale

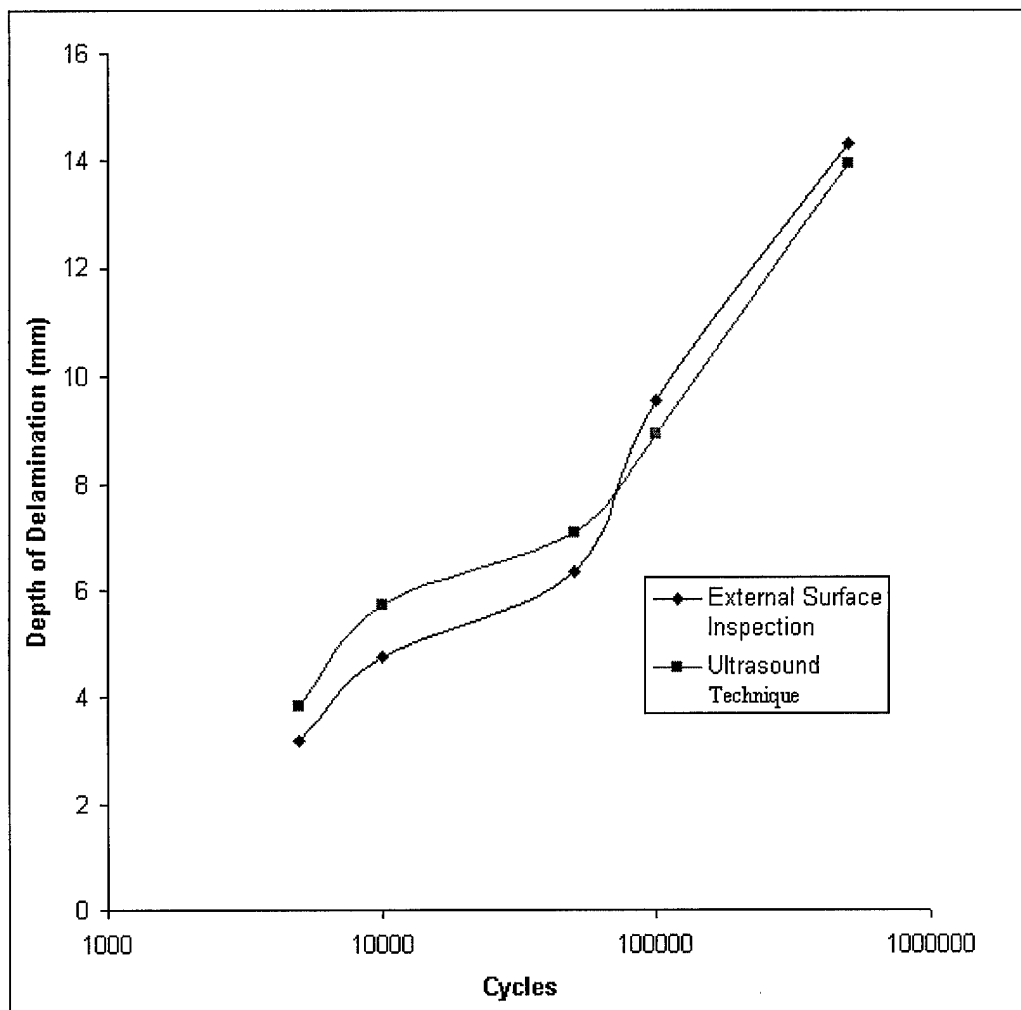


Figure 43. Comparison of External Surface and Ultrasound Inspection Methods - Specimen FT6

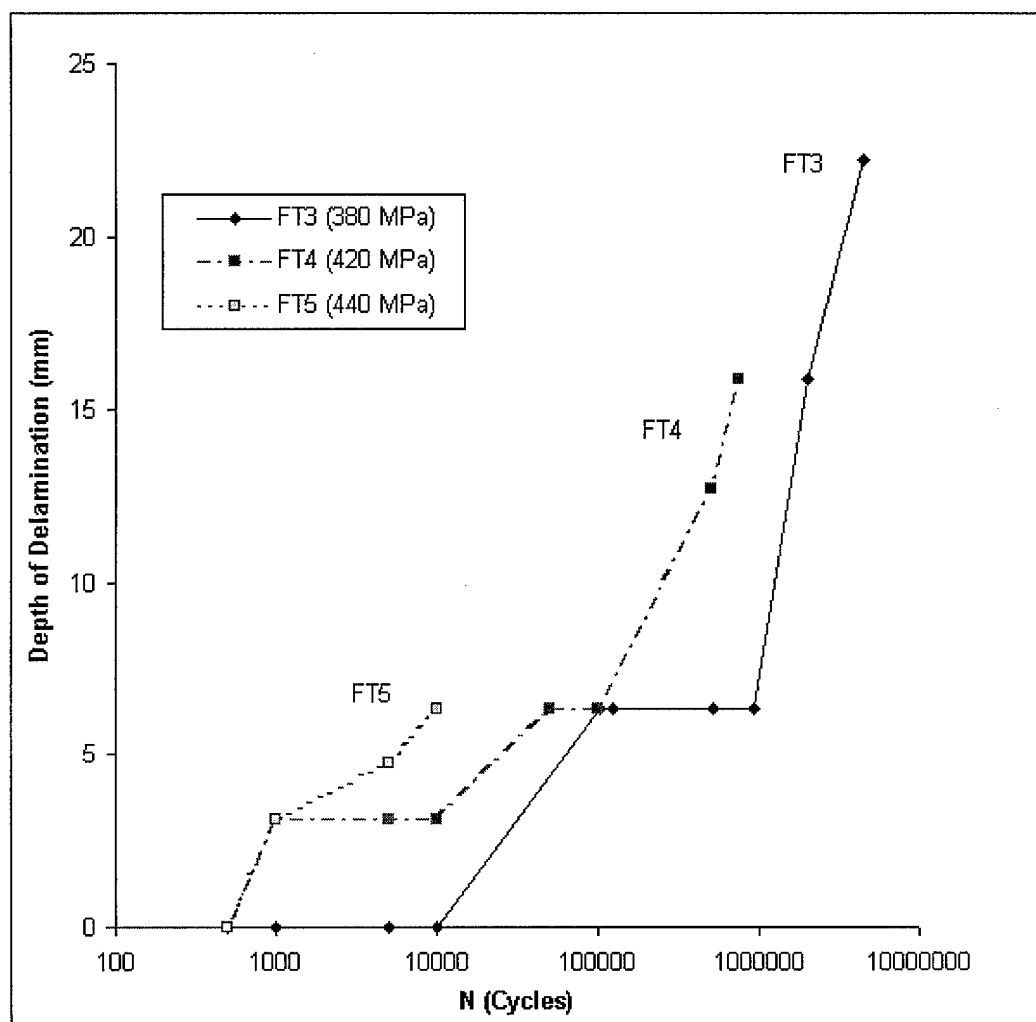


Figure 44. Depth of Delamination vs Cycles - FT Specimens

the lines in Figure 45 allow for clear reading of the data, but are not meant to imply the growth was linear, polynomial, logarithmic, etc. Overall, the basic trends for both AT and FT specimens were very comparable as shown in Figure 46. On the larger scale, the rates of delamination growth for all cycled specimens showed the same general trend. Specimens AT4 and FT5, which were loaded at 460 and 440 *MPa* respectively, have a higher rate of delamination. Specimens FT3 and AT1, which were loaded at 380 *MPa*, have the lowest rate of delamination growth.

As already stated, the rate of delamination progression was very similar for both AT and FT specimens, but there were some significant differences. These observed differences were the location of maximum delamination and the eventual effect on failure mode. The embedded PZT in the AT specimens seemed to reduce the overall extent of delamination for most of the test period, particularly when the PZT was slightly off-center, nearer one edge of the specimen. Figure 47 shows how the delamination away from the actuator was significantly greater than the delamination at the actuator. The square area outlined on the specimen at the bottom of the picture indicates the location of the PZT. The picture only shows the top half of the specimen in the MTS 647 Hydraulic Grips. This type of localized reduction in delamination was noticed for all AT specimens, but the "maximum" depth and width of delamination was generally very comparable to FT specimens, except at higher cycles. At higher cycles, the embedded PZT seemed to prevent total delamination through the specimen, until near failure. Figure 48 shows the differences in delamination of AT1 and FT3 at 2 million cycles. The total extent of delamination of AT1 was somewhat lower than FT3, even though both were cycled at 380 *MPa*. At 5 million cycles, the extent of damage was comparable, with the sensor area totally delaminated (Figure 49). Observations on the overall extent of delamination was not taken for every specimen, therefore more specimens would have to be tested in order to verify that embedded sensors cause less overall delamination.



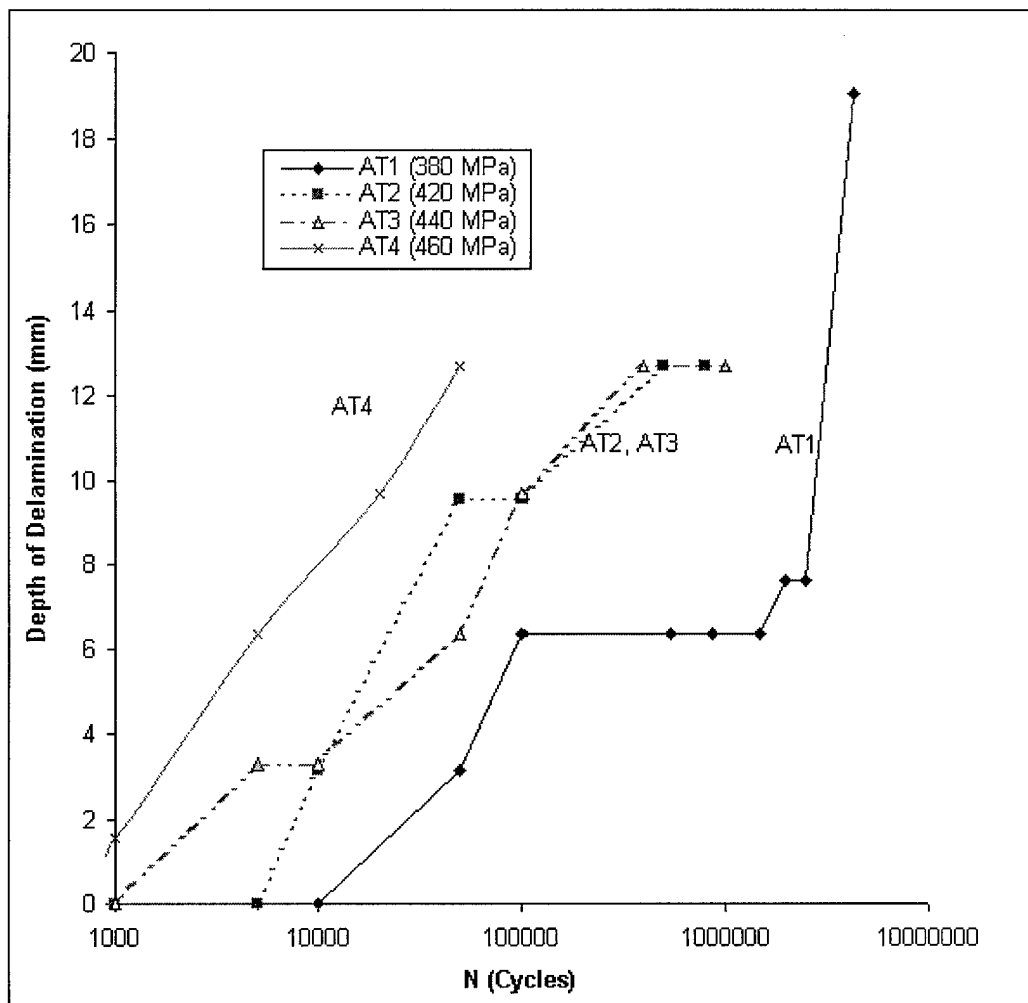


Figure 45. Depth of Delamination vs Cycles - AT Specimens

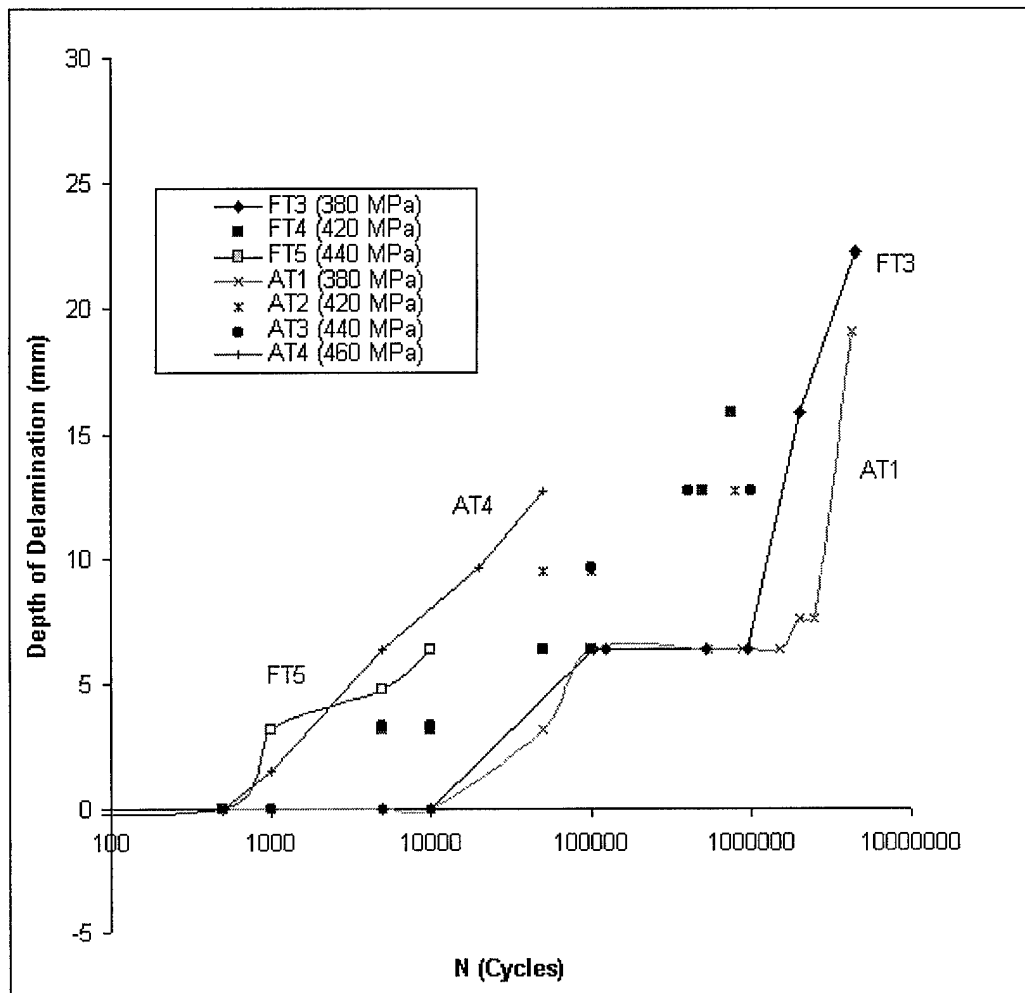


Figure 46. Depth of Delamination vs Cycles for All Specimens

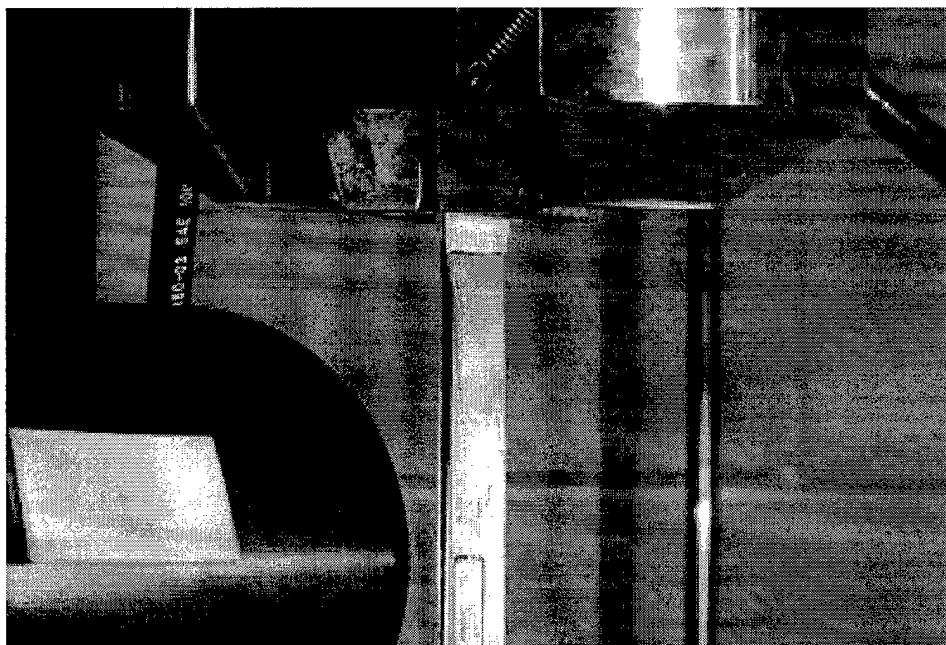


Figure 47. Edge View of AT2 at 500k Cycles



Figure 48. Overall Extent of Delamination of FT3 and AT1 at 2 Million Cycles

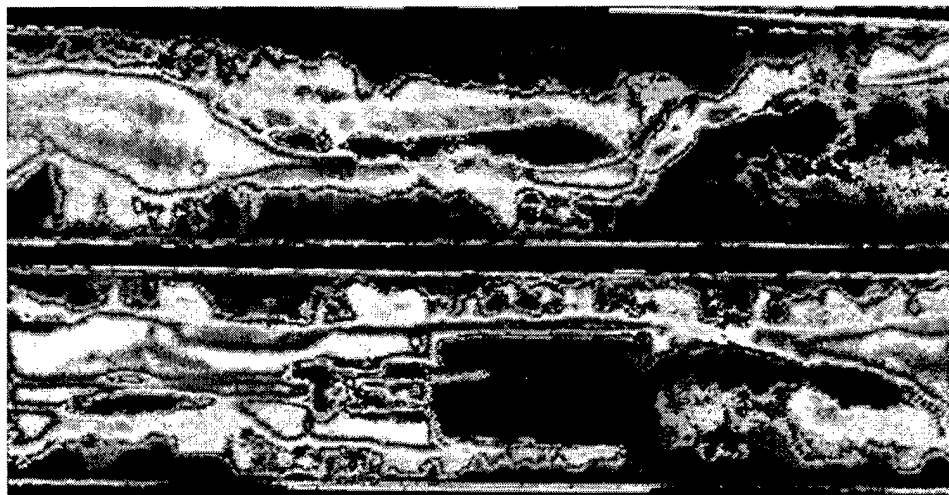


Figure 49. Overall Extent of Delamination of FT3 and AT1 at 5 Million Cycles

A second significant difference between the FT and AT specimens was the failure mode. Specimens AT2 and AT3 split into two halves, as mentioned earlier. Smoother surfaces in the middle of the specimen seem to indicate the middle section delaminated near final failure, which agreed with the ultrasound inspections of AT1. This could be attributed to the internal moments being generated due to the off-set embedded sensor. As one edge was only slightly delaminated, the other edge would delaminate similarly to FT specimens. Another factor could be the delamination of the PZT. As the brittle ceramic and isolation barrier of the PZT delaminated, the entire width near this section split in one instance. When ultimate failure occurred, the normal stresses, moments, and the greatly weakened area in the middle resulted in the splitting of the AT specimen into two parts.

To summarize, the rate of delamination growth of AT and FT specimens during most of the fatigue life were comparable, with no significant variations, which is contrary to previous reports using glass inserts [9, 18]. The location and extent of the delamination were shown to be quite different however. In the AT specimens, the embedded sensor seemed to reduce the extent of delamination at the middle of the specimen, until final failure. Ultrasound inspection of AT1 confirmed the delamination was reduced near the PZT. Since delamination was primarily a result of edge effects, the sensor would seem to have lowered the normal tensile stresses due to Poisson's effect [6]. Near failure however, two AT specimens completely delaminated and split into two parts. This would indicate the embedded sensor initially prevented delamination growth to some extent, but catastrophically split at failure in two cases. The exact nature could be tentatively attributed to the brittle nature of the PZT and the internal moment and stress variations due to the embedded sensor.

### 4.2.3 Degradation of PZT Output

#### 4.2.3.1 Voltage Degradation from Fatigue Loading

As briefly discussed earlier, the voltage output of the embedded PZTs degraded sharply after the first cycle of the high stress (380-460 MPa) fatigue loading. Specimen AT1 was typical of all the AT specimens and will be used as the typical example. The voltage output initially saturated the MTS console's upper limit, then degraded into a typical strain versus voltage loop, as shown in Figure 50. After the initial damage, the voltage loops degraded in shape and magnitude at a relatively slower rate. Figure 51 shows that, after 10,000 cycles, the form and magnitude of the loops changed drastically. At this point, the voltage output remained constant over a region, which could be attributed to the voltage offset of the measurement equipment. Since the applied high strain levels were far beyond the sensor design limits as provided by its manufacturer ACX, the stress was also reduced to measure the sensor output at lower strain values [2]. Before the initial fatigue cycle, AT1 was cycled at 60 MPa. This initial loop is shown in Figure 52. After only 500 cycles, the strain versus voltage loops changed drastically in form and magnitude, which is shown in Figure 53. The magnitude dropped by a factor of ten, while the loop crossed early in the cycle. This general shape stayed the same for over 500,000 cycles, while the voltage output actually increased very slightly.

While mechanical stresses have been shown to "switch" the polarity of PZTs, the results of this study do not necessarily indicate switching. 180° switching would have flipped the strain versus voltage loop, similar to what was seen in Figure 53. However, 180° switching would be more likely in applied electric fields [13, 14]. Mechanical depolarization usually results in 90° switching, which could have contributed significantly to the voltage reduction, but not necessarily to the shape of the waveform. Therefore, the waveform change seems to be linked to the structural damage of the laminate and/or the PZT, which may be the most likely

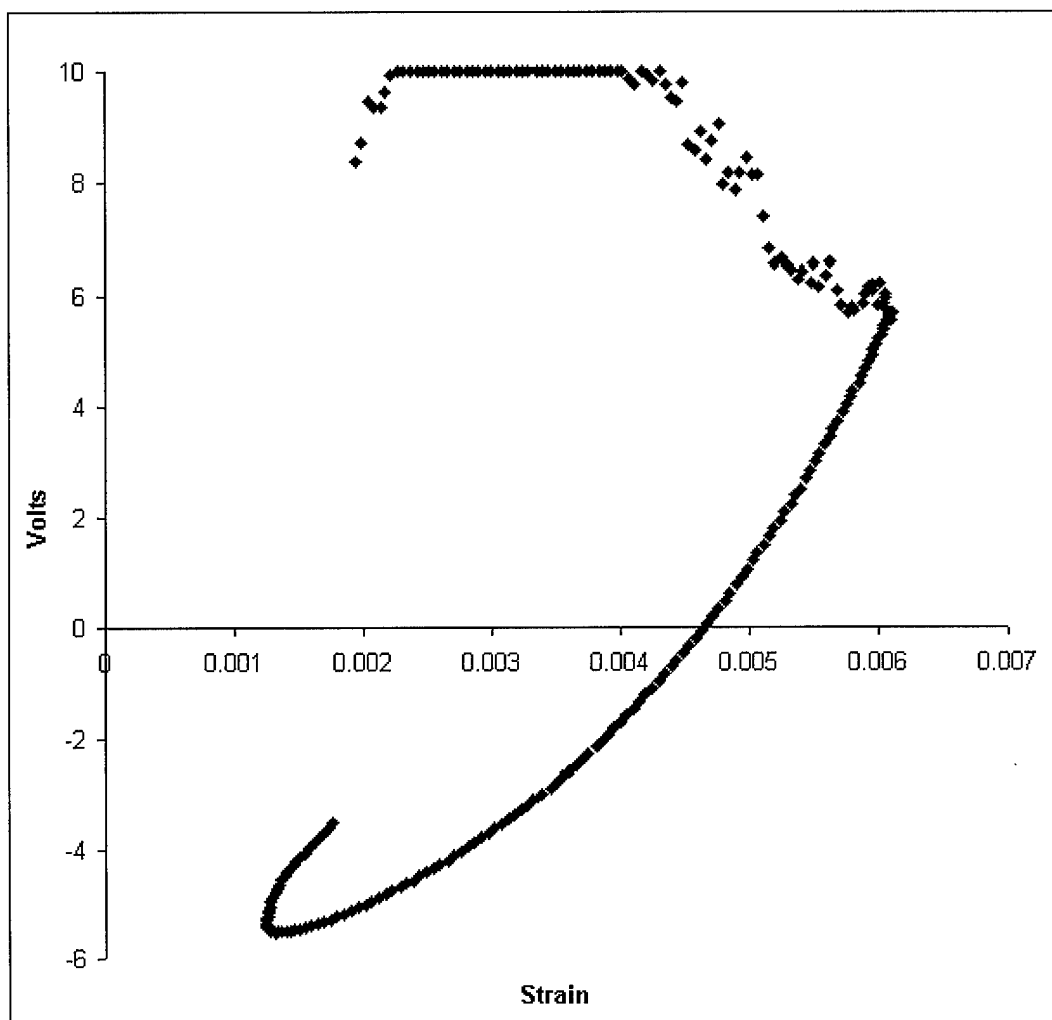


Figure 50. Output Voltage vs Strain - Specimen AT1, Cycle 1, (380 MPa)

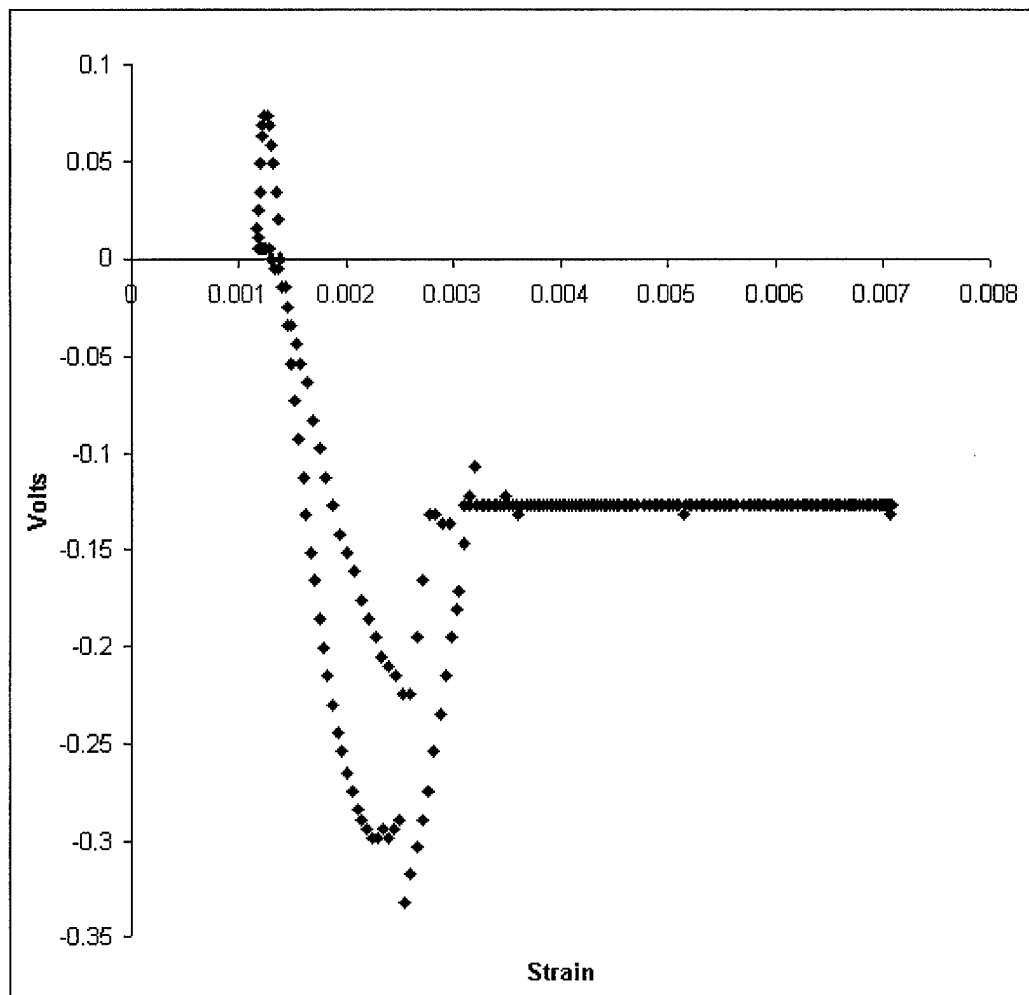


Figure 51. Output Voltage vs Strain - Specimen AT1, Cycle 10,000. (380 MPa)



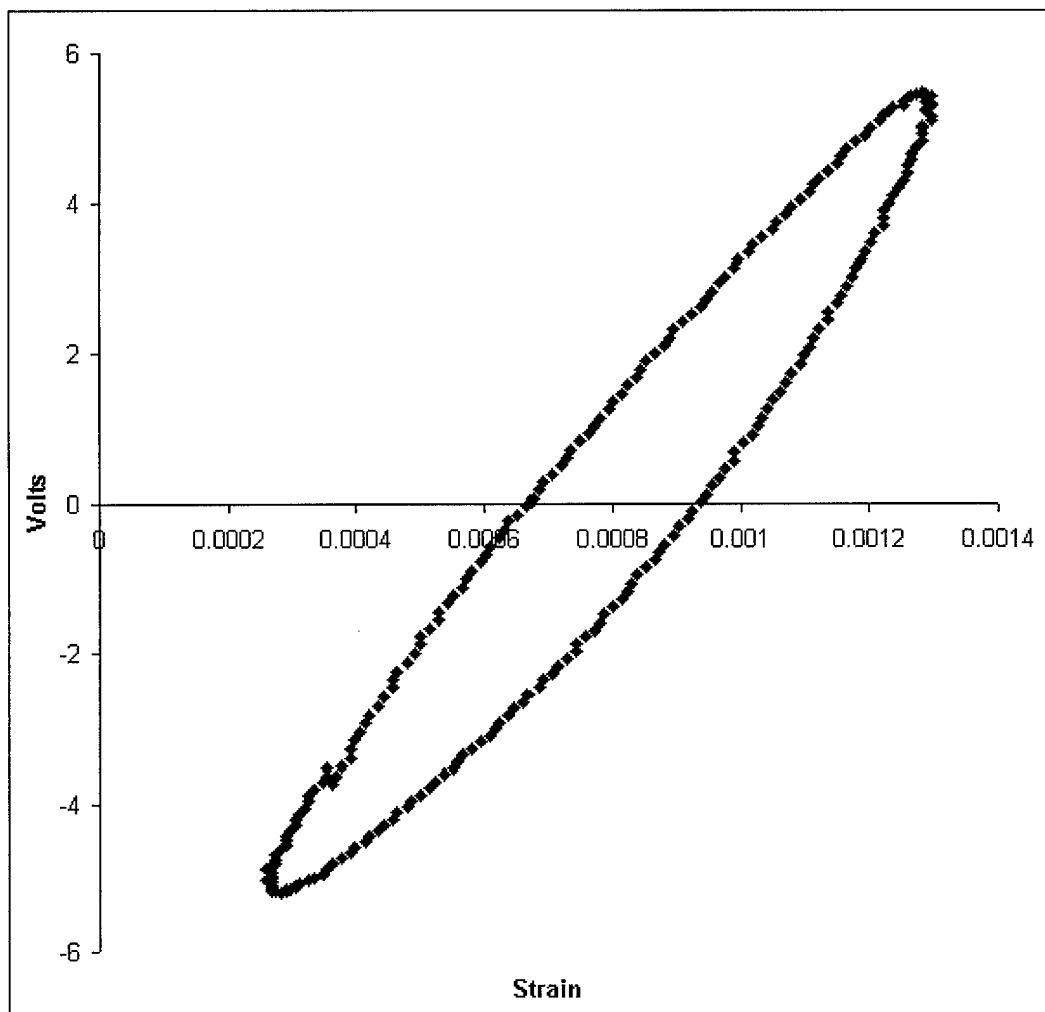


Figure 52. Output Voltage vs Strain - Specimen AT1, Cycle 1 (60 MPa)

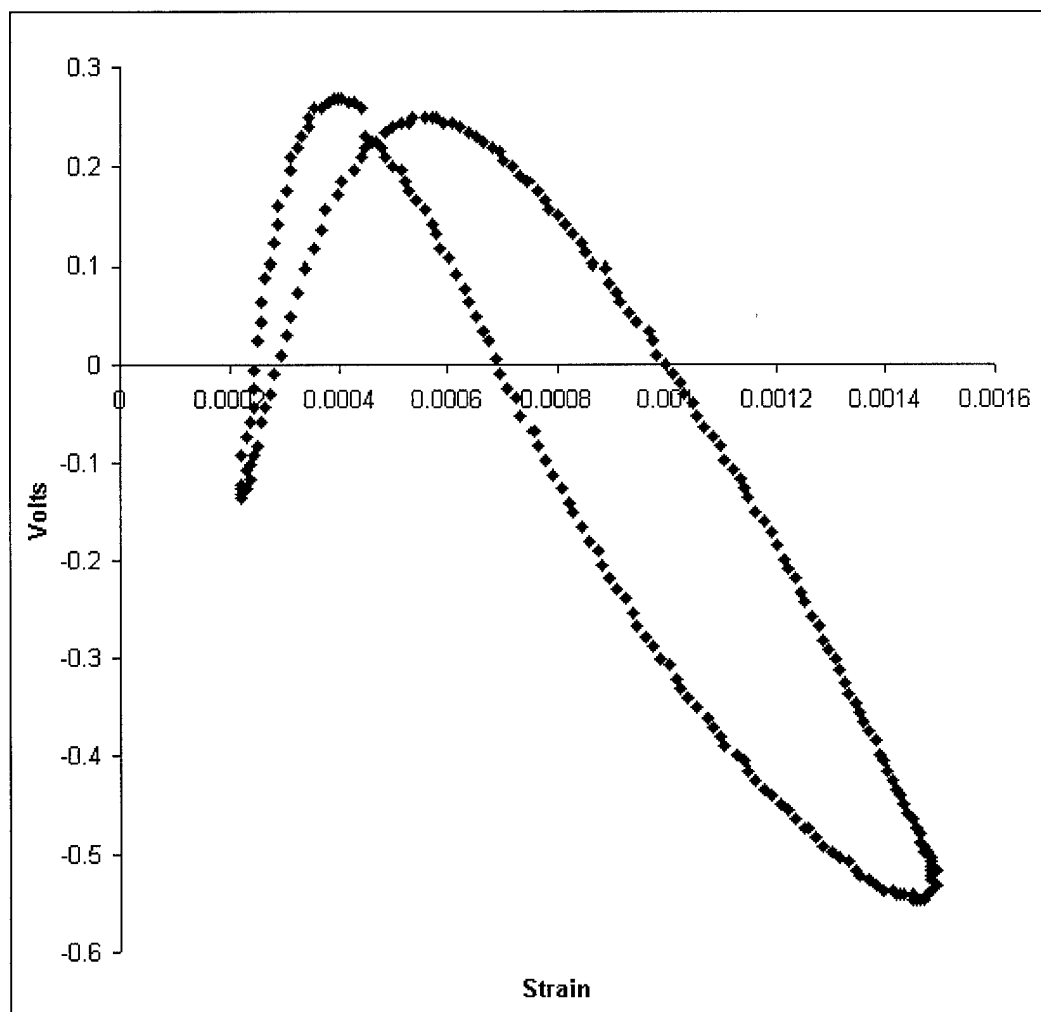


Figure 53. Output Voltage vs Strain - Specimen AT1, Cycle 500 (76 MPa)

cause. The laminate transversely cracked after the first cycle, and damage progressed thereafter. Monotonic results indicated that PZT output dropped by over 50 % after the first transverse crack occurred. Concerning the PZT, the capacitance measurements remained constant, which would seem to indicate a good circuit, but the monotonic tests have also shown how capacitance can be improved under mechanical loading. In addition, PZT cracking was found in specimen AT3 after the specimen had split, even though the capacitance was constant up to that point. Since capacitance seems to be a weak indicator about the health of a PZT, the PZT could have sustained major cracking damage and lead wire connection damage as well. Looking at all the different possible factors, the voltage degradation was most likely due to a combination of depolarization, delamination, matrix cracking, PZT cracking, and lead wire damage.

#### **4.2.3.2 Low-Strain versus Cycles Curve**

Specimens AT5, AT6, AT7, and AT8 were tested at the low-strain levels to investigate the effects of fatigue loading on the embedded PZT in the composite laminate. Each specimen was inspected before and after cycling for cracking or delamination by the QRMS-II and Nikon microscope. Ultrasound and X-ray inspection were used on two specimens. X-ray inspection proved unsubstantial, since cracking at the edge was necessary for the dye penetrant to show damage. Ultrasound inspection showed that some minor damage may have occurred, but was not very clear.

Specimen AT5 was manufactured with the sensor off-center, so the sensor could be inspected at the edge (See Figure 54). AT5 was originally cycled at  $200 \mu\epsilon$  for 2 million cycles, where no degradation of output was measured. The stress level was then increased to  $50 \text{ MPa}$ , which resulted in a maximum strain of approximately  $1000 \mu\epsilon$ . Figure 55 shows how the voltage output remained relatively constant for 2 million cycles. The level of strain was then increased to  $2000 \mu\epsilon$ , which was twice the maximum value recommended by ACX. After only 10,000

cycles, the output dropped by over 40 %. No cracking was found by microscope, ultrasound, or X-ray analysis. The epoxy rich regions surrounding the sensor can be seen in Figure 56. The bonding region at the top and bottom surfaces remained visibly unchanged as well, which is shown more closely in Figure 57. The outer protective coating of the PZT can also be seen in Figure 57. Further, the capacitance of the PZT remained constant.

Before the damage occurred, AT5 was also used to obtain a reference, strain versus voltage output curve. All the AT specimens tested under the low-strain conditions, except AT8, had voltage outputs which originally fell on this curve. Therefore, the embedded specimens demonstrated a consistent output with applied mechanical loads, until some damage occurred. Figure 58 shows the linear response of the sensor to increasing levels of applied stress. The top line is the maximum positive voltage, while the bottom line corresponds to the minimum voltage output of the sensor under cyclic tensile loading.

Specimens AT6, AT7, and AT8 were all tested above  $1000 \mu\epsilon$  in order to determine the degradation of voltage output and a strain to failure curve for the embedded sensors based upon its voltage degradation. Specimens AT6 and AT7 were cycled at 65 and 75 MPa, which resulted in the 40% voltage drop failure after only 10,000 to 35,000 cycles. AT8 was cycled at approximately  $1100 \mu\epsilon$ , where the output remained constant for over 1 million cycles. AT8's output was suspect however, since the initial voltage output was far below the expected found from AT5's reference curves. This would indicate damage had already occurred in AT8 before cycling. Ultrasound inspection confirmed delamination around the lead wire section had occurred before testing. Therefore, this point was thrown out of the results. The final results are plotted in Figures 59 and 60.

In summary, four AT specimens were cycled at 16 Hz,  $R = 0.1$ , constant amplitude, load control. The maximum strain tested,  $2000 \mu\epsilon$ , was twice the upper limit given by ACX.

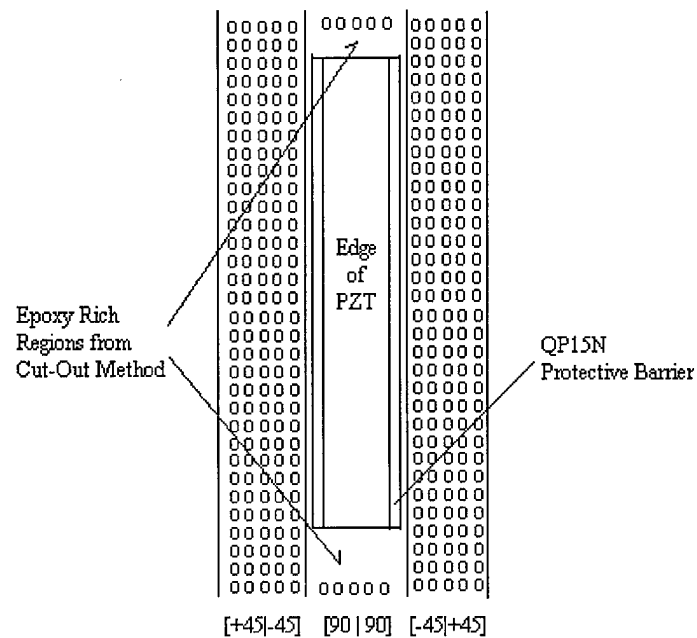


Figure 54. Schematic Edge View of Specimen AT5 with the Embedded PZT at the Edge

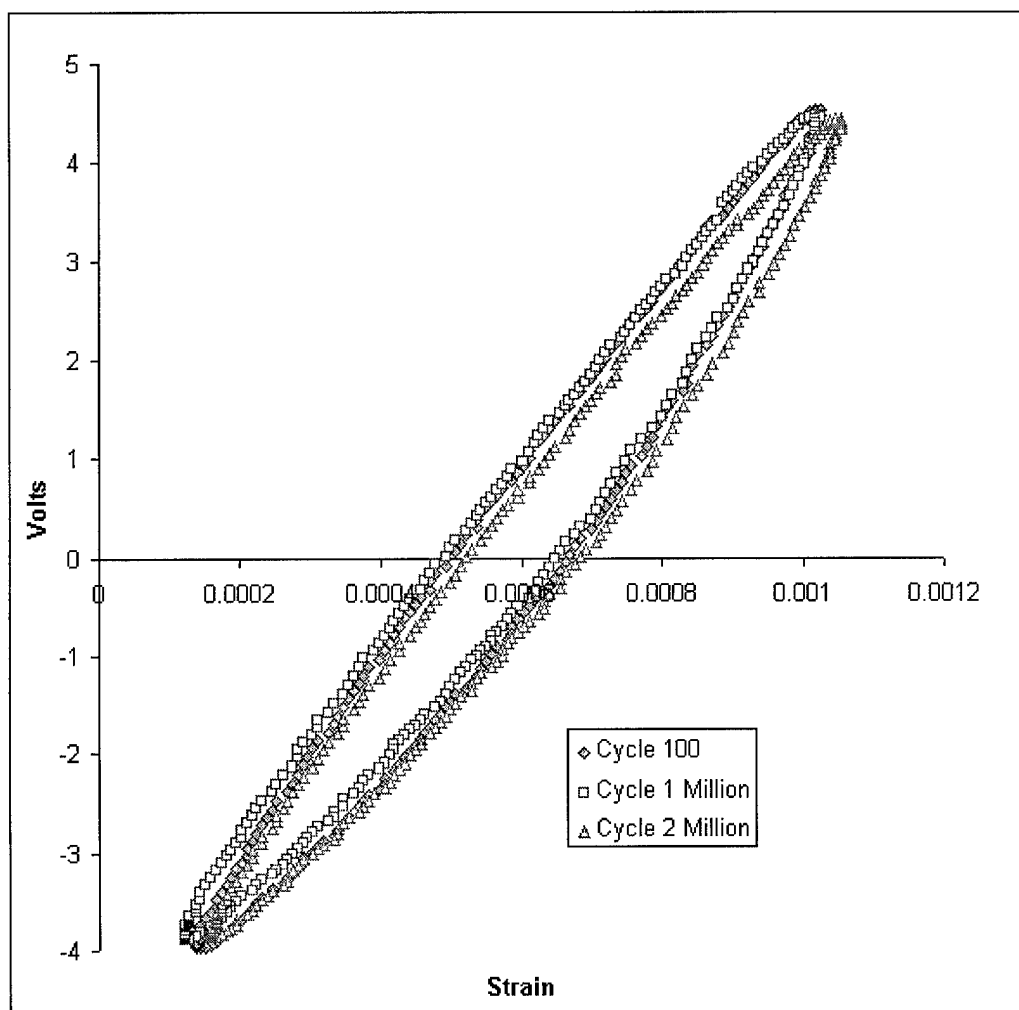


Figure 55. Voltage vs Strain - Specimen AT5 , Comparison of Output at  $1000 \mu\epsilon$

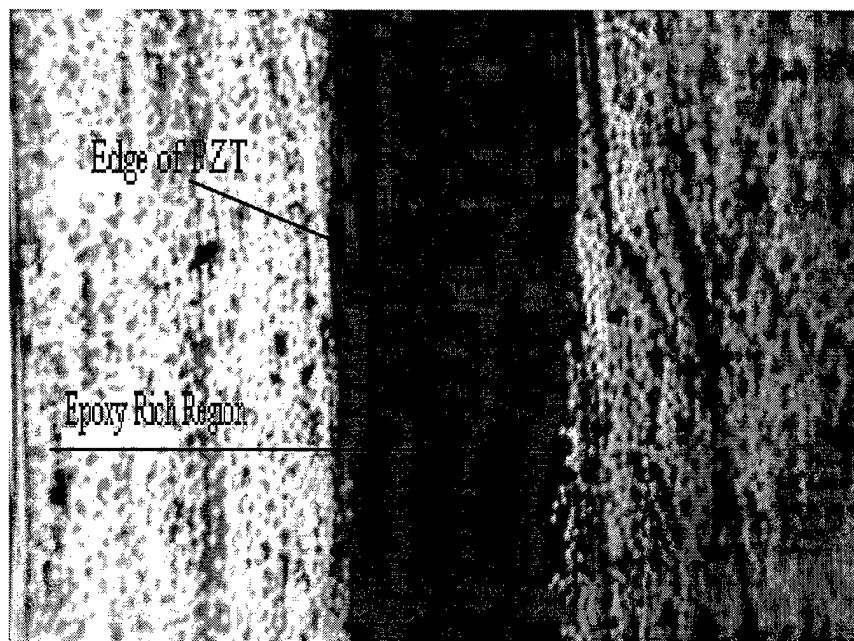


Figure 56. Epoxy Rich Region Due to Cut-out Method - Specimen AT5

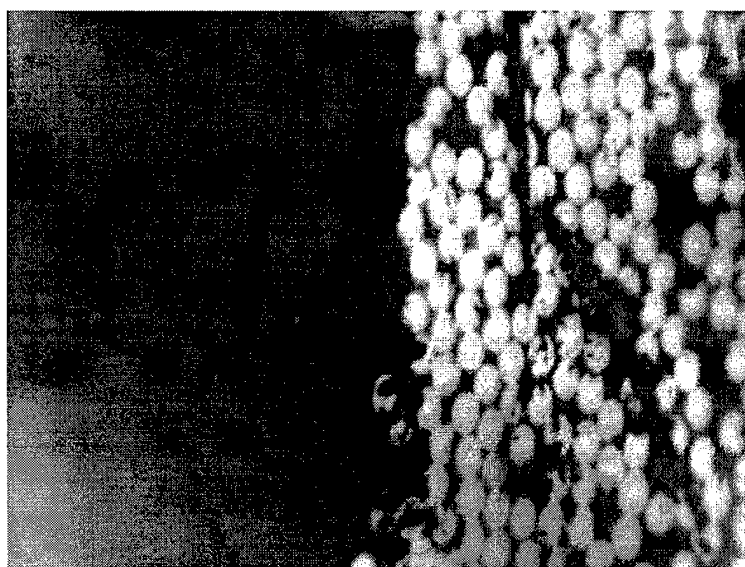


Figure 57. Bonding Interface Between PZT and Plies - Specimen AT5

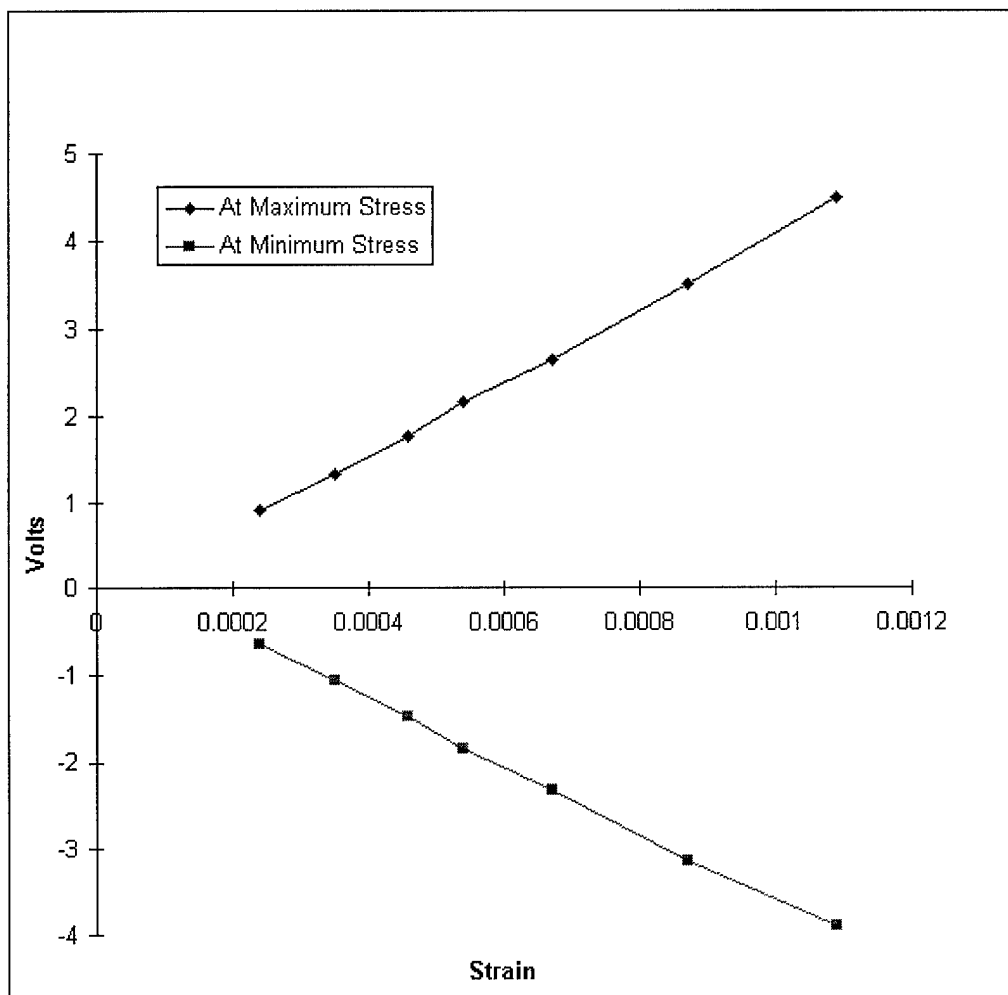


Figure 58. Voltage Output vs Strain Calibration During Cycling - Specimen AT5



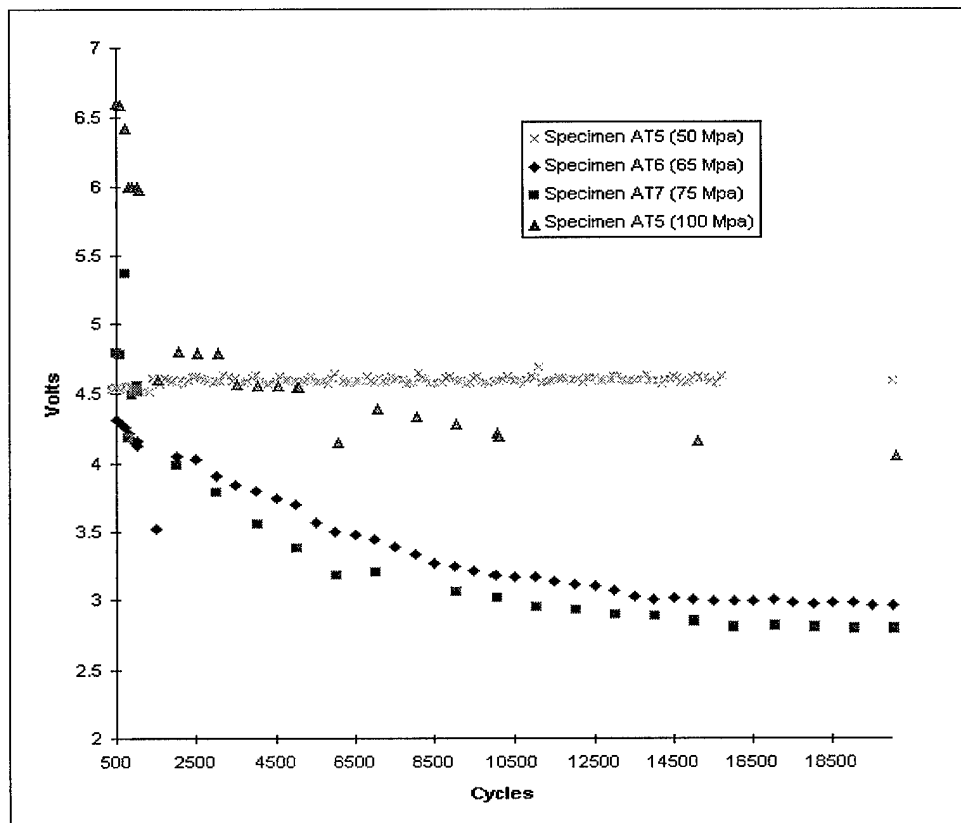


Figure 59. Voltage Degradation vs Cycles

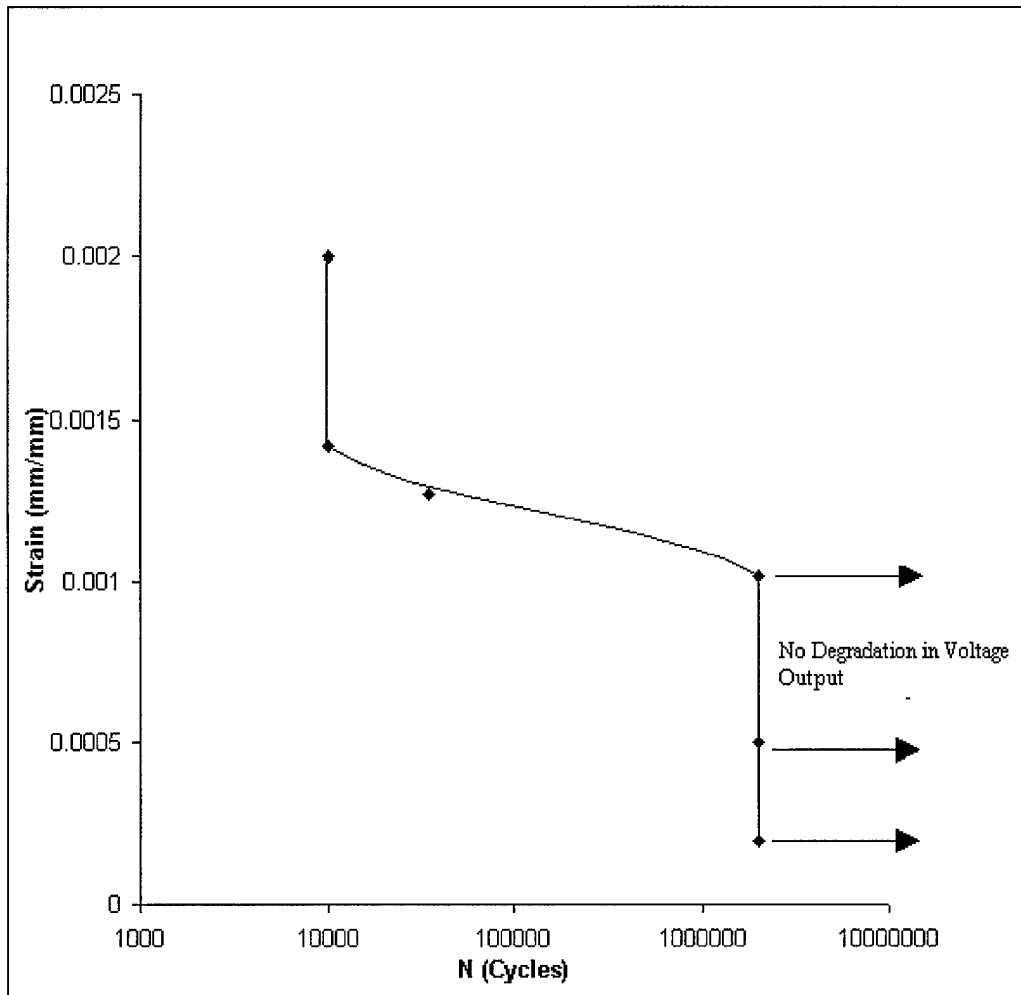


Figure 60. Strain vs Cycles to Sensor Failure, Based on 40 % Reduction of Voltage Output

Results showed that the PZT voltage output stayed constant for over 2 million cycles, when the sensor was cycled at 1000  $\mu\epsilon$  and below. Above this limit, the output degraded quickly after only thousands of cycles. Failure was taken to be a reduction of 40 % of the original voltage output. Ultrasound inspection of a couple of specimens showed possibly minor damage and delamination around the lead wire section, but AT5 showed no signs of delamination or cracking. X-ray inspection of AT5 also did not indicate any damage had occurred to the laminate. Figure 60 shows the dramatic drop-off when the upper strain limit is reached. Capacitance measurements were relatively constant throughout all testing, and repoling the specimens did not result in improved voltage outputs. Since nondestructive inspection methods did not indicate any significant damage to the laminate, damage to the PZT due to the higher applied strains about 1000  $\mu\epsilon$  seems to be the primary reason for the degradation in output voltage. Nevertheless, the PZT did perform very well during cycling up to the manufacturer's design limit of 1000  $\mu\epsilon$ .

## 5. Conclusions and Recommendations

Results from this study indicate that it is possible to embed PZTs inside carbon-epoxy laminates without significantly affecting the tensile strength and fatigue life of the composite. Results from the monotonic tests showed that the average ultimate stress and modulus for specimens with and without PZTs were within 4% of each other, which was not very significant considering the relatively large embedded PZT. The range of the ultimate strengths found during this study were not uncommon, since past studies have shown that the same type of specimen might fail with a scatter of 100 *MPa*. This natural variation is primarily due to material and manufacturing differences of the laminate [12, 16]. A comparison of the stress-strain curves (strain gage data) obtained from un-interrupted tests (FT8 and ATST2) showed little differences as well. Stress-strain curves initially had a constant slope, but tended to start curving downward at approximately the same stress levels. In addition, all monotonically loaded specimens had similar transverse failure planes and limited edge delamination. There were some differences found in the interrupted test results, but these were attributed to specimen variation, since the location of the damage did not seem to depend on the PZT location. Observed differences are certainly within expected variances due to material inhomogeneities, test differences, etc.

Fatigue test results showed some differences, but overall indicated no significant degradation to the structure due to the embedded PZT. S-N curves for both types of specimens with and without PZTs indicated that the fatigue strengths were very similar. In fact, AT specimens (with PZTs) actually had a slightly better fatigue strength. While the strengths were very comparable, one noticeable trend was a sharper drop-off of the modulus for AT specimens. While this may have been tentatively attributed to the embedded sensor, the natural variation in each specimen's material properties and extensometer data could have caused many of the differ-

ences between specimens. The extensometer, in particular, was found to slip when the edges became severely damaged. Since AT specimens generally had less delamination near the PZT, perhaps less slippage resulted and a more accurate measurement of the modulus was made near failure. The overall range in modulus reduction for FT and AT specimens were usually within 5-15 % of each other. The rate of delamination growth of AT and FT specimens during most of the fatigue life was very comparable, with no significant variations, which was contrary to previous reports using glass inserts [9, 18]. The location and extent of the delamination between both types of specimens were shown to be different. As mentioned earlier, the embedded sensor seemed to reduce the extent of delamination at the middle of the specimen, until final failure. Near ultimate failure, two AT specimens completely delaminated and split into two parts. This would indicate that the embedded sensor initially prevented delamination growth to some extent, but catastrophically split at failure in these two cases. The embedded PZT was split down the middle as well, indicating the bonding interface to the plies was stronger than the interface between the plates of the PZT. Nevertheless, the AT specimens generally survived more cycles than the FT specimens.

Overall, the initial sequence of damage in all specimens in this study agreed with previous investigations on the damage mechanisms for  $[0 \mid \pm 45 \mid 90]_S$  quasi-isotropic laminates. First, the  $90^\circ$  plies transversely cracked and slightly decreased the modulus. Resulting stress concentrations near the cracks resulted in further cracking near this area as the load was increased further. Longitudinal cracking and delamination then occurred as the edge effects caused the plies to pull apart at the edge.

In addition to the strength and fatigue results, this study showed that PZTs can maintain a steady output indefinitely when mechanically cycled within the operational strain limits. At low-strain levels (200-1000  $\mu\epsilon$ ), the voltage output remained constant for millions of cycles.

The bonding interface between the PZT and surrounding plies showed no signs of damage when cycled in this range. However, as the level of strain was gradually increased, the voltage output dropped off sharply. During the interrupted monotonic load tests, where higher loads were applied, the first laminate cracks resulted in a significant drop of over 50 % in voltage output of the embedded sensor. Under fatigue loading at high strain, the sensor output dropped immediately after the first cycle, then eventually degraded to zero. The exact damage mechanism could be a combination of depolarization, sensor deformation, grounding, and matrix cracking.

A number of items should be addressed in the future concerning this study. First, more specimens should be tested to statistically verify these results. In addition, improvements in mounting the extensometer must be made to prevent test variation of modulus measurements. In the future, a modification to the knife edges should be made to enable the extensometer to be mounted on the face of the composite, where less damage occurs. Strain gages could also be used in addition to the extensometer. Concerning the health of the PZT, capacitance measurements do not seem to be a good indicator of a functional PZT. Even as the voltage output of the PZTs decreased under higher loads, capacitance measurements stayed constant throughout, giving no indication of damage by depolarization or cracking of the sensor. Therefore, other methods need be used to monitor the health of the PZT. An important aspect is differentiating whether the PZT or structure has caused the degradation in voltage output. One possible method would be to mount a strain gage to the embedded PZT, but the integrity of this system may be questionable.

## **APPENDIX A Laminate Properties and Equations**

Table 6. Material Properties of AS4-3501-6

Property	Symbol	Value
Fiber Volume	$V_f$ (%)	65
Longitudinal Modulus	$E_x$ (GPa)	137.9
Transverse Modulus	$E_y$ (GPa)	10.3
Shear Modulus	$G_{xy}$ (GPa)	5.5
Major Poisson's Ratio	$\nu_{xy}$	0.3
Tensile Strength in Longitudinal Direction	$\sigma_{xult}$ (MPa)	2,137.9
Tensile Strength in Transverse Direction	$\sigma_{yult}$ (MPa)	65.5
Shear Strength	$\tau_{xy}$ (MPa)	93.1

Table 7. Quasi-Isotropic Laminate Equations

thickness of actuator:	0.254 mm
thickness of plies	~0.127 mm
Number of plies	8
Total thickness (h)	~1.12 mm
Width	50.8 mm
$\begin{pmatrix} \sigma_1 \\ \sigma_2 \\ \tau_6 \end{pmatrix} = \begin{bmatrix} Q_{11} & Q_{12} & 0 \\ Q_{12} & Q_{22} & 0 \\ 0 & 0 & Q_{66} \end{bmatrix} * \begin{pmatrix} \varepsilon_1 \\ \varepsilon_2 \\ \gamma_6 \end{pmatrix}$	$\sigma_3 = 0 \quad \tau_{23} = \tau_{13} = \tau_4 = \tau_5 = 0$
$\begin{pmatrix} \sigma_x \\ \sigma_y \\ \tau_s \end{pmatrix} = \begin{bmatrix} Q_{xx} & Q_{xy} & Q_{xs} \\ Q_{yx} & Q_{yy} & Q_{ys} \\ Q_{sx} & Q_{sy} & Q_{ss} \end{bmatrix} * \begin{pmatrix} \varepsilon_x \\ \varepsilon_y \\ \gamma_s \end{pmatrix}$	Off-axis plies
$\begin{pmatrix} N_x \\ N_y \\ N_s \end{pmatrix} = \begin{bmatrix} A_{xx} & A_{yx} & A_{xs} \\ A_{yx} & A_{yy} & A_{ys} \\ A_{sx} & A_{sy} & A_{ss} \end{bmatrix} * \begin{pmatrix} \epsilon_x \\ \epsilon_y \\ \gamma_s \end{pmatrix}$	Total Laminte
$Q_{11} = \frac{E_1}{1-\nu_{12}*\nu_{21}}$ $Q_{22} = \frac{E_2}{1-\nu_{12}*\nu_{21}}$ $Q_{12} = \frac{\nu_{12}*E_2}{1-\nu_{12}*\nu_{21}}$ $Q_{66} = G_{12}$ $Q_{xx0} = Q_{11}$ $Q_{xx90} = Q_{22}$ $Q_{xx45} = \frac{1}{4} * (Q_{11} + Q_{12} + 2 * Q_{12} + 4 * Q_{66})$ $A_{xx} = \frac{h}{8} * (3 * Q_{11} + 3 * Q_{22} + 2 * Q_{12} + 4 * Q_{66})$ $A_{yy} = A_{xx}$ $A_{xy} = \frac{h}{8} * (6 * Q_{12} + Q_{11} + Q_{22} - 4 * Q_{66})$ $\bar{E}_x = \frac{1}{t} * (A_{xx} - \frac{(A_{xy})^2}{A_{xx}})$	138.9 GPa 10.4 GPa 3.12 GPa 5.52 GPa 138.9 GPa 10.4 GPa 42.59 GPa 2.62 GPa 2.62 GPa 0.803 GPa 53.9 MPa



## APPENDIX B Ply Discount Method

### B.1 First Ply Failure (Ultimate Strain)

Given for 90° plies:

$$\varepsilon_{xult} = 0.006$$

$$\sigma_{xu} = \bar{E}_x * \varepsilon_{xult}$$

$$E_{xestimated}: \sigma_{xu} = 53.916 \text{ GPa} * .006 = 323 \text{ MPa}$$

$$E_{xactual}(FT): \sigma_{xu} = 50.33 \text{ GPa} * .006 = 302 \text{ MPa}$$

$$E_{xactual}(AT): \sigma_{xu} = 48.8 \text{ GPa} * .006 = 293 \text{ MPa}$$

### B.2 Change in Modulus and Ultimate Strength

#### B.2.1 Modulus after 90° Plies Have Failed

Set Stiffness of 90° plies to zero:

$$Q_{xx90} = Q_{xy90} = Q_{ss90} = 0$$

Recalculate Extensional Stiffness Terms for Laminate:

$$A_{xx} = A_{yy} = \frac{h}{8} * (2Q_{xx0} + 2 * Q_{xx90} + 4 * Q_{xx45}) = 2.5404$$

$$A_{xy} = A_{yx} = \frac{h}{8} * (2Q_{xy0} + 2 * Q_{xy90} + 4 * Q_{xy45}) = 0.768$$

$$A_{ss} = \frac{h}{8} * (2Q_{ss0} + 2 * Q_{ss90} + 4 * Q_{ss45}) = 0.847$$

Use Quasi-Isotropic Relation for Laminate Modulus:

$$E_{xest'} = \frac{1}{h} * (A_{xx} - \frac{A_{xy}^2}{A_{yy}}) = 51.548 \text{ GPa}$$

$$E_{xest'} = 0.956 * E_{xestimated}$$

$$E_{xactual'} = 0.956 * E_{xactual} = 47.82 \text{ GPa (estimate of actual drop)}$$

### B.2.2 Estimated Ultimate Strength of Laminate at This Point

$$\begin{bmatrix} \varepsilon_x \\ \varepsilon_y \\ \gamma_s \end{bmatrix} = \begin{bmatrix} A_{xx} & A_{xy} & A_{xs} \\ A_{xy} & A_{yy} & A_{ys} \\ A_{xs} & A_{ys} & A_{ss} \end{bmatrix}^{-1} * \begin{bmatrix} N_x \\ N_y \\ N_s \end{bmatrix}$$

$$\begin{bmatrix} 2.504 & 0.768 & 0 \\ 0.768 & 2.504 & 0 \\ 0 & 0 & 0.847 \end{bmatrix}^{-1} = \begin{bmatrix} .441 & -.135 & 0 \\ -.135 & .441 & 0 \\ 0 & 0 & 1.181 \end{bmatrix}$$

$$\sigma_{xult} = \frac{\varepsilon_{xult}}{a_{xx}} * \frac{3}{4} \div h \text{ (effective thickness is 3/4 of original)}$$

$$\sigma_{xult} = \frac{0.015}{.441} * \frac{3}{4} \div 0.044 = 579.8 \text{ MPa}$$

### B.2.3 Modulus after -45° Plies Have Failed

Set Stiffness of -45° plies to zero:

$$Q_{xx-45} = Q_{xy-45} = Q_{ss-45} = 0$$

Recalculate Extensional Stiffness Terms for Laminate:

$$A_{xx} = A_{yy} = \frac{h}{8} * (2Q_{xx0} + 2 * Q_{xx90} + 2 * Q_{xx45}) = 2.016$$

$$A_{xy} = A_{yx} = \frac{h}{8} * (2Q_{xy0} + 2 * Q_{xy90} + 2 * Q_{xy45}) = 0.401$$

$$A_{ss} = \frac{h}{8} * (2Q_{ss0} + 2 * Q_{ss90} + 2 * Q_{ss45}) = 0.454$$

Use Quasi-Isotropic Relation for Laminate Modulus:

$$E_{xest'} = \frac{1}{h} * (A_{xx} - \frac{A_{xy}^2}{A_{yy}}) = 44 \text{ GPa}$$

$$E_{xest'} = 0.816 * E_{xest}$$

$$E_{xactual'} = 0.816 * 50 = 40.8 \text{ Gpa (estimate of actual)}$$

### B.2.4 Estimated Ultimate Strength of Laminate at This Point

$$\begin{bmatrix} \varepsilon_x \\ \varepsilon_y \\ \gamma_s \end{bmatrix} = \begin{bmatrix} A_{xx} & A_{xy} & A_{xs} \\ A_{xy} & A_{yy} & A_{ys} \\ A_{xs} & A_{ys} & A_{ss} \end{bmatrix}^{-1} * \begin{bmatrix} N_x \\ N_y \\ N_s \end{bmatrix}$$

$$\begin{bmatrix} 2.016 & 0.401 & 0 \\ 0.401 & 2.016 & 0 \\ 0 & 0 & 0.454 \end{bmatrix}^{-1} = \begin{bmatrix} 0.516 & -0.103 & 0 \\ -0.103 & 0.516 & 0 \\ 0 & 0 & 2.2 \end{bmatrix}$$

$$\sigma_{xult} = \frac{\varepsilon_{xult}}{a_{xx}} * \frac{3}{4} \div h \text{ (use effective thickness is } 3/4 \text{ of original)}$$

$$\sigma_{xult} = \frac{0.015}{.516} * \frac{3}{4} \div 0.044 = 495.5 \text{ MPa}$$

## APPENDIX C Capacitance Calculations

$$\text{Plate Capacitance (F)} = \frac{K_3^T * \epsilon_0 * l * w}{t}$$

where  $K_3^T$  is the dielectric constant,  $\epsilon_0$  is the permittivity of free space,  $l$  is the length,  $w$  is the width, and  $t$  is the thickness of the capacitor. Using the initial measured capacitance of specimen ATST1, the unknown constants can be found.

$$F_{ATST1} = 0.099 * 10^{-6} = \frac{(K_3^T * \epsilon_0) * l * w}{t}$$

The initial dimensions of the piezo wafer were given by ACX to be  $4.5974 \text{ cm} \times 2.0574 \text{ cm} \times .0127 \text{ cm}$ . From these dimensions,  $K_3^T * \epsilon_0$  was found to be initially equal to  $0.132925 \text{ nF/cm}$ .

If  $K_3^T * \epsilon_0$  remained constant under applied stress, the only variables would be the dimensions of the PZT ( $l$ ,  $w$ , and  $t$ ), which can be calculated by simple stress-strain relationships. The plane stress, stress-strain relationships are shown below, where  $\nu_{ij}$  is the Poisson's ratio.

$$\begin{aligned} \text{strain}_x &= \frac{\sigma_x}{E_x} \\ \text{strain}_y &= \nu_{xy} \frac{\sigma_x}{E_x} \\ \text{strain}_z &= \nu_{xz} \frac{\sigma_x}{E_x} \end{aligned}$$

In order to calculate the maximum potential change in dimensions of the PZT,  $\nu_{xy}$  was found to be 0.306 for the quasi-isotropic lay-up of AS4/3501-6.  $\nu_{xz}$  was taken to be approximately equal to  $\nu_{12}$  for a single ply, which was equal to 0.3. The resulting change in dimensions due to unidirectional tension were calculated by the following equations, where  $E_x$  was experimentally found to be  $50.6 \text{ GPa}$  for specimen ATST1. The resulting change in capacitance due to only the dimension changes are shown in fifth column of Table 8.

$$\begin{aligned}
l &= l_0 \left(1 + \frac{\sigma_x}{E_x}\right) \\
w &= w \left(1 - \nu_{xy} \frac{\sigma_x}{E_x}\right) \\
t &= t \left(1 - \nu_{xz} \frac{\sigma_x}{E_x}\right)
\end{aligned}$$

If  $K_3^T$  is not constant, but increases with applied mechanical loads, the capacitance would increase at a faster rate. To show this,  $K_3^T$  was increased by 25 *nF* per 50 *MPa* to match the rising experimental slope. (The permittivity of free space,  $\epsilon_0$ , is equal to  $8.85 * 10^{-14}$  *F/cm*.) Results of these calculations are shown in the last column of Table 8.

Table 8. Mathematical Change in Capacitance

Stress (MPa)	Length (cm)	Width (cm)	Thickness (cm)	nF (constant $K_T$ )	nF ( $K_T + 25$ )
100	4.5974	2.0574	0.012700	99.0	99.0
150	4.6111	2.0555	0.012692	99.3	100.9
200	4.6158	2.0549	0.012689	99.4	102.7
250	4.6204	2.0543	0.012685	99.5	104.4
300	4.6250	2.0537	0.012681	99.6	106.2
350	4.6296	2.0531	0.012677	99.7	107.9

## APPENDIX D Discussion of $[0|0|\pm 45|0|0|90]_S$ Testing

### D.1 Test Preparation

The  $[0|0|\pm 45|0|0|90]_S$ , AS4/3501-6 laminate was made by UDRI after a number of practice panels were constructed. The initial lay-up consisted of a  $30.4\text{ cm} \times 30.4\text{ cm}$  panel, embedded with two PZTs in the center  $90^\circ$  plies. Two  $5.08\text{ cm} \times 30.4\text{ cm}$  specimens were cut from the panel using a diamond saw. One of the specimens, AAT1, contained an embedded PZT which was previously known to be "bad". This specimen was mechanically fatigued under tension-tension constant amplitude loading at a frequency of 10 Hz. Most of the fatigue test was run at 40% of the expected ultimate stress, but additional testing was also conducted at 68% to inspect for further damage. In order to monitor crack initiation and growth, one side of each specimen was polished using a series of larger grit sizes leading up to 5 micron polishing liquid. The QRMS optics system was used to inspect for damage. The second specimen, AAT2, was monitored for both damage progression and PZT degradation. An overview of these tests are discussed the following sections. An important note is that both PZTs were embedded by the cut-out method, and capacitance was checked at intermediate check points.

### D.2 Specimen AAT1, 40% Load (552 MPa) Damage Progression

Cycle 0 to 8000. Extensometer was attached on the back edge of the specimen, surrounding the length where the embedded actuator was located. Rubber bands were used to attach the extensometer, which has proved to be risky. Our first effort stopped after the equipment started making unusual noises. After the first 8,000 cycles the optics machine revealed severe delamination in the  $90^\circ$  plies, running the length of the composite. Immediate damage was expected, since the displacement was above the calculated first ply failure of these plies. No transverse cracks in the other plies were seen via the optics or under the microscope. At this point, the

transverse and longitudinal cracking in the  $90^\circ$  plies effectively eliminated the load carried capability. The modulus was calculated as  $80 \text{ MPa}$ . There is some question regarding the validity of this first part, due to the abnormal load cycle seen from the equipment. Further testing was done to correct the problems seen.

#### Cycles 8000 to 15000

In another attempt to start the test, Material Test System 810 (MTS) anomalies were again found, where the load cycle was not properly operating. The MTS was subsequently taken apart to reduce noticeable vibration, and the load card and output were electrically analyzed for faults. No further damage was noted, but the specimen was accidentally compressed twice, thereby introducing some additional damage outside the tension-tension testing. Inspection of the edge under the microscope did not indicate further damage. Modulus in this time frame stayed approximately the same.

#### Cycles 15000 to 42000

After the MTS problems were rectified, the fatigue test continued until the rubber bands of the extensometer broke at 42,000 cycles. Inspection of the edge for additional cracks was conducted at this time. Using the QRMS optical system, delamination and cracking were found not to have grown noticeably at the  $0^\circ$  plies interfaces surrounding the middle plies. No noticeable cracks were seen in the  $45^\circ$  plies. Modulus at this time remained relatively constant.

#### Cycles 42,000 to 600,000

The bottom rubber bands were replaced by a spring wire system, which proved to be an improved system for holding the extensometer in place. Modulus stayed at constant for quite some time. After approximately 600,000 cycles the extensometer fell off again. After inspecting the lay-up, the middle  $90^\circ$  plies have separated even further (longitudinal cracks along the length). There seems to be some cracking in the other plies as well, but these were less preva-



lent. The  $0^\circ$ plies surrounding the middle seem to be cracking, while the  $45^\circ$ plies on the outside have less noticeable cracking.

#### Cycles 600,000 to 800,000

Modulus upon reconnection remained relatively constant. More cracking in the matrix may have occurred, but the fibers still seemed to be healthy. Upon optics inspection, the near side  $45^\circ$ plies had hardly any damage, while the opposite side showed cracking and some delamination in places. The composite at this time looked like two composites, since the center was close to being nonexistent.

#### Cycles 800,000 to 2,400,000

A hydraulic failure caused the test to be delayed for about a day. The modulus rose slightly, which may not indicate a true change, since the extensometer could have been slipping slightly as the edge became more damaged. At 1,311,523 cycles the extensometer fell off again, but went unnoticed, since it happened over night. When the test was restarted at 1,500,000 cycles, the MTS once again started to vibrate badly. This may have been the reason the extensometer kept falling off the composite. Even without the vibration, the extensometer fell off again, which would indicate the edge damage was causing the extensometer to fall off. Once again, the entire edge was inspected, primarily looking at the inner  $0^\circ$ plies and the adjacent  $45^\circ$ plies. It appeared that some damage was continuing on the right side of the composite, with some delamination and matrix cracking appearing in the adjacent plies. On the left side, the plies looked healthy, with some possible minor cracking. The modulus is  $87\text{ GPa}$ , while the strain is currently .00579.

After 2 million cycles, "failure" was determined to have already occurred, even though the composite was still supporting the load. The load was further increased to 68% for another 400 thousand cycles. This caused delaminations at the edges of all plies, with the  $90^\circ$  coming

apart dramatically. There could be a number of reasons which explain the delamination at the edges, which did not go through the entire width of the lay-up.. First, stress concentration may have existed at the edge. Second, there may have been some bending moments involved once the  $90^\circ$  longitudinally cracked, thereby causing the edges to separate permanently. Third, the carbon fibers may have experienced permanent deformation from Poisson's effect, which caused the bowing effect at the edges when the load was released. Fourth, the  $\pm 45^\circ$  plies have a natural tendency to align itself with the direction of the stress, which may cause the noticeable separation at the edges. Nevertheless, the composite was still supporting the applied load. The modulus ( $80\text{-}87\text{ GPa}$ ) during this time was questionable due to the damage on the edges, since the extensometer would not stay on. In the future, the extensometer should be put on during critical measurement periods, leaving it off for most of the time.

#### **D.2.1 Lessons Learned**

1. Only put the extensometer on when collecting data; preferably at lower loads, and at the beginning and when the modulus has become rather constant. (Phase I continuous, Phase II intermittent, Phase III too far out there) 2. Realistically, failure occurred before ultimate failure. We must decide the criteria for failure of this lay-up.. The  $0^\circ$  plies held the higher loads, while the matrix came apart at the seams.

3. The optical equipment detects cracks, but micro-crack initiation cannot be detected at the very small scale. The embedded sensor did not seem to have much effect on when or where the  $90^\circ$  plies failed. This was a reasonable observation, since the applied load was past the first ply failure.

4. The MTS 810 was too small for high load testing, which may or may not be a problem. Since the lay-up was holding higher loads because of the  $0^\circ$  plies, ultimate failure would occur far beyond where the matrix has cracked and plies have delaminated. In reality, the actuator

4. The MTS 810 was too small for high load testing, which may or may not be a problem. Since the lay-up was holding higher loads because of the  $0^\circ$ plies, ultimate failure would occur far beyond where the matrix has cracked and plies have delaminated. In reality, the actuator would probably be considered useless at this point anyway. If failure was determined by when the actuator data goes erroneous, then there would be a question of whether the interface or the actuator failed. These types of tests should be conducted under lower loads, which is really indicative of the operational environment the composite would see.

### **D.3 Specimen AAT2, 443 MPa, PZT Response to Mechanical Cycling**

The damage progression of AAT2 was very similar to AAT1, therefore the details of the progression of damage were not repeated in this section. The focus of testing AAT2 was on understanding the output of the embedded PZT, therefore the tension-tension fatigue loading was set near the expected FPF ( $450\text{ MPa}$ ). Figure 61 shows the linear stress-strain curve, taken before fatigue testing, which did not indicate significant damage at the applied static load.

At approximately 1,000,000 cycles, the crack density appeared to saturate. Capacitance measurements were taken at the same time, to indicate whether crack density had an effect on capacitance. No significant effect was noticed (See Figure 62).

Since the electrical test setup was different from what was used for the  $[0|\pm 45|90]_S$  laminate, the output voltage could not be directly compared with this laminate. But, the general linear response seemed very similar to what was found in the AT specimens. Figure 63 shows how the voltage output almost linearly increases with increasing applied stress (strain). However, the voltage output seemed to degrade at the higher strains, which would indicate damage or the operational limit of the PZT was breached.

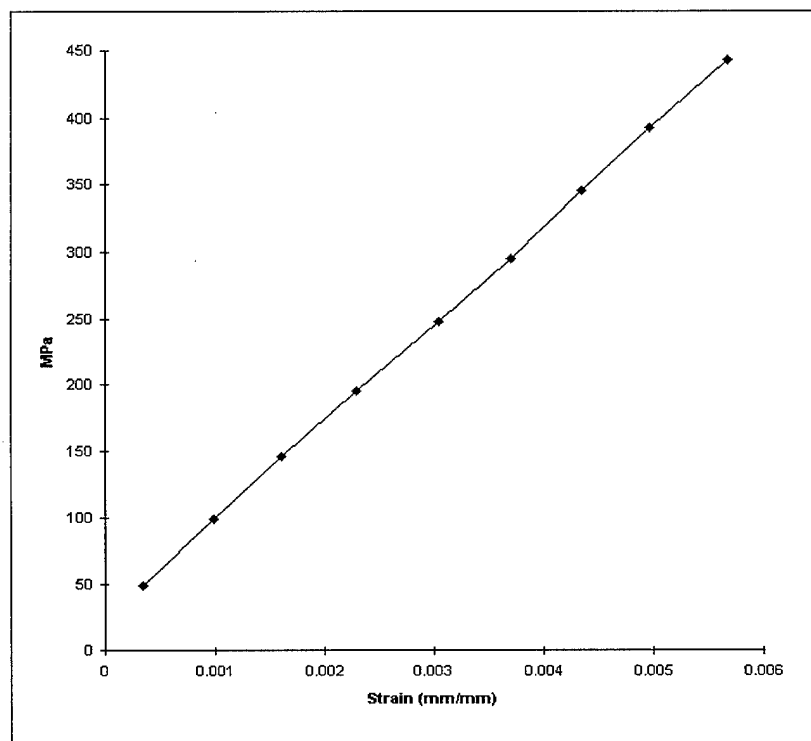


Figure 61. Stress-Strain Curve for AAT2

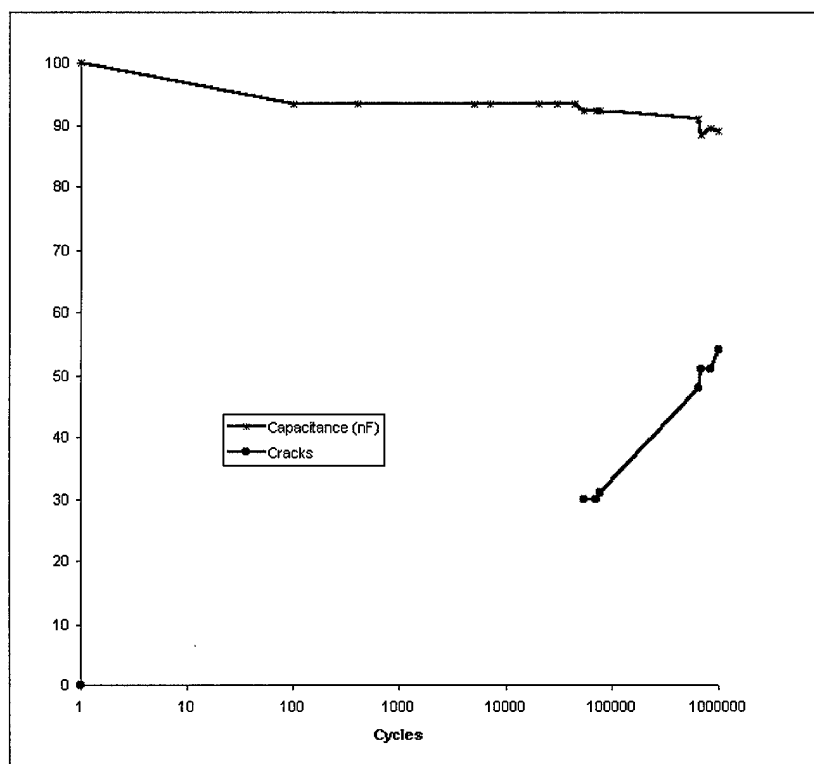


Figure 62. Specimen AAT2 Capacitance & Cracks vs Cycles

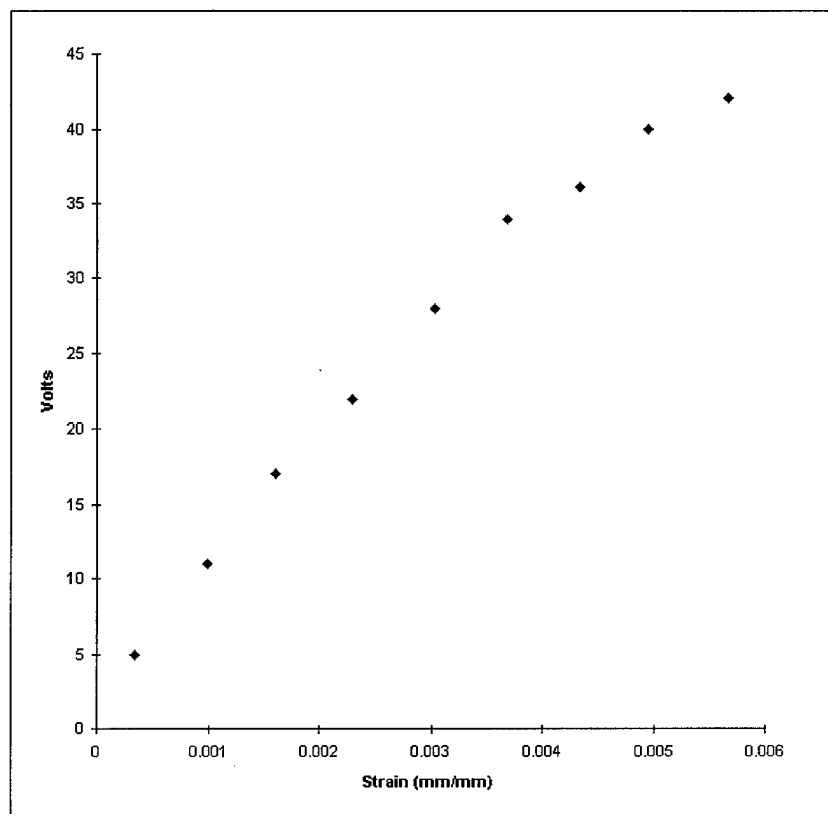


Figure 63. Specimen AAT2 Voltage Output vs Strain

As specimen AAT2 was fatigued, the stress level was intermittently lowered to 100 and 200 *MPa* to measure the voltage output at these levels as well. The object of this test was to find any load rate effects to the PZT output. Figure 64 shows how the voltage output remained constant at 100 *MPa*, while the output degraded significantly at the higher stresses after 10,000 cycles. This would seem to indicate the higher load rates caused the PZT to give a degraded output. The lower load rate enabled the PZT to have a constant output, even though transverse cracking had occurred. The reasons behind these results are unclear.

The third concern of evaluating embedded PZTs were any potential frequency effects, which could also be thought of as load rate again. After specimen AAT2's voltage output degraded, the effects of changing the frequency from 3 *Hz* to 10 *Hz* were briefly investigated. The results of these test are found in Figures 65, 66, and 67. In general, the load rate does effect the voltage output to some degree, but this aspect was not studied further. An electro-mechanical study should verify that the PZT performs best near it's natural frequency, therefore frequency effects should be dramatic.

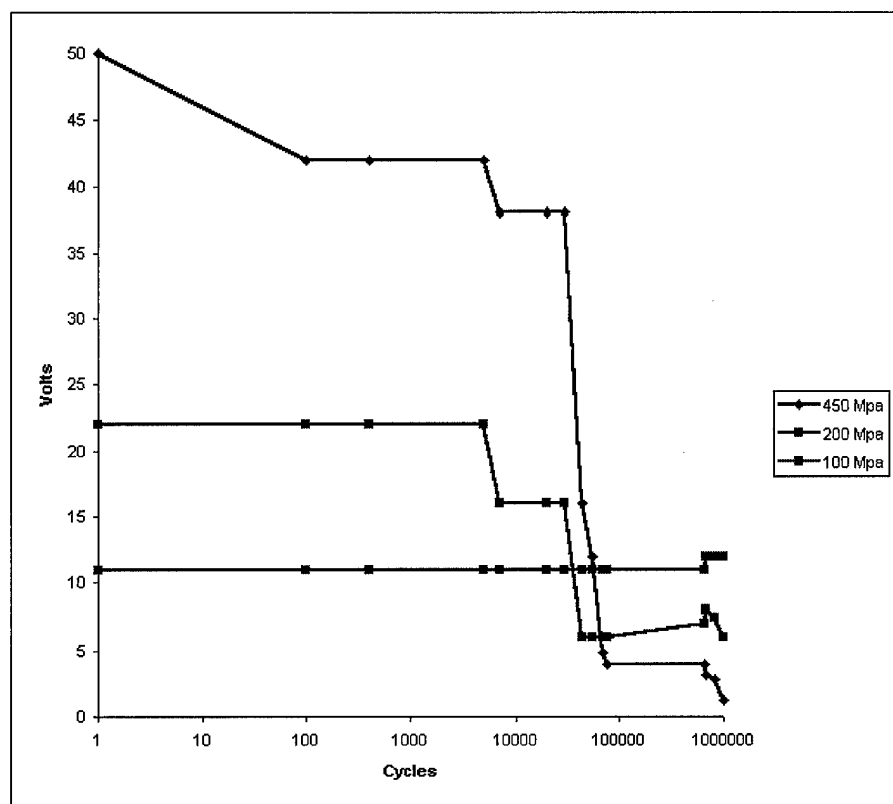


Figure 64. Specimen AAT2 Degradation of Voltage Output at Various Applied Stress Levels



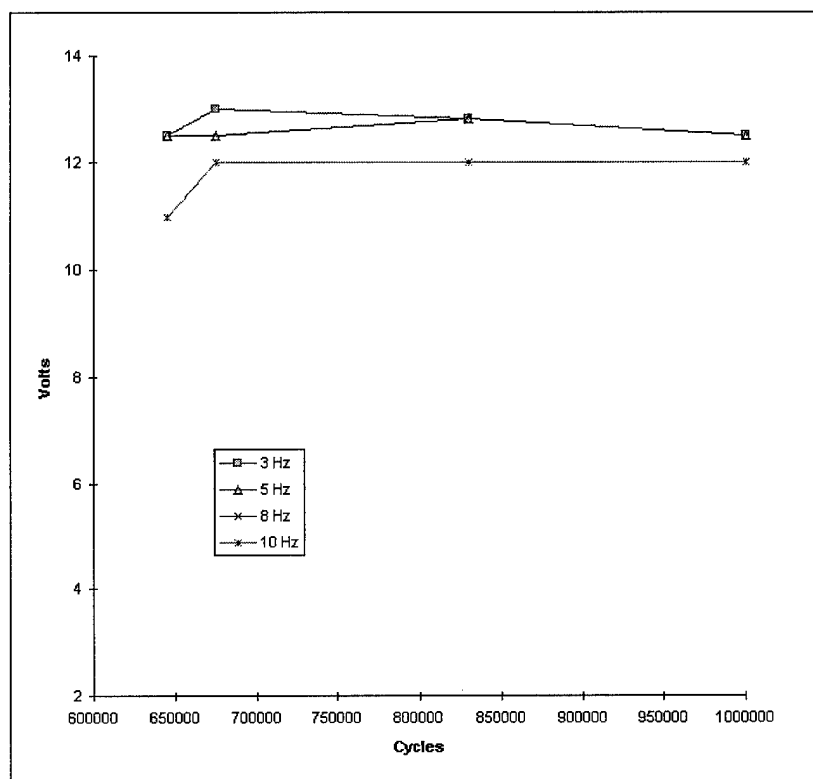


Figure 65. Frequency Effects on Voltage Output at 100 MPa

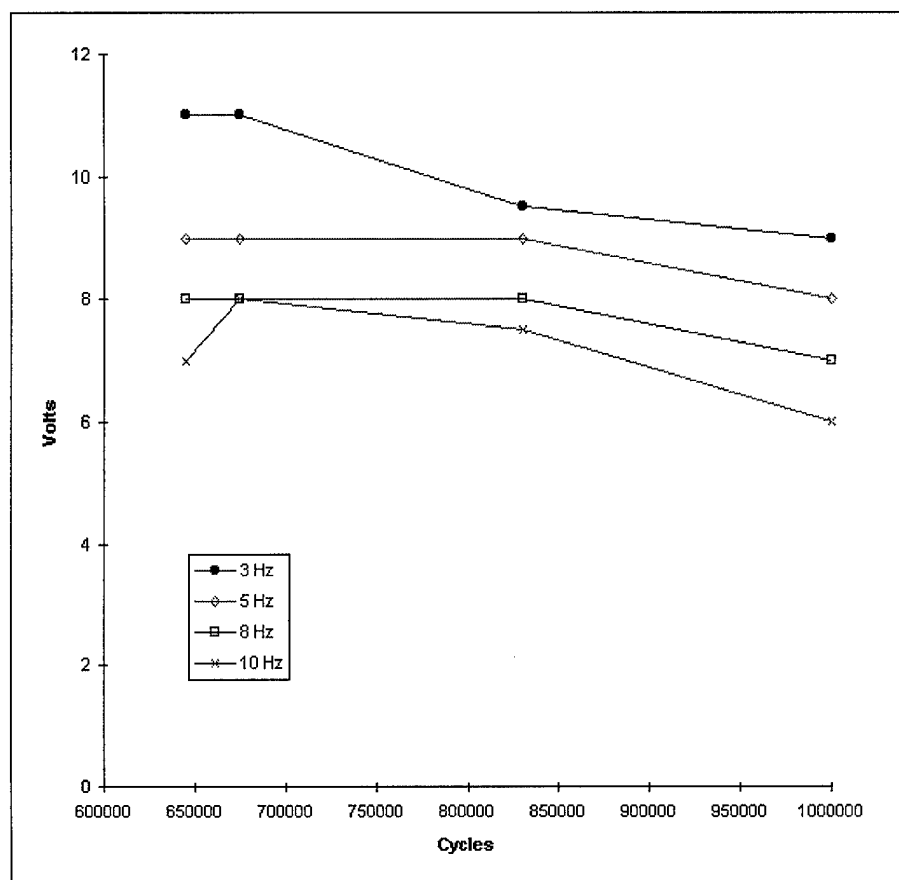


Figure 66. Frequency Effects on Voltage Output at 200 MPa

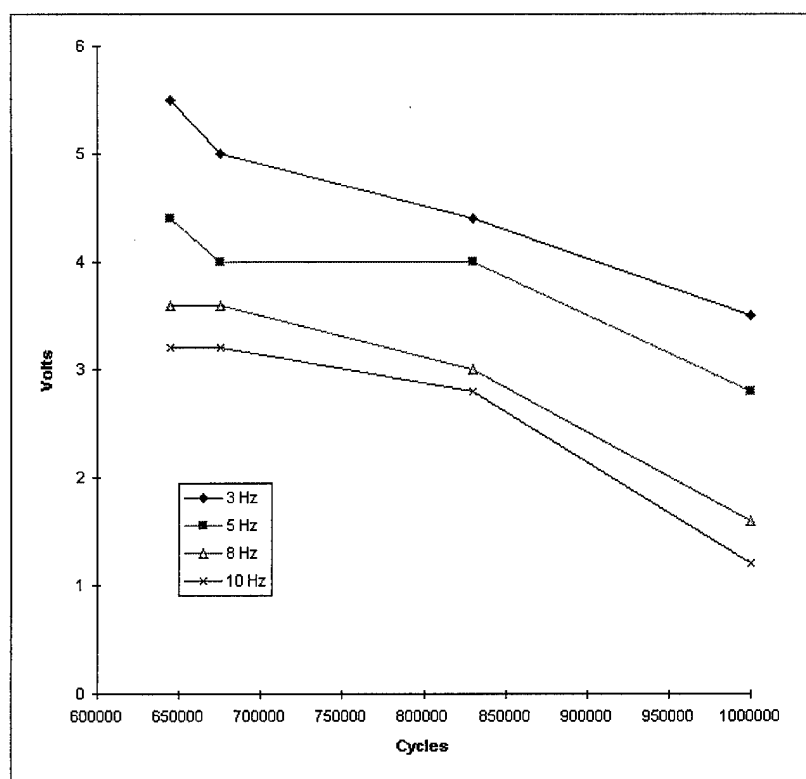


Figure 67. Frequency Effects on Voltage Output at 450 MPa

## *Bibliography*

- [1] A. J. Bronowicki, L. J. McIntyre, R. S. Betros and G. R. Dvorsky. "Mechanical Validation of Smart Structures." *Smart Material and Structures*. 129–139. IOP Publishing Ltd, 1996.
- [2] ACX. *General Specifications: Model QP15N*. Active Control eXperts, Inc., 1995.
- [3] Brei, D., "Piezoelectrics I and II, ME 599," 1996. Smart Materials and Structures.
- [4] Brei, D. *Smart Structures*. Technical Report F33615-94-C-5804, University of Michigan, 1996.
- [5] Culshaw, B. *Smart Structures and Materials*. 685 Canton Street, Norwood, MA 02062: Artech House, Inc., 1996.
- [6] Daniel, I. M. and O. Ishai. *Engineering Mechanics of Composite Materials*. 200 Madison Avenue, New York, New York 10016: Oxford University Press, 1994.
- [7] Doran, C. J. and R. J. Butler. "Characteristic of Static Actuation Behavior of Encapsulated PZT." *Smart Structures and Materials*. Crown/DRA: Defense Research Agency, 1994.
- [8] Dosedel, S. B. *Influence of Embedded Optical Fibers on Compressive Strength of Advanced Composites*. MS thesis, AFIT, 1993.
- [9] Hansen, J.P. and A.J. Vizzini. "Fatigue Response of a Host Structure with Interlaced Embedded Devices." *38th AIAA/ASME/ASCE/AHS/ASC Structures, Structural Dynamics and Materials Conference*. AIAA-97-1346. 1801 Alexander Bell Drive, Suite 500, Reston, VA, 20191: AIAA, 1997.
- [10] Jacobs, J. H. *Synthesis and Processing of Intelligent Cost Effective Structures (SPICES)*. Technical Report MDA972-93-2-0010, McDonnell Douglas Aerospace, 1996.
- [11] K. L. Reifsnider, K. Schulte and J. C. Duke. "Long-Term Fatigue Behavior of Composite Materials." *Long-Term Behavior of Composites*, edited by T.K. O'Brien. 136–159. 1916 Race Street, Philadelphia, Pa. 19103: American Society for Testing and Materials, 1983.
- [12] Kim, R. Y., "Fatigue Strength of Composite Structures," 1986. University of Dayton Research Institute.
- [13] Lynch, C. S., "The Effect of Uniaxial Stress on the Electro-Mechanical Response of 8/65/35 PLZT," 1995. Department of Mechanical Engineering, University of California, Santa Barbara, CA, 93106. Submitted to the Acta Metallurgica et Materialia.
- [14] Lynch, C. S., "Electro-Mechanical Constitutive Behavior of Various Compositions of PZT and PLZT," 1995. Department of Mechanical Engineering, University of California, Santa Barbara, CA, 93106. Submitted to the 1995 North American Conference on Smart Structures and Materials.
- [15] Mall, S. *Composites Engineering Handbook*, chapter 16, 811–889. Marcel Dekker, Inc, 1997.
- [16] Masters, J.E. and K.L. Reifsnider. "An Investigation of Cumulative Damage Development in Quasi-Isotropic Graphite/Epoxy Laminates." *Damage in Composite Materials*, edited by K.L. Reifsnider. 40–61. 1916 Race Street, Philadelphia, Pa, 19103:

American Society for Testing and Materials, 1982.

- [17] Shukla, D. R. and A. J. Vizzini. "Interlacing for Improved Performance of Laminates with Embedded Devices." *Smart Materials and Structures* 5 . 225–229. Printed in the UK: AIAA, 1996.
- [18] Singh, D. A. and A. J. Vizzini. "Structural Integrity of Composite Laminates with Interlaced Actuators." *Smart Materials and Structures*, 3 . 71–79. AIAA: Printed in the UK, 1994.
- [19] Stinchcomb, W. W. *Nondestructive Evaluation and Flaw Criticality for Composite Materials*, ASTM STP 696 . American Society for Testing and Materials, 1978.
- [20] Stinchcomb, W. W. and C. E. Bakis. "Fatigue Behavior of Composite Laminates." *Fatigue of Composite Materials*, edited by Ken L. Reifsnider. 105–119. 655 Avenue of the Americas, New York, N.Y. 10010, U.S.A.: Elsevier Science Publishers B.V, 1991.
- [21] Stinchcomb, W. W. and C. E. Bakis. *Fatigue of Composite Materials* . Elsevier Science Publishers B.V, 1991.
- [22] Warkentin, D. J. and E. F. Crawley. "Embedded Electronics for Intelligent Structures." *AIAA/AHS/ASME/ASC/ASC 32nd Structures, Structural Dynamics and Materials Conference AIAA-91-1084-CP* . 1322–1331. AIAA, 1991.
- [23] Warkentin, D. J. and J de Luis. "Use of Piezoelectric Actuators as Elements of Intelligent Structures," *AIAA Journal* , 25 1373–1385 1987.

## *Vita*

Captain Jon Mark Coleman was born on 3 March 1965 in Fort Monmouth, New Jersey, United States of America. He graduated from Greenon High School, Springfield, Ohio in June 1983. He was awarded an Air Force ROTC Scholarship and attended the Georgia Institute of Technology from 1983 to 1987 and graduated with a Bachelor Degree of Mechanical Engineering. After completing his degree, he was commissioned into the United States Air Force.

Captain Coleman was first assigned to the Eastern Space and Missile Center at Cape Canaveral AFS, Florida. His initial duties included being the 6555 ASTG environmental & propellants manager, railroad manager, and launch facilities engineer. During this time, he obtained his Masters Degree in Business Administration at the Florida Institute of Technology. After the facilities manager position, Captain Coleman became a Field Program Manager for the Global Positioning System (GPS) branch, 45 SPOS. His duties in this position included satellite count-down controller, lead engineer of anomaly resolutions, PAM-D engineer, facilities manager, and trainer. After two years in GPS, he was selected to become a Field Program Manager for Titan Payloads. Overall, his work resulted in the successful launch of over 10 systems at CCAFS.

Captain Coleman was then assigned to the National Air Intelligence Center at Wright-Patterson AFB, Ohio. His initial duties included foreign manufacturing technologies analyst and branch Attache briefer. Following this position, Captain Coleman was selected to become a Foreign Reconnaissance Satellite System Manager. Among his duties was to lead a team of eleven engineers in developing foreign satellite vulnerability and operational capability assessments.

Captain Coleman entered the School of Engineering, Air Force Institute of Technology, in May 1996.

REPORT DOCUMENTATION PAGE			Form Approved OMB No. 0704-0188	
Public reporting burden for this collection of information is estimated to average 1 hour per response, including the time for reviewing instructions, searching existing data sources, gathering and maintaining the data needed, and completing and reviewing the collection of information. Send comments regarding this burden estimate or any other aspect of this collection of information, including suggestions for reducing this burden, to Washington Headquarters Services, Directorate for Information Operations and Reports, 1215 Jefferson Davis Highway, Suite 1204, Arlington, VA 22202-4302, and to the Office of Management and Budget, Paperwork Reduction Project (0704-0188), Washington, DC 20503.				
1. AGENCY USE ONLY (Leave blank)		2. REPORT DATE December 1997		3. REPORT TYPE AND DATES COVERED Master's Thesis
4. TITLE AND SUBTITLE FATIGUE BEHAVIOR OF A QUASI-ISOTROPIC GRAPHITE/EPOXY LAMINATE EMBEDDED WITH A PIEZOELECTRIC SENSOR			5. FUNDING NUMBERS	
6. AUTHOR(S) Jon M. Coleman, Captain, USAF				
7. PERFORMING ORGANIZATION NAME(S) AND ADDRESS(ES) Air Force Institute of Technology 2750 P Street WPAFB OH 45433-7765			8. PERFORMING ORGANIZATION REPORT NUMBER AFIT/GAE/ENY/97D-02	
9. SPONSORING / MONITORING AGENCY NAME(S) AND ADDRESS(ES) Dr. Steve Donaldson WL/ML Bldg 654, Area B WPAFB OH 45433			10. SPONSORING / MONITORING AGENCY REPORT NUMBER Capt Brian Sanders AFOSR 110 Duncan Avenue, Suite B Bolling AFB, DC 20332-001	
11. SUPPLEMENTARY NOTES				
12a. DISTRIBUTION / AVAILABILITY STATEMENT  Approved for public release; distribution unlimited			12b. DISTRIBUTION CODE	
13. ABSTRACT (Maximum 200 words)  This study primarily investigated the mechanical effects of embedding piezoelectric sensors on the tensile and fatigue strength of a quasi-isotropic, carbon-epoxy laminate. A secondary focus was the investigation of the sensor degradation under tensile loading. A $[0 \pm 45 90]_s$ laminate was fabricated from Hercules AS4/3501-6 pre-preg tape. Specimens were first tested monotonically to obtain an average ultimate tensile strength and to detail the progression of damage. The fatigue tests were tension-tension, $R=0.1$ , 10 Hz, constant amplitude. Results indicated that the embedded piezoelectric sensors did not have a significant effect on the tensile strength of the laminate. Specimens with embedded sensors showed a more extensive decrease in stiffness, but a lesser degree of overall delamination due to edge effects. The embedded sensors functioned consistently at the manufacturer suggested operational range, but degraded rapidly thereafter.				
14. SUBJECT TERMS  Carbon-Epoxy Composites, Load Control, Fatigue, Quasi-isotropic, Tension-Tension, Smart Materials, Piezoelectric, Embedded Sensors			15. NUMBER OF PAGES 151	
			16. PRICE CODE	
17. SECURITY CLASSIFICATION OF REPORT Unclassified	18. SECURITY CLASSIFICATION OF THIS PAGE Unclassified	19. SECURITY CLASSIFICATION OF ABSTRACT Unclassified	20. LIMITATION OF ABSTRACT U1	